

ARGUS: A 16-PIXEL MILLIMETER-WAVE SPECTROMETER

A DISSERTATION
SUBMITTED TO THE DEPARTMENT OF PHYSICS
AND THE COMMITTEE ON GRADUATE STUDIES
OF STANFORD UNIVERSITY
IN PARTIAL FULFILLMENT OF THE REQUIREMENTS
FOR THE DEGREE OF
DOCTOR OF PHILOSOPHY

Matthew Michael Sieth

September 2016

© 2016 by Matthew Michael Sieth. All Rights Reserved.

Re-distributed by Stanford University under license with the author.



This work is licensed under a Creative Commons Attribution-Noncommercial 3.0 United States License.

<http://creativecommons.org/licenses/by-nc/3.0/us/>

This dissertation is online at: <http://purl.stanford.edu/bz783pt1914>

I certify that I have read this dissertation and that, in my opinion, it is fully adequate in scope and quality as a dissertation for the degree of Doctor of Philosophy.

Sarah Church, Primary Adviser

I certify that I have read this dissertation and that, in my opinion, it is fully adequate in scope and quality as a dissertation for the degree of Doctor of Philosophy.

Patricia Burchat

I certify that I have read this dissertation and that, in my opinion, it is fully adequate in scope and quality as a dissertation for the degree of Doctor of Philosophy.

Chao-Lin Kuo

Approved for the Stanford University Committee on Graduate Studies.

Patricia J. Gumport, Vice Provost for Graduate Education

This signature page was generated electronically upon submission of this dissertation in electronic format. An original signed hard copy of the signature page is on file in University Archives.

Abstract

This thesis presents the development and deployment of *Argus*, a 16-pixel millimeter-wave spectrometer for the 100 m Robert C. Byrd Green Bank Telescope (GBT). *Argus* enables astronomical imaging at state-of-the-art mapping speeds and high angular resolution over the 76–116 GHz band. Its applications include studies of star formation, comets, astrobiology, and astrochemistry. *Argus* was installed on the GBT and measured first light in March 2016. It will be available to the general radio astronomy community beginning in the winter 2016 observing semester.

This work has demonstrated a novel scalable approach to building a focal plane array. The *Argus* array is built in 4-pixel subunits, which are tiled together to form the 16-pixel array. In principle, these subunits could be used as the building blocks of an even larger array. Every part is designed to be compact, mass-producible, and as economical as possible. The core technology is based on miniaturized receiver modules, which integrate low-noise amplifiers, a bandpass filter, and a mixer into a single compact unit that would be amenable to automated assembly. The *Argus* receiver array achieved low noise performance over a very wide bandwidth, which both enables a number of new scientific opportunities in the near term while demonstrating the viability of the design concept for future receiver designs.

Acknowledgements

Firstly, I thank my advisor Sarah Church. She directed me towards an interesting project in *Argus*, which was only just beginning when I joined the group. Sarah ultimately gave me the opportunity to play a leading role in the design, development, deployment, and commissioning of the instrument. I am indebted to Sarah not only for the plethora of technical skills that I took away from this project, but for her lessons in project management. I also thank the rest of my thesis committee including Chao-Lin Kuo, Patricia Burchat, Kent Irwin, and Gregory Valiant for their useful feedback on my thesis work.

I've been privileged to work with a lot of talented people over the course of my graduate career. The *Argus* instrument was built in collaboration with a number of colleagues from whom I have learned a great deal: Dongwoo Chung, Kiruthika Devaraj, Patricia Voll, Kieran Cleary, Rohit Gawande, Tony Readhead, Rodrigo Reeves, Andrew Harris, Joshua Gunderson, Todd Gaier, Paul Goldsmith, Pekka Kangaslahti, Lorene Samoska, Nichol Cunningham, Dennis Egan, David Frayer, Michael Stennes, and Steve White. In the Stanford lab I've been fortunate to work with two good postdocs in Kiruthika and Judy. I've enjoyed my time both working and socializing with the other Church Group members including Patricia, Stephen, Keith, and Ed. I am thankful to Dan for teaching me some of the finer points of microwave engineering in my early years of graduate school. It's been a privilege to mentor a number of undergraduate students in the lab including Niloofer, Anthony, and Javier, who all made significant contributions to the group.

I owe a great deal of thanks to my friends who have made my time in graduate school a really fun experience. I've had a number of housemates who doubled as

great friends including Alex, Jamie, Tomas, Karl, Jared, Cat, David, Nils, Deborah, Julia, Fernando, Carly, Tom, Lucas, Becky, Reed, and Anya. I thank my best friend Rose for the fun adventures that were necessary breaks from work and for helping me push through the more stressful stretches of graduate school. Thanks to my other California friends who include Ace, Andreas, Andrew, Camille, Ellen, Hayden, Jeff, Jim, Kassa, Keith, Luca, Micheal, Paul, Richard, Tyler, and Varun. I'm also indebted to my West Virginia crew who have made my time at the Green Bank Telescope an awesome experience: Amber, Anna, Clarissa, Evan, Jennifer, Justin, Kelly, Nichol, Ryan, Tomas, and Vereese. Finally, thanks to all of my other friends from Wisconsin and elsewhere for their support.

There are a number of support staff at Stanford who have helped me throughout graduate school. The machine shop staff not only machined crucial *Argus* parts, but patiently taught me how to make better technical drawings and how to operate the equipment. Dana, the administrative assistant in our group, processed countless purchase orders for *Argus* parts and lab equipment. The Physics staff – including Maria, Violet, and Rosenna – helped me to navigate the administrative hurdles of my graduate career.

Finally, I thank my family who have always supported me in all of my endeavors.

Contents

Abstract	iv
Acknowledgements	v
1 Introduction	1
1.1 Radio and Microwave Astronomy	1
1.2 Spectroscopic Science with <i>Argus</i>	2
1.2.1 Molecular Spectral Lines	3
1.2.2 Gas Tracers	7
1.2.3 Star Formation Relations	8
1.2.4 Filaments	11
1.2.5 Other Science	12
2 The <i>Argus</i> Instrument	14
2.1 The <i>Argus</i> Collaboration	14
2.2 Receiver Architecture	15
2.2.1 Heterodyne Receivers	15
2.2.2 Mixers	15
2.3 Sensitivity	19
2.3.1 Noise Temperature	20
2.3.2 The Radiometer Equation	20
2.3.3 Friis Equation	21
2.4 Specifications	22
2.4.1 Number of Pixels	23

2.4.2	RF and LO Input	23
2.4.3	IF Output	23
2.4.4	Receiver Temperature	24
2.4.5	Angular Resolution	24
2.4.6	Polarizations	25
2.4.7	Image Rejection Ratio	25
2.4.8	Dynamic Range	25
2.4.9	Passband Slope	26
2.4.10	Gain Stability	26
2.4.11	Scalability	27
2.5	The Radiometer	28
2.5.1	Design Concept	28
2.5.2	RF System	32
2.5.3	LO System	33
2.5.4	IF System	34
2.5.5	Cryogenics	37
2.5.6	Comparison with Similar Instruments	41
2.6	<i>Argus</i> Prototypes	41
3	Miniaturized Receiver Modules	46
3.1	Technology	52
3.1.1	Monolithic Microwave Integrated Circuits (MMICs)	52
3.1.2	High-electron-mobility transistors (HEMTs)	53
3.2	Chip Set	57
3.2.1	Low-Noise Amplifiers	57
3.2.2	Mixers	58
3.3	Packaging	60
3.4	Performance	64
4	Cryogenic Signal Distribution	68
4.1	Multilayer Printed Circuit Boards	69
4.1.1	Construction	69

4.1.2	IF Design	73
4.1.3	LO Design	80
4.2	Microstrip Flex Circuit Interconnects	88
4.2.1	Wirebond Interface	89
4.3	Performance	90
4.3.1	IF System	90
4.3.2	LO System	90
5	<i>Argus</i> Commissioning	96
5.1	Receiver Characterization in Lab	97
5.1.1	Receiver Temperature	97
5.1.2	Expected System Temperature	99
5.1.3	Dynamic Range	100
5.1.4	IF Power	103
5.1.5	Passband Slope	104
5.1.6	Stability	108
5.1.7	Image Rejection	116
5.2	On-The-Fly Mapping	119
5.3	Calibration	125
5.3.1	Chopper Vane	127
5.3.2	Flux Calibration	129
5.3.3	Position Switching	130
5.3.4	Frequency Switching	131
5.3.5	Pointing and Focus	132
5.3.6	Active Surface Corrections	132
5.4	LO Troubleshooting	132
5.4.1	Insufficient LO Power	133
5.4.2	LO-to-RF Leakage	134
5.4.3	Broadband LO Noise	138
5.5	<i>Argus</i> Installation and First Light	141
A	Y-Factor Method	145

B	<i>Argus</i> Optics	146
B.1	The Robert C. Byrd Green Bank Telescope	146
B.2	Antenna Efficiency	147
B.3	Simulated <i>Argus</i> Performance	151
B.3.1	Mode Decomposition	151
B.3.2	Simulated Efficiencies	151
B.3.3	Figures of Merit	153
C	Measurement Setups	158
D	Frequency Tripler	162

List of Tables

1.1	List of some key transitions from 76–116 GHz. The names of the principal isotopic species are in bold. The <i>Argus</i> receiver covers the entire 76–116 GHz range with state-of-the-art sensitivity; however the instrument performance has been fine-tuned for two pairs of lines that are indicated in blue: HCN & HCO ⁺ and C ¹⁸ O & ¹³ CO.	4
1.2	Table of the Einstein A coefficients for spontaneous emission, the collision rates (γ), and the critical densities (n_{crit}) for some of the key molecular spectral lines for <i>Argus</i> science. The data were retrieved from the Leiden Atomic and Molecular Database [1] for a gas temperature of 100 K. The frequency for these transitions are given in Table 1.1. The critical density (<i>i.e.</i> the density at which the spectral line is thermalized and therefore emits significantly) is calculated from Equation 1.10, which assumes that the gas is optically thin. The table is ordered by increasing critical densities. In practice, many <i>Argus</i> observations will target multiple lines in order to explore different density regimes. . .	8
2.1	The distribution of work for the <i>Argus</i> collaboration.	16
2.2	Specifications for the <i>Argus</i> array.	22
2.3	Key differences between the first prototype, second prototype, and production version of <i>Argus</i> . There were significant changes in the frequency ranges, the downconversion scheme (§2.2.2, §3.2.2), and the cryogenic routing components (§4).	42

3.1	A summary of the low-noise amplifiers used in the <i>Argus</i> prototype and production designs and their performance over the 75–115 GHz frequency range.	59
4.1	A summary of the multilayer routing board properties for the prototype and production receivers.	71
4.2	Technical specifications for the core materials used for constructing the multilayer printed circuit boards. The coefficients of thermal expansion (CTE) are well matched to copper in the transverse directions (<i>i.e.</i> x and y). The copper surface roughness is quoted for 0.5 oz/ft ² electrodeposited copper. The PFTE-based cores are capable of supporting lower loss transmission lines than the hydrocarbon/ceramic cores because of their superior loss tangent and copper surface roughness.	71
4.3	Technical specifications for the prepreg materials used for constructing the multilayer printed circuit boards. The low loss tangent of the prepreg for PFTE-based cores allow for transmission lines with very low insertion losses.	72
4.4	Details of the multilayer routing board stack-ups. The metal layers are all 0.5 oz/ft ² electrodeposited copper, which has a thickness of 0.0007".	73
4.5	Specifications for the <i>Argus</i> IF amplifier candidates for the production design. All of the amplifiers cover the 0.90–2.15 GHz <i>Argus</i> IF bandwidth.	75
5.1	A table of the specifications for the <i>Argus</i> receiver that were measured in the lab along with the relevant section. These specifications are a subset of the design specifications presented in §2.4.	97
5.2	The noise parameters extracted from the spectroscopic Allan variance data depicted in Figure 5.10. The 1/ <i>f</i> contribution to the Allan variance and the drift power law index α are expected to be the same on the sky as in the laboratory. The Allan time, on the other hand, depends on the white noise level, which depends on the measurement configuration.	112

5.3 The expected Allan times for observations on the sky. These are simply the minima of the spectroscopic Allan variance models that are plotted in Figure 5.11. Alternatively, Equation 5.10 can be used to predict the Allan time of an arbitrary observational configuration. 114

5.4 Specifications for the amplitude and phase imbalances that would be required to achieve a particular *IRR* target. The first number given assumes that the amplitude and phase imbalances contribute equally to the *IRR*, while the value in parentheses assumes that just one of these factors is contributing to the *IRR* and the other one is negligibly small. 118

List of Figures

1.1	The opacity of the Earth’s atmosphere as a function of wavelength. There are “atmospheric windows” at radio and microwave frequencies that allows observations to be made terrestrially. <i>Argus</i> utilizes the atmospheric window at around 3 mm. Credit: NASA.	2
2.1	A schematic for a simple heterodyne receiver. Impinging radiation is collected with an antenna. The signal is then amplified, filtered, and downconverted by mixing the input RF signal with a reference LO signal (§2.2.2).	15
2.2	A mixer downconverts the input radio frequency (RF) signal, which is shown in red, by multiplying the input signal with a reference tone, known as the local oscillator (LO). The output signal, or intermediate frequency (IF), is shown in blue and has a frequency that is the difference of the LO and RF frequencies. The IF also a high frequency component from the sum of the LO and RF frequencies, which is typically rejected through filtering. The frequency of the RF signal can be either above or below the LO frequency, which are known as the upper sideband (USB) and lower sideband (LSB). The upper and lower sidebands get converted into the same IF frequency range, which means that at a given IF frequency it is impossible to determine which sideband the signal is from unless the sidebands are separated using one of the techniques discussed in §2.2.2.	18

2.4	The footprint of the <i>Argus</i> array relative to the 24" turret hole through which the receiver is mounted. The black circle represents the turret hole. The red circles represent the physical size of the <i>Argus</i> feedhorn antennas, which are packed in a 4x4 square array. The <i>Argus</i> receiver occupies a small fraction of the available space in the turret hole. In principle a 144-pixel <i>Argus</i> -like array (<i>i.e.</i> 9 copies of <i>Argus</i> tiled together) would fit easily into this space, which is indicated by the blue circles.	27
2.5	A schematic of the cryogenic front-end of the <i>Argus</i> receiver. The miniaturized receiver modules take millimeter-wave signals (76–116 GHz) at the RF port and amplify, filter, and down convert them to double-sideband IF outputs (0.90-2.15 GHz). The bandpass of the receiver modules is provided by the input waveguide, which has a sharp low frequency cut-off, and a high-pass filter (HPF). Further cryogenic amplification and band definition via a low-pass filter (LPF) is provided on the multilayer routing board. Each 4-pixel card receives a local oscillator signal, which is split four ways on the routing board. Detailed schematics for the warm IF and the LO systems are given in Figures 2.11 and 2.9, respectively.	29
2.6	(a) An annotated CAD drawing of the production 4-pixel card. The production card has a 1.5 GHz instantaneous bandwidth to match the GBT backend. (b) A CAD drawing of the 4x4 <i>Argus</i> focal plane array. The array is built from 4-pixel subunits, or cards, which form the rows of the array. A card comprises the feedhorns, MMIC receiver modules, routing boards, flexible circuitry and cables.	30
2.7	A photograph of the <i>Argus</i> focal plane.	31
2.8	The <i>Argus</i> window, which is made from 0.5" thick ultra-high-molecular-weight polyethylene.	32

2.9	A schematic of the LO system. The LO system multiplies, amplifies, filters and splits the LO. The waveguide acts as a high pass filter to reject the fundamental tone from passing. The power values in red are the expected power levels at various points in the LO chain at a synthesizer frequency of 13.875 GHz (<i>i.e.</i> an effective LO of 111.0 GHz).	35
2.10	A plot of the output LO power from one of the 4-pixel cards as a function of LO frequency. The LO power decreases with LO power level because of ohmic losses in the system; however, the LO power is above the specification of -5 dBm across the entire LO frequency range for <i>Argus</i> .	36
2.11	A schematic of the room temperature IF board. A quadrature hybrid separates the IF into its upper and lower sideband components. A switch allows the user to choose which sideband to observe. The following amplifiers, attenuators, and equalizers ensure compliance with the power and slope specifications for the VEGAS spectrometer. For pixels 1–8, a is 6 or 10 and b is 1–3. For pixels 9–16, a is 5 and b is 10.	38
2.12	A table of the heat loads on the <i>Argus</i> CTI 1020 cryostat for (a) the second stage at ~ 25 K and (b) the first stage at ~ 70 K.	39
3.1	The <i>Argus</i> Prototype 1 miniaturized receiver module. (a) A schematic of the receiver module showing the gains and bandwidths of some of the key components. (b) A CAD drawing of the split-block receiver design. The components are mounted in cavities in the base block, while the RF lid provides a hermetic seal. (c) A photograph of the assembled receiver module before the lid was closed.	48
3.2	The <i>Argus</i> Prototype 2 miniaturized receiver module RF design. (a) A schematic of the receiver module showing the gains and bandwidths of some of the key components. The total receiver gain is approximately 15–27 dB. (b) A photograph of the assembled receiver module before the RF lid was closed.	49

3.3	The <i>Argus</i> Prototype 2 miniaturized receiver module packaging. (a) A CAD drawing of the split-block receiver design. The components are mounted in cavities in the base block, while the RF lid provides a hermetic seal. The IF and LO connectors are miniaturized push-on connectors that launch from the side of the receiver module. (b) A photograph of the outside of the miniaturized receiver module after assembly.	50
3.4	Photographs of the Pre-production and Production <i>Argus</i> miniaturized receiver modules. Both of these designs have a keying mechanism along the length of the receiver module that facilitates blind mating into the focal plane array.	51
3.5	The band diagram for the heterojunction between an n-type InAlAs layer and an undoped InGaAs layer. The image is adapted from https://en.wikipedia.org/wiki/High-electron-mobility_transistor#/media/File:HEMT-band_structure_scheme-en.svg	54
3.6	The equivalent circuits of a field-effect transistor that are used in the Pospieszalski noise model [2].	56
3.7	The conversion loss for the mixer used in Prototypes 1 and 2. A range of LO frequencies from 40–50 GHz was used. (a) The performance as a function of the RF frequency. The IF frequency ranges from 1–25 GHz. Lower IF frequencies were measured, but a DC block capacitor causes the response to roll off significantly below 1 GHz. The conversion loss varies from 11–25 dB amongst the different LO configurations. A fixed 50 GHz LO frequency can be used to cover the entire 75–115 GHz frequency range with a conversion loss of 12–23 dB. (b) The conversion loss is plotted for only IF frequencies below 2 GHz in order to illustrate the degradation in performance due to the DC block capacitor on the mixer chip.	61

3.8	A plot of the conversion loss versus RF frequency for the mixer used in the Pre-production and Production receiver modules as reproduced from [3]. The IF frequency is fixed at 1 GHz. The conversion loss ranges from 10–18 GHz over the 80–120 GHz band.	62
3.9	(a) The performance of the <i>Argus</i> Prototype 1 receiver module. This receiver has good performance from 81–102 GHz, which covers the astronomically important HCN (88.632 GHz) and HCO+ (89.189 GHz) high density gas tracers, but it does not cover any lines for CO or its isotopomers. (b) The performance of the <i>Argus</i> Prototype 2 receiver module, which is reproduced from [4]. The performance is good from 75–111 GHz, which is an improvement upon the Prototype 1 receiver. The Prototype 2 receiver can therefore measure the C ¹⁸ O (109.782 GHz) and ¹³ CO (110.201 GHz) lines, which are important for tracing the total molecular gas mass and measuring the column density of the gas; however, like the Prototype 1 receiver, it is unable to measure the CO (115.271 GHz) line.	65
3.10	(a) The measurement setup for characterizing the noise temperature of the Pre-production receiver module. The I channel included an NXP BGU7003W amplifier, which was one of the <i>Argus</i> amplifier candidates (§4.1.2). The amplifier was added as a check that the gain of the receiver module was sufficiently high to overcome the noise from the amplifier and that the reflection between the two components was not prohibitively high. (b) The measured performance of the Pre-production Receiver in this measurement setup. The channel with the cryogenic IF amplifier had similar performance to the channel without the amplifier.	66

3.11	The measured performance for the Production <i>Argus</i> receiver modules as measured by Rohit Gawande at Caltech. The noise performance is good over the entire <i>Argus</i> bandwidth of 76–116 GHz, although the performance degrades below 85 GHz. The average receiver has 27–52 K noise temperature across the 76–116 GHz <i>Argus</i> bandwidth. There is a sweet spot at 108 GHz where it achieves a record low spot noise temperature of 23 K.	67
4.1	(a) A photograph of the production multilayer routing board. (b) A CAD drawing of the production signal routing board. The board has six layers: a top layer with microstrip and co-planar waveguide (red), an embedded stripline layer (violet), an embedded layer for DC lines (green), and three reference ground planes (not shown). The pads at the top are for custom push-on connectors for the IF and LO (§3.3). The ground pad in the lower right is for attaching the flexible microstrip lines (§4.2).	70
4.2	The measurement setup for cryogenically characterizing the IF amplifier candidates. Semirigid coaxial cables with stainless steel outer conductors were used as the thermal break between the cooled amplifier and the room temperature test components.	75
4.3	The performance of the four cryogenic IF amplifier candidates for <i>Argus</i> . Shown here are (a) the gain and (b) the noise temperature over the 0.90–2.15 GHz IF band. Notably the noise temperatures were <i>not</i> corrected for the effect of the coaxial cables; the noise temperatures are for the entire system shown in Figure 4.2.	76

4.4	The Avago VMMK-2303 amplifier was thermally cycled several times and the gain was checked for reproducibility. The amplifier did not fail after repeated coolings. This model was eventually selected as the cryogenic IF amplifier for <i>Argus</i> . The measurements were interspersed over the span of months which meant that the test setups were similar but not exactly the same. Differences in the amplifier temperature might account for the slight change in gain levels.	77
4.5	(a) Left: A photograph of a test board with two back-to-back stripline-to-microstrip transitions. The two signal chains are separated by 1.0". Right: A CAD model of the transition. (b) The performance of the test board. These measurements demonstrate that the microstrip-to-stripline transitions are not the dominant source of insertion loss in the IF chain. The return loss is better than 20 dB over the <i>Argus</i> band, which minimizes the level of standing waves in the system.	79
4.6	(a) The insertion loss is plotted for various levels of solder mask removal. The solder mask contributes to substrate losses. The solder mask was removed over a width of three times the microstrip trace width. Further removal does not improve the insertion loss. (b) The insertion loss is shown for three different choices of surface finish: none (<i>i.e.</i> bare copper), immersion silver (IAg), and electroless nickel immersion gold (ENIG). The production boards utilized an IAg finish, which does not degrade the insertion loss.	83
4.7	A finite element model of a prototype version of the <i>Argus</i> LO coaxial connector launches. The signal is shown radiating into the 0.001" gap between the board and the connector, which formed a resonant cavity. This effect led to poor connector performance. This effect was mitigated by decreasing the board thickness, changing from a microstrip launch to coplanar waveguide, and receding the interior layers of the multilayer routing board.	84

4.8	The simulated insertion loss for the LO coaxial connector launches. The prototype board suffered from a resonance in the gap between the multilayer printed circuit board and the connector as illustrated in Figure 4.7. The simulated insertion in this prototype design is high and has many spectral features, which can be attributed to this resonance. The resonance was detuned by decreasing the board thickness, changing from a microstrip launch to a coplanar waveguide launch, and receding the ground planes. The resulting simulated performance is adequate for providing sufficient LO power to the <i>Argus</i> receivers over the 39–59 GHz band.	85
4.9	The microstrip insertion loss per inch after the substrate losses, metal losses, and radiation losses were improved via prototyping.	86
4.10	(a) A photograph of a Wilkinson splitter test board on 0.010” PFTE-based core. (a) The measured performance of the Wilkinson splitter test board. The insertion loss of the connectors and the microstrip leads have been subtracted.	87
4.11	(a) A photograph of a prototype of the microstrip flexible circuitry. (a) The performance of the prototype as reproduced from [5]. The insertion loss is shown in red and the nearest neighbor cross-talk is shown in blue. The solid traces correspond to microstrip lines with a solid ground plane and the dashed traces correspond to the patterned ground plane. The patterned ground plane decreases the thermal conductivity at the expense of a small increase in insertion loss and a modest increase in cross-talk; the patterned ground plane was not implemented in the <i>Argus</i> boards because the heat loading from the flexible was already sufficiently low. The solid ground plane provides an insertion loss of 0.076 dB/GHz/in.	91

4.12	A hermetic feedthrough was designed for the IF signals. (a) On the inside of the cryostat the flexible microstrip lines are soldered to glass bead connectors. Clamps provide a ground connection and strain relief. (b) The IF interface on the outside of the cryostat is a pattern of 8 SMA connectors.	92
4.13	(a) A photograph of the wirebond interface. (b) An HFSS model of the wire bond to flexible circuit interface. The model is split in half in order to capitalize on the H-plane symmetry of the fields. (c) The insertion loss and return loss for this interface. The microstrip lines have been de-embedded from the model.	93
4.14	The cryogenic IF routing was characterized for four channels. Shown in the sub-panels are (a) the gain, (b) the noise temperature, and (c) the cross-talk between channels.	94
4.15	The insertion loss in the LO chain for a typical multilayer routing board. The 4-way split accounts for 6 dB of the insertion loss. The ripple is due to impedance mismatches at the input and output connectors. The performance is sufficient to route enough LO power to the miniaturized receiver modules (§2.5.3).	95
5.1	A photograph of the test setup for measuring the receiver noise temperature. The white styrofoam box contains an absorber that is immersed in a liquid nitrogen bath at 77 K, which together comprise the cold load. A piece of room temperature absorber is moved over the window (and below the styrofoam box) by a stepper motor to provide the hot load.	98
5.2	The receiver temperature for all 16 <i>Argus</i> pixels as measured in the lab. The noise temperature for an average receiver is 39–65 K and meets the specification of 60 K at all but the lowest frequencies in the <i>Argus</i> passband.	99

5.3 The expected system temperature versus frequency for observations at an elevation of 30° and 90°. The light traces show the system temperature for the individual pixels and the dark traces are the average system temperatures. 101

5.4 A plot of two signals with 0 dBm power: a white noise signal and a continuous-wave tone (*i.e.* a sine wave). A 50Ω impedance is assumed. Despite the fact that both traces have the same average power, the instantaneous power of the white noise trace occasionally experiences brief spikes. The warm IF electronics were originally designed using saturation specifications that were deduced using continuous-wave measurements; however, since *Argus* measures noise-like signals that occasionally have short timescale spikes in power, some of the amplifiers in the warm IF electronics system were driven into saturation. The attenuators in the system were adjusted to account for this issue as shown in §2.5.4. 102

5.5 The linearity of the warm IF system for pixel 6. A variable attenuator was inserted at the input of the warm IF electronics and varied from 1–32 dB. The IF system is linear over an 18 dB dynamic range, which meets the specification of 5 dB. At the highest attenuation levels the noise temperature of the warm IF components leads to a deviation from linearity. 103

5.6 The IF power of each of the 16 pixels while observing a room temperature load. Pixels 1–8 were adjusted so that the IF power was as high as possible without saturation in the IF chain. The specification is -5 dBm, but higher powers are desirable. Pixels 9–16 to not have a strict specification and were set to ~-25 dBm 105

5.7	A typical IF spectrum as measured with a spectrum analyzer with 5 MHz resolution bandwidth. There are two important features. The first is a sinusoidal component, which has a trough at ~ 1.2 GHz and peak at ~ 1.9 GHz. This feature is from LO-to-IF leakage; the LO noise is downconverted into the IF. The LO lines on the multilayer routing board have ~ 1.2 GHz standing waves from connector mismatch (see Figure 4.15), which is the source of the sinusoids seen in the IF spectrum. This phenomenon increased the receiver noise temperature as discussed in §5.4.3. This problem was mitigated by filtering the LO signal, but yet the effect of LO noise can still be seen in the IF spectrum. The second feature is a rising slope of ~ 2 dB across the <i>Argus</i> band of 0.90–2.15 GHz. This slope is seen in all pixels and can be attributed to the equalizer in the warm IF electronics (§2.5.4), which overcompensates for ohmic losses in the system. The slope could be flattened and the IF power levels could be increased by adjusting the equalizer.	106
5.8	The peak-to-peak power in the IF spectrum for all 16 pixels. The large peak-to-peak power for pixel 12 was observed at just one of the LO frequencies over which <i>Argus</i> was characterized. The IF spectra for this pixel were otherwise unremarkable. Despite this data point, all pixels meet the 10 dB specification for IF slope.	107
5.9	The total power Allan variance for pixel 3. The RF frequency was set to 85.5 GHz with the LO configured for a lower sideband configuration.	110
5.10	The spectroscopic Allan variance for pixel 3. The RF frequency was set to 85.5 GHz with the LO configured for a lower sideband configuration. The noise is fit to a model with three components: radiometric noise, $1/f$ noise, and drift.	111

5.11	The expected spectroscopic Allan variance for observations on the cold sky. The radiometric component of the Allan variance is dependent on the bandwidth of the observation. Considered here are channel width for two VEGAS configurations (92 kHz and 1,465 kHz) and the spectral line width of a 17 km/s HCN line (5,000 kHz), the latter of which could be binned to form an image.	113
5.12	A typical waterfall plot showing 30 IF spectra that are each integrated for 60 s and normalized to the first integration. The bottom trace is the first integration and each subsequent measurement is plotted above the previous one with an offset. The topmost trace therefore shows the stability of the passband over 30 minutes. The passband remained relatively flat over 30 minutes, which was a qualitative indication that <i>Argus</i> is stable enough to do useful science. The observed spectral features in this measurement would be straightforward to remove in an observation with baseline subtraction.	115
5.13	A photograph of the test setup for measuring the image rejection ratio. A fixed frequency signal is injected into the input of the receivers via a synthesizer, frequency multipliers, a variable attenuator, and a feedhorn antenna. The signal and image are then measured at the IF output with a spectrum analyzer.	120
5.14	The image rejection data for all 16 <i>Argus</i> pixels. The majority of pixels and frequencies meet the 10 dB specification. The handful of data points below specification could not be improved after repeated optimizations. These data were eventually deemed good enough to do useful science despite not meeting the specification in part because these LO frequencies will not be used for observing HCN & HCO ⁺ and C ¹⁸ O & ¹³ CO for which <i>Argus</i> was optimized.	121
5.15	The original LO chain for <i>Argus</i> , which was used during most of the receiver integration and testing at Stanford. Spurious signals from this LO chain led to significant artifacts in the receiver performance data. The LO chain in Figure 2.9 was implemented to solve these problems.	133

5.16	(a) A photograph of the three types of shields that were used to block LO-to-RF leakage: a metal case encloses the multilayer routing boards, a machinable piece of absorber shields the connector between the multilayer routing boards and the miniaturized receiver modules, and a metal sheet at the feedhorn antenna input plane. (b) A photograph of the connector shield before the miniaturized receiver modules were installed. Each shield is a rectangular piece of absorber with holes drilled out for the connectors to pass through.	137
5.17	The receiver temperature for all 16 <i>Argus</i> pixels as measured in the lab with the YIG filter bypassed in the LO chain. This data is to be compared with Figure 5.2, which shows the receiver temperatures with the YIG filter in place. The spikes in the noise temperature when the filter is bypassed can be attributed to LO noise power that is downconverted into the IF path.	140
5.18	Photographs from the <i>Argus</i> installation on the GBT. (a) The <i>Argus</i> cryostat being hoisted to the top level of the GBT. (b) The instrument being lowered into the receiver turret. (c) The top side of the receiver after installation. A radome protects the <i>Argus</i> window from the elements. A nozzle blows dry air across the radome to prevent condensation. (d) The bottom side of the receiver after during installation.	142
5.19	The <i>Argus</i> first and second light measurements of Orion. (a) The first light spectrum centered around 110 GHz that targeted C ¹⁸ O and ¹³ CO. (b) The second light spectrum of ¹² CO. (c) A raster map of HCN. . .	143
B.1	A photograph of the Robert C. Byrd Green Bank Telescope. Credit: NRAO.	148
B.2	A CAD model of the GBT that was used to study the observing efficiency and mapping speed of <i>Argus</i> as a function of the feedhorn beam size.	152

B.3	The higher-order modes of the <i>Argus</i> horns that were simulated in [6]. The simulated beam patterns were imported into an optical design program to study the optical interface between <i>Argus</i> and the GBT. About 93% of the power is in the fundamental Gaussian mode.	153
B.4	(a) The coupling efficiencies to the telescope versus edge taper at a frequency of 100 GHz. The optimal antenna efficiency, which is the relevant efficiency for point source detection, is at ~ 11 dB. The <i>Argus</i> edge taper at 100 GHz is ~ 15 dB. (b) The coupling efficiencies to the telescope versus frequency. The illumination efficiency and surface efficiency degrade with increasing frequency.	154
B.5	(a) The relative mapping times versus edge taper at 100 GHz. The mapping times improve with increasing edge taper. (b) The relative mapping times versus frequency. The mapping time increases at the upper frequencies in the <i>Argus</i> band due to higher system temperatures.	156
B.6	(a) G/T_{sys} versus edge taper at 100 GHz. The optimal value is at ~ 18 dB. (b) G/T_{sys} versus frequency. The performance degrades at the band edges.	157
C.1	A schematic of the test setup used to characterize the receiver noise temperature.	159
C.2	A schematic of the spectroscopic Allan variance test setup.	160
C.3	A schematic of the image rejection ratio test setup.	161
D.1	(a) A schematic of the prototype frequency tripler, which utilizes a flip-chip dual diode. The input filter is a stepped-impedance design. A coupled-line filter is included as a part of the output match. (b) A photograph of a prototype test board for the diode tripler.	163
D.2	(a) Output power versus input power with the output frequency at 45 GHz. (b) Output power versus output frequency where the input power is varied between 10–18 dBm in increments of 2 dBm.	165

Chapter 1

Introduction

1.1 Radio and Microwave Astronomy

Astronomy is the study of celestial objects through observation. Astronomical observations are commonly made by detecting the electromagnetic radiation, or light, that is emitted from the object. There is an enormous range of wavelengths at which electromagnetic radiation can be observed. Enumerating from larger wavelengths to smaller ones, the electromagnetic spectrum includes radio waves, microwaves, infrared, visible, ultraviolet, x-ray, and gamma rays as shown in Figure 1.1. Astronomy can be done in any of these wavelength regimes; however, the atmosphere is opaque to many of them. The atmospheric opacity across the electromagnetic spectrum is shown in Figure 1.1. The radio and microwave regimes notably include bands of wavelengths with low atmospheric opacity. These “atmospheric windows” permit observations to be made terrestrially whereas for many other wavelengths the observations must be made above the earth’s atmosphere. This work is focused on imaging specifically in the 3 mm atmospheric window, which spans roughly 67–116 GHz.

Astronomy has existed since ancient civilizations studied the night sky with the naked eye; however, the birth of radio astronomy is much more recent. Radio astronomy began in 1932 when Karl Jansky serendipitously observed radio emission from the Milky Way during a test for Bell Telephone Laboratories. Grote Reber extended Jansky’s pioneering work by building a 9 m telescope in his backyard in 1937. Reber

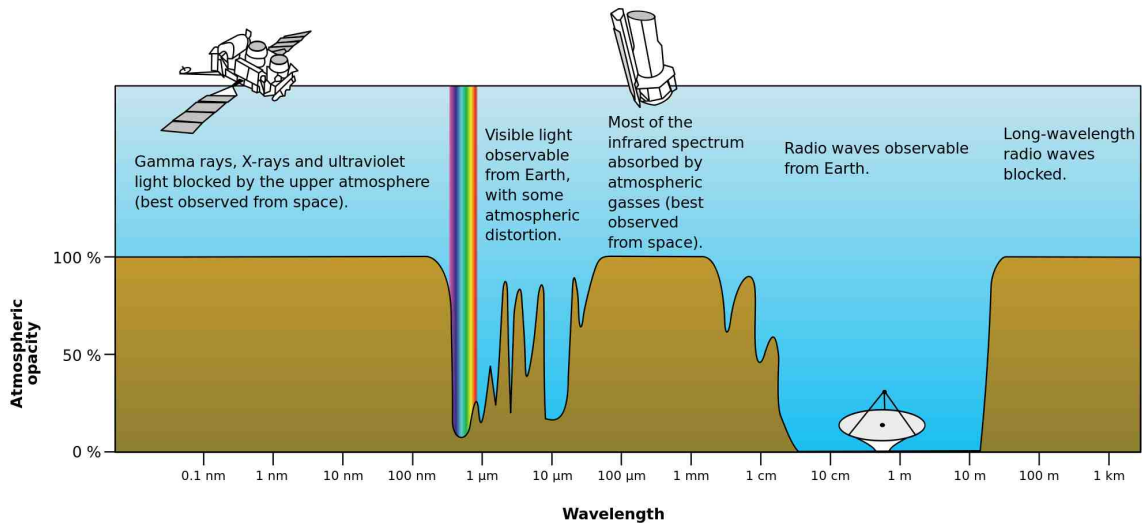


Figure 1.1: The opacity of the Earth’s atmosphere as a function of wavelength. There are “atmospheric windows” at radio and microwave frequencies that allows observations to be made terrestrially. *Argus* utilizes the atmospheric window at around 3 mm. Credit: NASA.

spent the next several years taking a survey of the radio sky, becoming a pioneer in the field of radio astronomy. It wasn’t until after the Second World War that the field started to rapidly grow with researchers building bigger and bigger telescopes and interferometric telescope arrays with larger collecting areas. Moreover, the receivers were built at higher frequencies, with more pixels, and increasingly lower noise. *Argus*, a state-of-the-art receiver for 3 mm imaging, is part of this trend.

1.2 Spectroscopic Science with *Argus*

Argus is designed to image molecular spectral lines in the 3 mm atmospheric window. It is common in radio astronomy to refer to the frequency of radiation instead of the wavelength. The frequency is related to the wavelength through

$$f(\text{GHz}) = \frac{299.792458}{\lambda(\text{mm})} \quad (1.1)$$

The *Argus* instrument specifically targets the 76–116 GHz frequency range of the 3 mm atmospheric window. There are over 2,000 detected molecular lines in this frequency range¹; a subset of these lines that are expected to be common *Argus* targets are listed in Table 1.1. While any of these lines can be observed with *Argus*, the instrument was fine-tuned at the frequencies corresponding to two pairs of spectral lines, HCN & HCO⁺ and C¹⁸O & ¹³CO, whose astrophysical importance is discussed in §1.2.2, §1.2.3, and §1.2.4. Oftentimes the astrophysical emission of these molecular spectral lines is diffuse and has very low surface brightness, which makes them difficult to image in a reasonable amount of time. Historically, millimeter-wave spectroscopic imaging has generally been implemented either over small areas of the sky at high angular resolution or over large areas at moderate to low angular resolution. The Atacama Large Millimeter/submillimeter Array (ALMA)², for example, can achieve very high angular resolution (37 mas to 4.8'' at 110 GHz, depending on the array configuration), but it can image extended emission only across its field of view (57'' at 110 GHz). The Five College Radio Astronomical Observatory (FCRAO), by contrast, has imaged large areas of sky (~ 100 deg²) but at moderate resolution (47'' at 110 GHz) [7]. *Argus*, however, will be capable of imaging low surface brightness emission over large areas of sky (10s to 100s of deg²) and at high angular resolution (7'' at 110 GHz), which will enable new scientific opportunities (§1.2.3).

This section is organized as follows. The physics of molecular spectral lines is covered in §1.2.1, the use of molecular spectral lines as proxies for gas properties is discussed in §1.2.2, and some of the science that will be enabled by *Argus* is discussed in §1.2.3, §1.2.4, and §1.2.5.

1.2.1 Molecular Spectral Lines

Molecules emit photons when they undergo a de-excitation in energy. The wavelength regime of the emission is related to the physics involved in the de-excitation. Transitions in energy levels involving valence electrons in a molecule yield ultraviolet or optical photons, those concerning the vibration of a molecule produce infrared photons, and

¹<http://physics.nist.gov/cgi-bin/micro/table5/start.pl>

²<https://almascience.eso.org/about-alma/alma-basics>

Table 1.1: List of some key transitions from 76–116 GHz. The names of the principal isotopic species are in bold. The *Argus* receiver covers the entire 76–116 GHz range with state-of-the-art sensitivity; however the instrument performance has been fine-tuned for two pairs of lines that are indicated in blue: HCN & HCO⁺ and C¹⁸O & ¹³CO.

Species	Transition	Freq. [GHz]	Species	Transition	Freq. [GHz]
DNC	1–0	76.305	HCO⁺	1–0	89.189
N₂D⁺	1–0	77.109	HNC	1–0	90.664
HDO	1(1,0)–1(1,1)	80.578	¹³ CS	2–1	92.494
HC ¹⁸ O ⁺	1–0	85.162	N₂H⁺	1–0	93.173
HC ¹⁵ N	1–0	86.055	C ³⁴ S	2–1	96.413
H ¹³ CN	1–0	86.340	CS	2–1	97.981
H ¹³ CO ⁺	1–0	86.754	C¹⁸O	1–0	109.782
SiO	2–1	86.847	¹³CO	1–0	110.201
HN ¹³ C	1–0	87.091	C ¹⁷ O	1–0	112.359
C₂H	1–0	87.317	CN	1–0	113.491
HCN	1–0	88.632	CO	1–0	115.271
H ¹⁵ NC	1–0	88.866			

those pertaining to the end-over-end rotations of a molecule give millimeter-wave photons. The molecular transitions that *Argus* is sensitive to, including those in Table 1.1, are not surprisingly almost all rotational transitions. In the subsequent paragraphs, the physics of molecular lines from rotational transitions is discussed following the analysis in [8].

The angular momentum and energy levels of a rotating molecule are quantized because of its quantum mechanical nature. The solution to Schrödinger’s equation for a rotating molecule gives an angular momentum, L , for the molecule as

$$L = n\hbar, \quad n = 0, 1, 2, \dots \quad (1.2)$$

The rotational energy level, E_{rot} , is then

$$E_{rot} = \frac{J(J+1)\hbar^2}{2I}, \quad J = 0, 1, 2, \dots \quad (1.3)$$

where I is the moment of inertia of the molecule and J is an integer that must obey the selection rule $\Delta J = \pm 1$. A transition from energy level J to $J - 1$ therefore

corresponds to a change in energy of $\Delta E_{rot} = \frac{\hbar^2 J}{I}$, which yields a photon of frequency $\nu_{line} = \frac{\hbar J}{2\pi I}$.

Most molecules have a permanent dipole moment that radiates when the molecule rotates³. The line strength from the molecule's dipole radiation can be quantified using mostly classical electrodynamics. The Larmor formula gives the radiated power, P , from an accelerated charge as

$$P = \frac{2q^2 a^2}{3c^3} \quad (1.4)$$

where q is the charge, a is the acceleration, c is the speed of light, and the direction of the radiation is perpendicular to the motion of the charge. The dipole moment, \vec{d} , for a molecule can be found through

$$\vec{d} = \int \vec{x} \rho(V) dV \quad (1.5)$$

It is instructive to consider a dipole that is made up of two equal but opposite charges $\pm q$ that are separated by a distance r_0 . The dipole moment in the rotation plane is then

$$d(t) = qr_0 e^{i\omega t} \quad (1.6)$$

where ω is the angular frequency of the rotation. If the line of sight is along the axis of rotation, then the acceleration of each of the charges perpendicular to the line of sight is

$$a = \ddot{r}(t) = \frac{\partial^2}{\partial t^2} \left(\frac{d(t)}{q} \right) = -\omega^2 r_0 e^{i\omega t} \quad (1.7)$$

The time-averaged radiated power can then be found with Equations 1.7 and 1.4:

$$\begin{aligned} \langle P \rangle &= \frac{2q^2}{3c^3} \omega^4 |r_0 e^{i\omega t}|^2 \\ &= \frac{2q^2}{3c^3} (2\pi\nu)^4 \left(\frac{r_0}{\sqrt{2}} \right)^2 \\ &= \frac{64\pi^4}{3c^3} \nu^4 |\mu|^2 \end{aligned} \quad (1.8)$$

³Importantly, the H₂ molecule does not have a permanent dipole moment.

where $\mu = \frac{q\tau_0}{2}$ is the mean electric dipole moment of the molecule. In practice Equation 1.8 is reasonably accurate, but a more detailed treatment would account for changes in the distance between atoms due to different centrifugal forces at different energy levels.

The molecules in astronomical gases are typically excited primarily through collisions and de-excited via spontaneous emission of photons. In practice, different molecules are collisionally excited at different density thresholds. This difference between molecules can be explained by considering the rates of excitation and de-excitation in a system that has both collisional and radiative effects. Equation 1.9 shows that in a steady state system the rate of excitation for a molecule equals the rate of de-excitation (see *e.g.* [9]):

$$n_i \left[\sum_{j<i} A_{ij} + \sum_j (B_{ij}U_\nu + \gamma_{ij}n_{col}) \right] = \sum_{j>i} n_j A_{ji} + \sum_j n_j (B_{ji}U_\nu + \gamma_{ji}n_{col}) \quad (1.9)$$

where n_i (n_j) is the density of the molecule in level i (j), n_{col} is the density of all possible collision partners including other types of molecules (in practice mostly H_2), A_{ij} is the Einstein coefficient for spontaneous emission, B_{ij} and B_{ji} are the Einstein coefficients for stimulated emission and absorption, U_ν is the radiant energy density per unit bandwidth, and γ_{ji} is the rate of collisions per unit density that lead to electronic excitation of a molecule. When $i > j$, the left-hand and right-hand sides of the equation correspond to de-excitations and excitations, respectively. In the case where stimulated emission and absorption are subdominant, Equation 1.9 is satisfied when n_{col} is equal to the critical density, n_{crit} :

$$n_{crit} = A_{ij}/\gamma_{ji} \quad (1.10)$$

A molecule in a gas with density greater than or equal to n_{crit} is said to be “thermalized” and emits significantly due to collisional excitations. However, this calculation for the critical density is only a rough approximation. It is assumed that the molecule is a two-level system and that the molecular gas is optically thin. Both of these approximations lead to overestimates of the critical density. A more accurate calculation that takes

these effects can be found in [10].

The average rate of spontaneous emission for a collection of molecules is given by the Einstein A coefficient, which can be solved for via $A_{ij} = \langle P \rangle / h\nu_{ij}$. The critical density can therefore be expressed using Equation 1.8 as

$$n_{crit} = \frac{64\pi^4}{3hc^3\gamma_{ji}}\nu^3|\mu|^2 \quad (1.11)$$

It follows that molecules with larger dipole moments require higher densities to thermalize. Consequently, environments with higher densities can be probed by mapping molecules with higher dipole moments. *Argus* will exploit this technique by using observations of multiple molecular spectral lines to explore the physical conditions in star-forming molecular clouds as discussed in §1.2.2.

1.2.2 Gas Tracers

One of the primary science goals of *Argus* is to study star formation processes in the Milky Way and nearby galaxies through millimeter-wave molecular spectroscopy. Molecular clouds are the birthplaces of stars in our universe. The most abundant molecule in molecular clouds is H_2 ; however, its rotational transitions require high temperatures to excite due to its low mass and lack of a permanent dipole moment and so it is mostly invisible in cold molecular clouds. Fortunately there are many other molecules in molecular clouds that are visible, although most of them are faint. Table 1.1 gives a list of some of the key molecular spectral lines that will be visible in the *Argus* passband. Many of these molecular spectral lines are used as proxies for the properties of the molecular gas; these lines are known as “tracers”. Carbon monoxide (CO) is the next most abundant molecule after H_2 and its spectral lines are the brightest. CO and its isotopologues are very common tracers of the total molecular gas content and reveal the overall structure and dynamics of molecular clouds. Molecules with higher dipole moments (*e.g.* HCN, HCO^+ , HNC, N_2H^+ , and CS) trace molecular gas with higher densities as indicated by Equation 1.11, but these lines are an order of magnitude fainter than CO [11]. High density gas tracers can probe the protostellar cores within molecular clouds and are discussed in more detail

in §1.2.3. The critical densities for a number of common tracers are listed in Table 1.2 ordered by increasing critical densities, which illustrates that it is possible to probe a large range of densities by observing an appropriate selection of molecules with different critical densities.

Table 1.2: Table of the Einstein A coefficients for spontaneous emission, the collision rates (γ), and the critical densities (n_{crit}) for some of the key molecular spectral lines for *Argus* science. The data were retrieved from the Leiden Atomic and Molecular Database [1] for a gas temperature of 100 K. The frequency for these transitions are given in Table 1.1. The critical density (*i.e.* the density at which the spectral line is thermalized and therefore emits significantly) is calculated from Equation 1.10, which assumes that the gas is optically thin. The table is ordered by increasing critical densities. In practice, many *Argus* observations will target multiple lines in order to explore different density regimes.

Molecule	Transition	Einstein A (s^{-1})	γ (cm^3s^{-1})	n_{crit} (cm^{-3})
C^{18}O	1–0	6.266×10^{-8}	3.506×10^{-11}	1.787×10^3
^{13}CO	1–0	6.294×10^{-8}	3.506×10^{-11}	1.795×10^3
CO	1–0	7.203×10^{-8}	3.506×10^{-11}	2.054×10^3
N_2H^+	1–0	3.628×10^{-5}	1.8×10^{-10}	2.015×10^5
HCO^+	1–0	4.251×10^{-5}	1.8×10^{-10}	2.362×10^5
HNC	1–0	2.690×10^{-5}	6.53×10^{-11}	4.119×10^5
CS	2–1	1.679×10^{-5}	2.44×10^{-11}	6.881×10^5
HCN	1–0	2.408×10^{-5}	9.04×10^{-12}	2.663×10^6

1.2.3 Star Formation Relations

In order to model the evolution of galaxies it is useful to have a recipe for star formation. Since stars form from molecular gas, a good starting point is to understand the relationship between star formation rates and molecular gas densities. Starting with Schmidt in 1959 [12], most global star formation studies have focused on finding empirical relations for the star formation rate that are averaged over entire galaxies. A particularly significant example of this is the Kennicutt-Schmidt (KS) law [13], which states that the star formation rate per unit area, Σ_{SFR} , scales with the surface density

of the molecular gas, Σ_{gas} , through a power-law relationship:

$$\Sigma_{SFR} \propto \Sigma_{gas}^N \quad (1.12)$$

In practice the far-infrared luminosity, L_{IR} , is commonly used as a proxy for the star formation rate and the CO luminosity, L_{CO} , is used as a tracer for the total molecular gas mass. Kennicutt found that $N = 1.40 \pm 0.15$ is obtained from measurements of L_{IR} and L_{CO} in local galaxies [13].

The KS law (Equation 1.12) is useful for coarse predictions of the star formation efficiency in a galaxy, but it has a number of shortcomings. Firstly, the power law index depends upon on the sample of galaxies measured. Gao & Solomon [11] compared the star formation rate and the molecular gas surface density for a sample of galaxies different from that of Kennicutt. They calculated a power-law index of $N = 1.25 \pm 0.08$, which is inconsistent with Kennicutt’s value of 1.40; however, they found that the index is mostly set by the galaxies in their sample with large star formation rates, namely the luminous infrared galaxies (LIRGs) with $L_{IR} > 10^{11} L_{\odot}$ and ultraluminous infrared galaxies (ULIRGs) with $L_{IR} > 0.8 \times 10^{12} L_{\odot}$. A modification in the number of LIRGs and ULIRGs relative to the number of normal galaxies in the Gao & Solomon sample can reproduce the Kennicutt index of ~ 1.40 . Excluding the LIRGs and ULIRGs from the sample completely yields an approximately linear relationship between L_{IR} and L_{CO} , while many of the LIRGs and ULIRGs have L_{IR}/L_{CO} ratios that are roughly an order of magnitude higher than normal galaxies. Large L_{IR}/L_{CO} ratios indicate substantial amounts of star formation per unit of molecular gas mass, which is to say that the efficiency of star formation is high. This high efficiency mode of star formation is known as a “starburst”. The vastly different star formation efficiencies of normal galaxies and starburst galaxies suggests that the KS law should consider them separately, which limits its utility since it is not known a priori which galaxies have a starburst mode of star formation. A second issue with the KS law is that most of the molecular gas in galaxies is inert; star formation occurs primarily in the small fraction of regions with high surface density. The KS law, which was empirically determined with low resolution observations, implies an artificially low star formation efficiency

because of this abundance of inert gas that is detected at these scales. At higher resolutions, on the other hand, the KS law breaks down. For example, the KS law was found to underpredict the star formation rate in molecular clouds in the Milky Way by as much as a factor of 17 [14]. Moreover, the KS law was found to break down on scales below ~ 80 pc in M33 [15], which is roughly the size of molecular clouds. While the KS law does a reasonable job of predicting the star formation rate for entire galaxies or large ensembles of molecular clouds, it is not a fundamental relation that holds for all star forming regions.

It has been shown that HCN, which traces dense gas cores, correlates more closely with star formation than CO [11] and overcomes the aforementioned shortcomings of the KS law. Specifically, the star formation rate is related to dense gas via a modified version of Equation 1.12 where $N = 1.00 \pm 0.05$. The tight linear relationship between star formation rate and dense gas suggests that the dense gas, which make up the “cores” that are precursors to stars, is a fundamental ingredient for star formation. This relation holds true even for LIRGs and ULIRGs, which implies that galaxies with high star formation rates simply have more dense gas and that the high L_{IR}/L_{CO} ratio of some LIRGs and ULIRGs is due to high dense gas fractions in these galaxies as traced by the L_{HCN}/L_{CO} ratio⁴. In fact, it is possible to identify starburst modes of star formation simply by locating areas with high L_{HCN}/L_{CO} ratios⁵. The linear correlation of star formation and dense gas also holds true for areas in the Milky Way [17]. Discrepancies of the KS law in the Milky Way can be explained by the vastly different dense gas ratios in different environments [14].

Argus observations will uncover the extent to which environmental factors affect the amount of star formation in different molecular gas cores. The dense gas mass has been shown to be a good tracer for star formation at the spatial scales of molecular clouds (10s to 100s of pc) and below. Consequently, it has been suggested that dense gas cores of size ~ 0.1 pc might be the fundamental units of star formation and that the star formation rate of a region can be crudely determined by counting the number

⁴The mechanism for starbursts was not clear from measurements of just IR and CO luminosities. It was long thought that starburst galaxies might have different energy sources than normal galaxies (*e.g.* dust-enshrouded AGNs [16]) before the essential role of dense gas became clear.

⁵It is suggested in [11] that $L_{IR}/L_{CO} > 0.06$ is a good criterion for starburst galaxies.

of cores [18]; however, recent observations have shown that the dense gas fraction and the star formation efficiency (*i.e.* the amount of star formation per dense gas mass) varies systematically within galaxies [19, 20]. Specifically, observations of M51 suggest that pressure is an important environmental factor that contributes to the star formation efficiency [20]. *Argus* observations of different types of galaxies with a variety of tracers will uncover additional details on what sets the dense gas fraction and how star formation in dense gas depends on the particulars of the local environment such as temperature, density, electric and magnetic fields, turbulence, gravitational boundedness, and ionization state. Such detailed information about star formation in the Milky Way and nearby galaxies is critical for understanding galaxy-scale star formation through the universe and throughout cosmic time.

1.2.4 Filaments

Understanding the structure and dynamics of molecular clouds is another important factor that is required to accurately model the evolution of galaxies. Infrared observations with Herschel revealed that filamentary structures in molecular clouds are ubiquitous [21, 22, 23]. Spectroscopic measurements of filaments are an important supplement to the Herschel continuum images because they provide velocity information for the filaments that reveal how they evolve. Early spectroscopic measurements on molecular clouds have already been made. The Taurus molecular cloud was surveyed in ^{12}CO and ^{13}CO with the SEQUOIA focal plane array on the 13.7 m Quabbin millimeter wave telescope [24]. These observations revealed a complex structure of filaments, cavities, and rings that were instrumental to understanding the dynamics of the molecular cloud. *Argus* on the GBT has 7 times better resolution than the SEQUOIA observations, which will allow the filaments and dense cores to be better resolved, revealing a more complete picture of the ongoing phenomena. One of the foremost goals in studying filaments is to understand the link between the filaments, the large scale processes in the interstellar medium, and the dense molecular gas cores that are precursors to stars. *Argus* is well-suited to this goal because it can map large areas of sky at high angular resolution and will therefore capture phenomena that

happen across a wide range of spatial scales.

There are a number of ideas about the function of filaments in star formation that can be tested with *Argus*. The Herschel images show that the main filaments have many smaller filaments, called striations, that run roughly perpendicular to the main filament. The striations are aligned along the magnetic field lines and are perhaps the vehicle for mass accretion onto the molecular clouds. Accretion driven turbulence might play an important role in regulating the rate of star formation in molecular clouds [25] and filamentary structures could significantly enhance the total accretion rate. *Argus* observations will be able to verify whether and how this mass accretion happens. Dense molecular gas cores are likely formed by axial instabilities along the filamentary structures. *Argus* observations will be able to test theoretical models of the collapse of the filament into cores (*e.g.* [26, 27]).

1.2.5 Other Science

Comets

The structure and composition of comets contain information about the conditions in the outer solar system when it formed [28]. Spectroscopic imaging of the the gaseous atmosphere of the comets, which is known as the coma, can reveal its constituent materials. Comets from different heliocentric distances have significantly different compositions, which reflect the environment and temperature where they were formed; however, the sample size of observed comets is small because most comets have very low surface brightness. Moreover, comets are difficult to image because they rotate relatively quickly and therefore require fast mapping speeds in order to capture the comet in a relatively fixed orientation. *Argus* will enable several comets per year to be imaged spectroscopically, which will vastly improve the state of knowledge on the formation of the solar system.

Astrochemistry and Astrobiology

The detection of complex organic molecules in the interstellar medium yields clues about the dominant chemical pathways in these regions. The interstellar medium has

a very low density, which is not practical to reproduce in labs. The low densities, in addition to the presence of weakly ionized gas and magnetic fields, lead to chemical pathways that are very different from those on earth. Recent observations on the GBT below 50 GHz have discovered new interstellar molecules that emit across arcminute spatial scales [29, 30, 31, 32]. *Argus* will extend this effort by searching for complex molecules with transitions in the 3 mm regime. These observations are technically challenging because of the low surface brightness of the molecular lines and the large spatial scales (based on the aforementioned detections) and require instruments with exquisite mapping speeds such as *Argus*.

A subset of the detected complex interstellar molecules are important for understanding the origins of life. The simple sugar glycolaldehyde, which is likely a precursor to RNA [33], was detected at the GBT at four rotational transitions between 13.5 and 22.1 GHz [30]. Additionally, acetamide and formamide, the only known interstellar molecules with peptide bonds⁶, were discovered at the GBT at transition frequencies below 50 GHz [32]. *Argus* will be used to search for other precursors to important biological molecules for the formation and evolution of life.

⁶A peptide bond links amino acids to form proteins.

Chapter 2

The *Argus* Instrument

This chapter provides an overview of the *Argus* instrument, which is a cryogenic 16-pixel millimeter-wave spectrometer. The chapter is organized as follows. The roles of the *Argus* team members are summarized in §2.1. The *Argus* receiver architecture is presented in §2.2. A discussion of the importance of the instrument sensitivity, the conventions used for quantifying noise, and the requirements for minimizing the instrument noise in a system like *Argus* is provided in §2.3. The instrument specifications are delineated in §2.4. The *Argus* instrument and its subsystems are described in §2.5. Finally, a description of the *Argus* prototypes and their differences from the production design are given in §2.6.

2.1 The *Argus* Collaboration

Argus was deployed to the 100 m Robert C. Byrd Green Bank Telescope (GBT) in early 2016 after roughly two years of integration and testing. The *Argus* instrument was built by a collaboration that involved individuals from Stanford, the California Institute of Technology (Caltech), the Jet Propulsion Laboratory (JPL), the University of Maryland, the University of Miami, and the National Radio Astronomy Observatory (NRAO). The contributions of different members of the collaboration are summarized in Table 2.1. I personally played a leading role in developing the cryogenic focal plane array, integrating the subsystems into a working array, testing the array in lab,

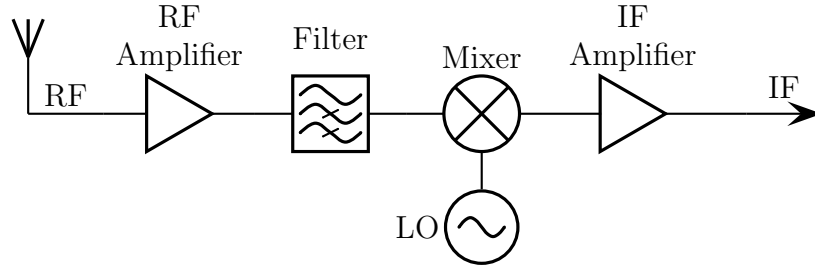


Figure 2.1: A schematic for a simple heterodyne receiver. Impinging radiation is collected with an antenna. The signal is then amplified, filtered, and downconverted by mixing the input RF signal with a reference LO signal (§2.2.2).

commissioning *Argus* on the telescope and managing the project.

2.2 Receiver Architecture

2.2.1 Heterodyne Receivers

The *Argus* receiver array utilizes a heterodyne receiver architecture. In this architecture a radio frequency (RF) input signal is amplified and downconverted to an intermediate frequency (IF). The low frequency IF is easier to process than the input RF for a number of reasons: the ohmic losses are lower, the feature size in custom electronics designs is larger (due to the longer wavelength) and therefore they are cheaper and easier to fabricate, and off-the-shelf components at these frequencies are cheaper and more readily available. A schematic for a simple heterodyne receiver is shown in Figure 2.1. The frequency downconversion is accomplished through a component known as a mixer, which is discussed in §2.2.2. The architecture also includes a receiving antenna, low-noise amplifiers (LNAs), and filters.

2.2.2 Mixers

A mixer is a device that is used to shift the frequency range of a signal. A perfect mixer takes an input signal $s_{IN}(t)$ and multiplies it by a reference tone $r_{LO}(t)$, which is known as the local oscillator (LO). The input signal s_{IN} can in general be represented

Role	Primary Person/Institution	Contributing
Receiver Integration		
Lab Integration and Testing	Matt Sieth (Stanford)	Kiruthika Devaraj (Stanford) Dongwoo Chung (Stanford)
Subsystems		
Cryostat	Joshua Gunderson (University of Miami)	Matt Sieth (Stanford)
Optic Design	Matt Sieth (Stanford)	
Window	Joshua Gunderson (University of Miami)	
Feeds	Patricia Voll (Stanford)	
Modules	Rohit Gawande (Caltech) Kieran Cleary (Caltech)	Matt Sieth (Stanford) Lorene Samoska (JPL) Pekka Kangaslahti (JPL)
Multilayer Routing Boards	Matt Sieth (Stanford)	
Flexible Circuitry	Andrew Harris (University of Maryland)	Matt Sieth (Stanford)
Monitor and Control Systems	Andrew Harris (University of Maryland) Justin Richmond-Decker (NRAO)	
Calibration	Andrew Harris (University of Maryland)	
LO System	Matt Sieth (Stanford) Jacob Kooi (Caltech)	Kiruthika Devaraj (Stanford) Dongwoo Chung (Stanford)
Warm IF System	Rohit Gawande (Caltech)	
Project Management		
	Sarah Church (Stanford) Kiruthika Devaraj (Stanford) Matt Sieth (Stanford)	David Frayer (NRAO)

Table 2.1: The distribution of work for the *Argus* collaboration.

as a Fourier sum of sine waves:

$$s_{IN}(t) = \sum_n A_n \sin(2\pi f_{IN,n}t) \quad (2.1)$$

where A_n and f_n^{IN} are the amplitude and frequency, respectively, of the n th component. Considering just a single component of the input signal, the result of the mixer multiplication yields

$$\begin{aligned} s_{OUT} &= s_{IN}(t) \times r_{LO}(t) \\ &\propto \sin(2\pi f_{IN}t) \sin(2\pi f_{LO}t + \phi) \\ &= \frac{\cos(2\pi(f_{IN} - f_{LO})t - \phi) - \cos(2\pi(f_{IN} + f_{LO})t + \phi)}{2} \end{aligned} \quad (2.2)$$

where f_{IN} and f_{LO} are the frequencies of the input and LO, respectively, and ϕ is the phase difference between the two signals. For a given f_{IN} and f_{LO} , the output signal has two frequency components: $|f_{IN} \pm f_{LO}|$. The high frequency component can be filtered out, which leaves just the downconverted IF signal: $|f_{IN} - f_{LO}|$. In practice the input signal is composed of a contiguous band of frequencies ($f_{IN,n}$ in Equation 2.1) that are shifted together into the IF band. A given IF frequency band can be generated from input frequencies that are either lower or higher than the local oscillator frequency; these are known as the lower and upper sidebands, respectively. A pictorial of the shifting frequency bands is shown in Figure 2.2.

The *Argus* mixer is subharmonically pumped, which is subtly different from the basic mixer described above. Mixing requires a nonlinear device – typically a diode or a transistor – that combines the f_{IN} and f_{LO} signals. A perfect mixer can be implemented by combining these two signals and then passing them through a square-law device:

$$\begin{aligned} s_{OUT} &= (s_{IN}(t) + r_{LO}(t))^2 \\ &= s_{IN}^2(t) + r_{LO}^2(t) + 2(s_{IN}(t) \times r_{LO}(t)) \end{aligned} \quad (2.3)$$

The first two terms of Equation 2.3 are much higher in frequency than the IF and

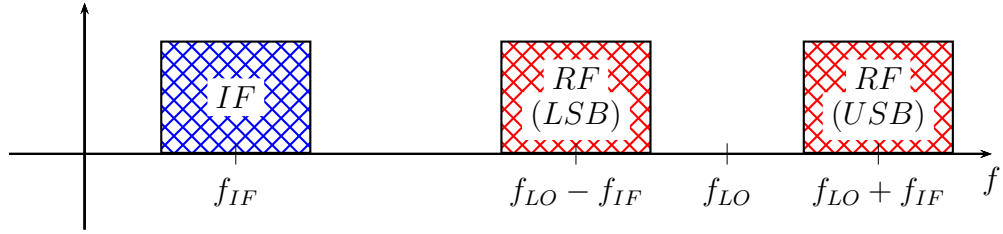


Figure 2.2: A mixer downconverts the input radio frequency (RF) signal, which is shown in red, by multiplying the input signal with a reference tone, known as the local oscillator (LO). The output signal, or intermediate frequency (IF), is shown in blue and has a frequency that is the difference of the LO and RF frequencies. The IF also has a high frequency component from the sum of the LO and RF frequencies, which is typically rejected through filtering. The frequency of the RF signal can be either above or below the LO frequency, which are known as the upper sideband (USB) and lower sideband (LSB). The upper and lower sidebands get converted into the same IF frequency range, which means that at a given IF frequency it is impossible to determine which sideband the signal is from unless the sidebands are separated using one of the techniques discussed in §2.2.2.

can be easily filtered out. With this assumption, the square-law device mixing scheme reduces to Equation 2.2. While a square-law device is a common choice for mixing, it is in general possible to use an arbitrary polynomial in a similar manner to Equation 2.3. In these cases, the IF frequency is given by

$$f_{IF} = |mf_{IN} - nf_{LO}| \quad (2.4)$$

where m and n are integers. For the mixers in *Argus*, $m = 1$ and $n = 2$.

For a broadband input signal, the lower and upper sidebands in Eq. 2.2 are folded together at the IF output and are therefore indistinguishable. This can be problematic in astronomical observations when one of the sidebands contains the desired signal while the other sideband has a contaminating source of noise, which is called the image. There are two commonly used techniques for discriminating between the two sidebands as depicted in Figure 2.3. In the first, the undesired sideband is filtered out before the input of the mixer. The output has just a single sideband in this case and the image rejection is determined by the quality of the filter. The second method relies on two mixers that are operated 90° out of phase. The sidebands in each mixer are folder

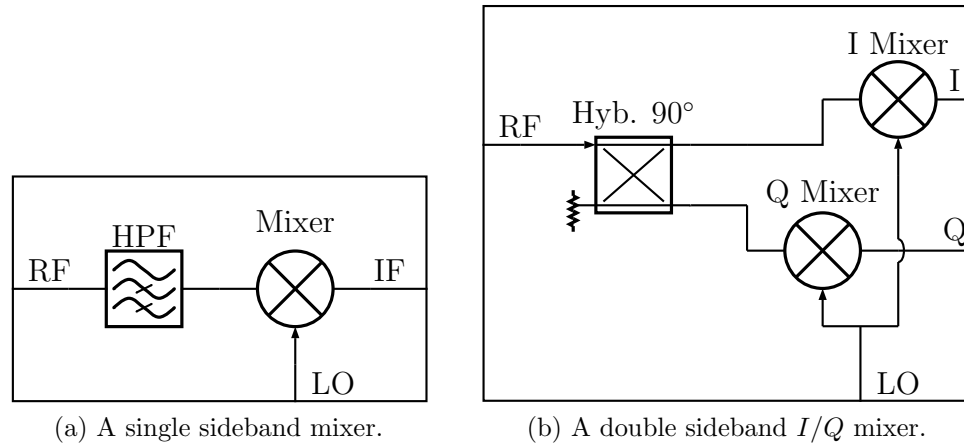


Figure 2.3: Two mixer architectures. An ideal mixer is simply a multiplier that multiplies the input with the local oscillator; the low frequency IF output contains both the upper- and lower-sidebands folded together. These architectures take different approaches to unfolding the sidebands. (a) In the single sideband design, one of the sidebands is filtered before it impinges on the mixer. (b) In the double sideband I/Q mixer the sidebands are folded together in two different mixers with orthogonal linear combinations so that the sidebands can later be separated either with a hybrid or in software.

together, but the relative phase between the upper and lower sidebands is different for each mixer. This allows for the sidebands to be separated with either hardware or software. Details of this procedure are given in §5.1.7. This second method is known as an I/Q mixing scheme, which refers to the in-phase and quadrature-phase mixers. The advantage of the I/Q scheme is that it yields twice the instantaneous bandwidth since both of the sidebands are processed; however, it is more complex to implement since there are twice as many mixers and output signals. Both methods were used in prototyping components, but the *Argus* receiver implements an I/Q scheme for the advantages described here.

2.3 Sensitivity

The *Argus* science objectives (§1.2) require the receiver to have state-of-the-art sensitivity so that it can quickly map large areas of low surface brightness emission on

the sky. The *Argus* instrument noise is characterized in units of noise temperature, which is covered in §2.3.1. Achieving low receiver noise temperatures is important in order to minimize the total observing time for an observation, which is presented quantitatively in §2.3.2; however, in a system of many cascaded components like *Argus*, minimizing the receiver noise temperature can be challenging as is discussed in §2.3.3.

2.3.1 Noise Temperature

In radio astronomy, noise temperature is used to describe the strength of noise-like signals. Noise temperature is defined as the temperature at which Johnson-Nyquist noise (*i.e.* the power that a resistor emits at a given physical temperature) would equal the noise from the device under test. At low frequencies – including the radio and microwave regimes – this noise power, P_N , can be approximated¹ as $P_N = kBT_N$ where k is the Boltzmann constant, B is the measurement bandwidth, and T_N is the noise temperature. It follows that the noise temperature is given by

$$T_N = \frac{P_N}{kB} \quad (2.5)$$

The noise temperature and gain of a device like the *Argus* receiver can be characterized via a standard technique known as the Y-factor method that involves comparing the response of the receiver to different input noise powers that are known. The Y-factor procedure is described in detail in Appendix A. The receiver temperature for an average *Argus* pixel is 39–65 K (§5.1.1), which is expected to translate to a system temperature of 100–255 K on the sky at zenith (§5.1.2).

2.3.2 The Radiometer Equation

The Rayleigh-Jeans sensitivity, ΔT_{\min} , for an observation with a single pixel is given by the radiometer equation:

$$\Delta T_{\min} = \frac{T_{\text{sys}}}{\sqrt{\Delta\nu\tau}} \quad (2.6)$$

¹This is the Rayleigh-Jeans approximation.

where ΔT_{\min} is the equivalent temperature of the minimum detectable signal, T_{sys} is the system noise temperature of a receiver, which is the sum of the receiver noise temperature and atmospheric contributions to the system noise, $\Delta\nu$ is the spectral resolution, and τ is the integration time for the observation. The mapping speed for imaging a large region scales approximately with $n_{\text{pix}}/(\Delta T_{\min})^2$ where n_{pix} is the number of pixels. Fast mapping speeds can therefore be achieved with focal plane arrays with a large number of pixels and low system temperatures.

2.3.3 Friis Equation

One of the foremost challenges in integrating all of the receiver components is minimizing the receiver noise temperature. The receiver noise temperature for a series of N cascaded components is given by the Friis equation:

$$T_{Rx} = T_1 + \sum_{i=2}^N \frac{T_i}{\prod_{j=1}^{i-1} G_j} \quad (2.7)$$

where T_i and G_i are the noise temperature and gain, respectively, of the i^{th} component. For a heterodyne receiver like the one illustrated in Figure 2.1, Equation 2.7 becomes

$$\begin{aligned} T_{Rx} = T_{RF} &+ \frac{T_{Amplifier,RF}}{G_{RF}} \\ &+ \frac{T_{Mixer}}{G_{RF}G_{Amplifier,RF}} \\ &+ \frac{T_{Amplifier,IF}}{G_{RF}G_{Amplifier,RF}G_{Mixer}} \end{aligned} \quad (2.8)$$

where the subscript RF corresponds to all components that are before the RF amplifier such as the window, the antenna, and transmission lines. The other subscripts correspond directly to the labeled components in Figure 2.1². If the RF amplifiers have sufficiently high gain ($G_{Amplifier,RF}$), then only the first two terms in Equation 2.8 contribute to the receiver noise temperature. In an ideal heterodyne receiver the receiver noise temperature would simply be the noise temperature of the first RF

²The filter has been assumed to have negligible loss.

amplifier; however, components preceding the amplifiers in general have a non-negligible noise contribution that adds to the total system noise. Additionally, lossy components (i.e. those with $G < 1$) have a multiplicative contribution that increases the noise contribution of subsequent components. It is therefore imperative that any component that precedes the low-noise amplifiers have both low loss and noise. In the case where these contributions are minimized, the system noise temperature is dominated by the low-noise amplifiers.

2.4 Specifications

The *Argus* receiver array is designed to make single-polarization observations in the 76–116 GHz band, which is rich with molecular spectral lines including the astronomically important $^{12}\text{CO}(1-0)$ and $\text{HCN}(1-0)$ lines. The following sections detail the specifications that are needed to achieve the *Argus* science objectives (§1.2) with the rationale behind each one explained. A summary of the specifications is given in Table 2.2.

Table 2.2: Specifications for the *Argus* array.

<i>Argus</i> Specifications	
Number of Pixels	16
RF Input	76–116 GHz
LO Input	39–59 GHz
IF Output	0.90–2.15 GHz
Angular Resolution	7" at 100 GHz
Polarizations	1
Receiver Temperature	<60 K per pixel
Image Rejection Ratio	>10 dB required, >13 dB preferred
Dynamic Range	>5 dB linear at $T_A = 300$ K
IF Power	>-5 dB
Passband Slope	<10 dB
Gain Stability (Allan time)	$\tau_A > 30$ s

2.4.1 Number of Pixels

The number of pixels for *Argus* was chosen to match the 16 available channels in the GBT backend (§2.5.4). The GBT focal plane could in principle accommodate a kilo-pixel millimeter-wave array, but the GBT backend would need to be upgraded to be able to read out all of the channels. It is conceivable that *Argus* could eventually be upgraded to perhaps a 100-pixel array with a corresponding upgrade to the capabilities of the GBT backend. The feasibility of such an upgrade is discussed in §2.4.11.

2.4.2 RF and LO Input

Argus was designed to observe molecular spectral lines that are relevant to star formation, comets, and the interstellar medium (§1.2). There are a high density of such lines in the 76–116 GHz *Argus* frequency range (see *e.g.* Table 1.1). An emphasis was placed on being able to observe HCN (88.632 GHz) and HCO⁺ (89.189 GHz), which are important dense gas tracers, and C¹⁸O (109.782 GHz), ¹³CO (110.201 GHz) and CO (115.271 GHz), which will be used to probe the structure and dynamics of molecular gas. There are even more spectral lines just below the *Argus* RF range that would also be useful for astronomers. For example, singly deuterated molecules (*e.g.* DCO⁺ at 72 GHz, DCN at 72 GHz, DNC at 76 GHz and NHD₂ at 67.8 GHz) are very useful for observing cold dense cores since they undergo an abundance enhancement in cold clouds due to fractionation [34]; however, there were hardware limitations that limited *Argus* from achieving even larger bandwidth. Namely the lower frequency bound is set by the LO chain; there are a number of commercial components that have a nominal frequency range of 40–60 GHz. The upper frequency is limited by the performance of the low-noise amplifiers inside the miniaturized receiver modules (§3.2.1); however, there is no need to try to push this higher as there is an atmospheric oxygen line that precludes observations.

2.4.3 IF Output

The *Argus* IF chain was designed to interface with the existing infrastructure at the GBT. The VEGAS spectrometer (§2.5.4) can process an instantaneous bandwidth of

1.25 GHz, which was therefore adopted as the *Argus* IF bandwidth.

Argus could in principle be modified to achieve higher instantaneous bandwidths. This could be useful for observing continuum radiation in front of point sources (*e.g.* quasars or HII regions). In the cryogenic focal plane, the IF filters and warm IF amplifiers are the bandwidth limiting components; however, these could be swapped out for higher bandwidth components in a potential future upgrade. The VEGAS spectrometer already supports a mode where two channels are read out over 10 GHz bandwidth. Two of the pixels could therefore be used in a high bandwidth mode. For point source observations, position switching between the two pixels could be implemented for sky subtraction.

2.4.4 Receiver Temperature

The noise temperature from the receiver limits the sensitivity of observations (§2.3). Most of the molecular spectral lines targeted by *Argus* are faint and extended. In order to map these lines efficiently, state-of-the-art receiver noise is required. The specification for the receiver temperature is 60 K. The receiver temperature that was measured in the lab for an average pixel was 39–65 K over the RF passband (§5.1.1).

2.4.5 Angular Resolution

The Green Bank Telescope will provide an angular resolution of about 7'' at 100 GHz. The resolution will be sufficient to resolve star-forming cores in the Milky Way, which are the smallest units of star formation, and molecular clouds in nearby galaxies. This resolution also overlaps with the angular scales from interferometric arrays such as CARMA, PdBI, and ALMA, which have superior angular resolutions but cannot resolve extended emission. It will therefore be possible to combine *Argus* data with interferometric datasets to attain much greater spatial dynamic range.

2.4.6 Polarizations

Argus is designed to measure a single linear polarization. In principle, it would be straightforward to build an *Argus*-like instrument with dual-polarization by adding a polarizer after the feedhorn; however, this would require twice as many heterodyne receiver chains per pixel, which would impose a couple of additional design considerations. Namely, a given backend could only support half the number of pixels; at the GBT a dual-polarization *Argus*-like instrument could presently only have 8 pixels. A more minor consideration is that the cross-sectional size of each receiver chain would have to be reduced or the pixel-to-pixel spacing would have to be increased. Another downside to dual-polarization is that the polarizer would add ohmic loss, which would degrade the system temperature of the *Argus* pixels.

2.4.7 Image Rejection Ratio

The *Argus* instrument is composed of heterodyne receivers that downconvert the impinging millimeter-wave signals (§2.2). The output of the receivers has two sideband components, which correspond to different RF input frequencies. The sidebands are separated before being read out, however, in practice they cannot be disentangled perfectly. The undesired sideband is known as the image; the image rejection ratio is simply the ratio between the signal and image powers.

Poor image rejection ratio has a couple of practical consequences for observations. The foremost concern is that the sensitivity is degraded because the image contributes additional noise to the signal chain. Another issue is that spectral features at the image frequency will contaminate the measurement of the signal frequency. In practice, this effect can be mitigated by making sure that the image frequency is devoid of significant signals. Both of these phenomena are reduced significantly if the specification of 10 dB image rejection ratio is met.

2.4.8 Dynamic Range

The *Argus* instrument needs to stay in its linear regime as it looks at different input levels. In particular the linearity requirement must hold when *Argus* changes from

observing the cold sky to the ambient temperature calibration vane. The calibration procedure will allow for the raw data to be converted into flux densities. If *Argus* were to become nonlinear during the calibration procedure then the flux densities of the reduced images would be systematically offset from the true values. The necessary dynamic range to avoid such problems is at least about 5 dB, which is the expected ratio of the system temperature between observing cold sky and the ambient temperature calibration load.

2.4.9 Passband Slope

Argus uses the VEGAS backend at the GBT, which is discussed in §2.5.4. The VEGAS backend is capable of handling input signals with a maximum of 20 dB of slope, but it is recommended to keep the slope less than 10 dB.

2.4.10 Gain Stability

Gain instabilities in the receiver adversely affect the instrument's sensitivity. The fluctuations in gain add to the radiometric noise of the receiver quadratically:

$$\sigma_T = \sqrt{\frac{1}{\Delta f \tau} + \left(\frac{\Delta G}{G}\right)^2} \quad (2.9)$$

where σ_T is the measurement uncertainty, Δf is the bandwidth, τ is the integration time and G is the receiver gain.

The Allan time, τ_A , is the integration time for which the radiometric noise power equals the power from $1/f$ noise and low frequency drift. The Allan time dictates the scan strategy for observations; the maximum scan time in between observations is proportional to the Allan time. Therefore the observing efficiency is improved with longer Allan times. The 30 s Allan time specification allows for scan times on the order of minutes as discussed in detail in §5.2; however, care must be taken to translate properly between Allan times measured in the laboratory and those expected on the sky (§5.1.6).

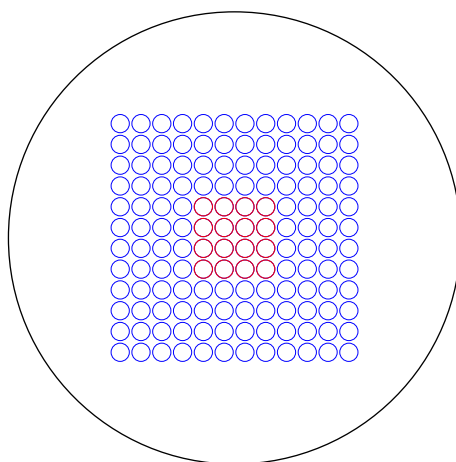


Figure 2.4: The footprint of the *Argus* array relative to the 24" turret hole through which the receiver is mounted. The black circle represents the turret hole. The red circles represent the physical size of the *Argus* feedhorn antennas, which are packed in a 4x4 square array. The *Argus* receiver occupies a small fraction of the available space in the turret hole. In principle a 144-pixel *Argus*-like array (*i.e.* 9 copies of *Argus* tiled together) would fit easily into this space, which is indicated by the blue circles.

2.4.11 Scalability

The 16-pixel *Argus* array is a powerful tool for molecular spectroscopy, but it also serves as a proof-of-concept for larger format future instruments. The *Argus* array was designed to have 4-pixel sub-units (§2.5.1) that could in principle be used as the building blocks for a future array with hundreds of pixels. Moreover, the instrument sub-components were designed with an emphasis on technology that would be scalable to much larger arrays. Preference was given to designs that are mass-producible or economical to manufacture. The feedhorn antennas have a smooth-walled design that make them straightforward to machine. The miniaturized receiver modules comprise chips that are produced en masse and which could conceivably be automatically assembled in future experiments. The IF, LO, and DC signals are largely routed on multilayer printed circuit boards which are innately easy to mass-produce.

2.5 The Radiometer

Argus is an state-of-the-art 16-pixel array that was designed to meet the specifications given in §2.4. This section will cover first the design concept (§2.5.1) and then the design of the RF (§2.5.2), LO (§2.5.3), IF (§2.5.4), and cryogenic (§2.5.5) subsystems.

2.5.1 Design Concept

Each of the *Argus* pixels is a heterodyne receiver. Figure 2.5 shows a circuit schematic for one pixel. A feedhorn (§2.5.2) couples incoming radiation to a miniaturized receiver module (§3), which contain most of the receiver functionality. The receiver modules amplify, filter, and downconvert the impinging RF signal. The downconversion is implemented with an I/Q scheme (§2.2.2), which folds the upper and lower frequency sidebands together. The miniaturized receiver modules attach to a cryogenic multilayer printed circuit board (§4.1) that routes the IF, LO, and DC signals to and from the receiver modules and also provides IF amplification and LO splitting. Flexible circuitry (§4.2) is used to transport high densities of IF and DC signals between temperature stages. The warm IF subsystem (§2.5.4) then separates the sidebands so that each channel being read out by the GBT backend (§2.5.4) corresponds to a unique RF frequency range before applying further signal conditioning.

The *Argus* array is comprised of four sub-units, or cards, that each include four pixels. An annotated CAD drawing for a four-pixel card is shown in Figure 2.6a. The four-pixel cards are designed to be stacked together to form a larger array. The *Argus* cards are arranged to form a 4x4 square-packed array by sliding the cards into a comb-like card cage as illustrated in Figures 2.6b and 2.7. In principle though, the four-pixel cards can be used as building blocks for an even larger array as discussed in §2.4.11.

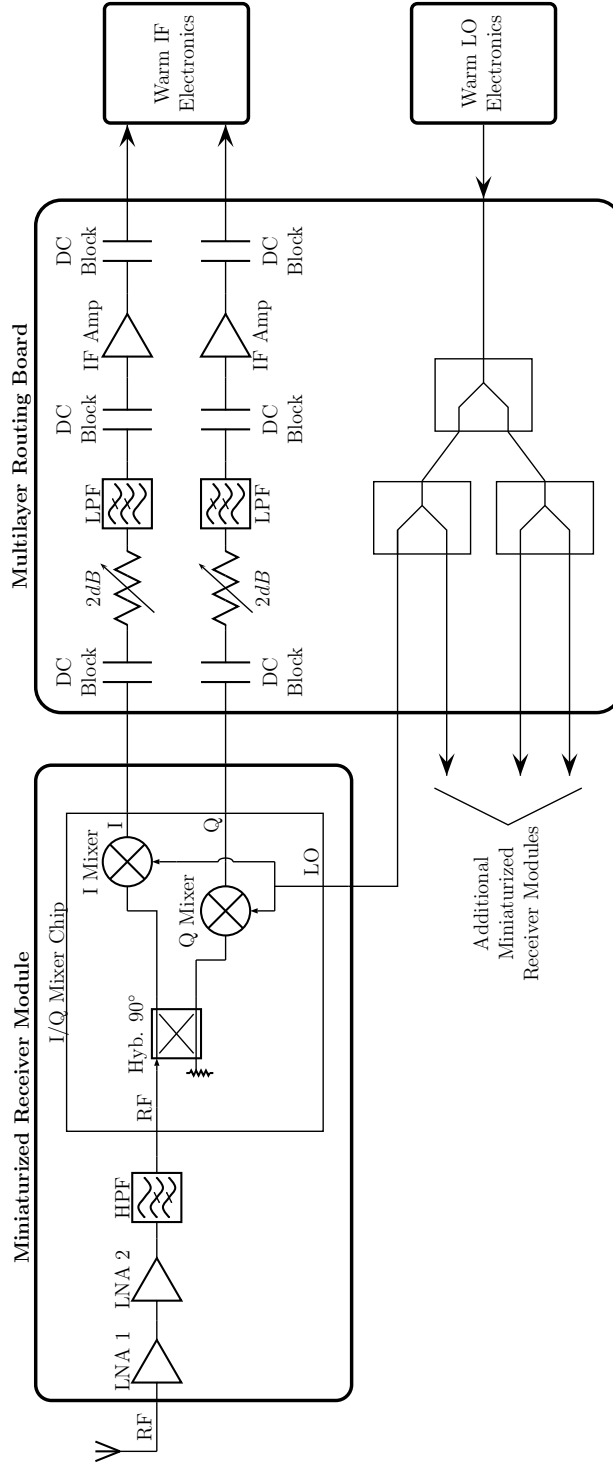
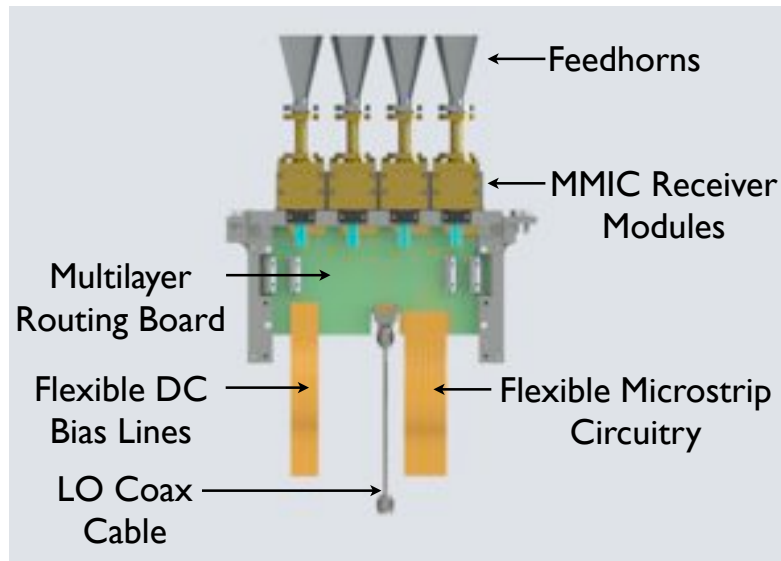


Figure 2.5: A schematic of the cryogenic front-end of the *Argus* receiver. The miniaturized receiver modules take millimeter-wave signals (76–116 GHz) at the RF port and amplify, filter, and down convert them to double-sideband IF outputs (0.90–2.15 GHz). The bandpass of the receiver modules is provided by the input waveguide, which has a sharp low frequency cut-off, and a high-pass filter (HPF). Further cryogenic amplification and band definition via a low-pass filter (LPF) is provided on the multilayer routing board. Each 4-pixel card receives a local oscillator signal, which is split four ways on the routing board. Detailed schematics for the warm IF and the LO systems are given in Figures 2.11 and 2.9, respectively.



(a) 4-Pixel Card



(b) Focal Plane Array

Figure 2.6: (a) An annotated CAD drawing of the production 4-pixel card. The production card has a 1.5 GHz instantaneous bandwidth to match the GBT backend. (b) A CAD drawing of the 4x4 *Argus* focal plane array. The array is built from 4-pixel subunits, or cards, which form the rows of the array. A card comprises the feedhorns, MMIC receiver modules, routing boards, flexible circuitry and cables.

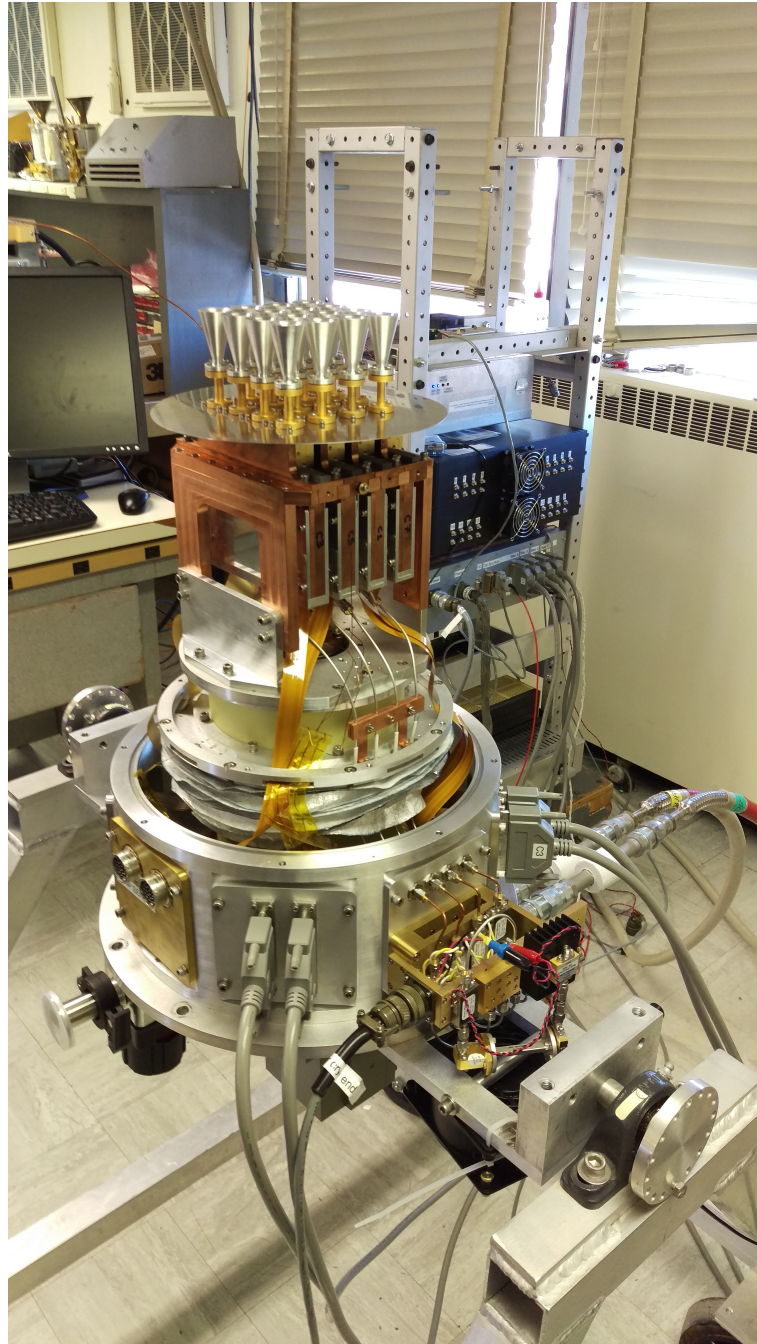


Figure 2.7: A photograph of the *Argus* focal plane.



Figure 2.8: The *Argus* window, which is made from 0.5" thick ultra-high-molecular-weight polyethylene.

2.5.2 RF System

Window

Argus requires a window with low insertion loss and high structural stability. The insertion loss has ohmic loss and a reflection contributions, both of which are undesirable. Ohmic losses before the heterodyne receiver can severely impact the system temperature of the array as dictated by Equation 2.8, while reflections can cause standing waves in the system. The window, designed by Josh Gundersen and pictured in Figure 2.8, is made from ultra-high-molecular-weight polyethylene (UHMW-PE), which is a hard plastic with a favorable loss tangent at microwave frequencies. The strength of the material minimizes bowing of the window when the cryostat is under pressure. The window is 8.0" in diameter and 0.5" thick with an anti-reflection layer on both sides that is formed through a uniform pattern holes with a quarter-wavelength depth.

Feeds

Smooth-walled feedhorns have been developed for *Argus* that can be economically mass-produced. Feedhorns were chosen in order to achieve the best possible bandwidth and pixel-to-pixel isolation. The feedhorn was designed by Patricia Voll and is a modified version of the design presented in [6]. The feedhorn profile is a spline with monotonically increasing diameter so that it can be easily machined with either a CNC milling machine or drilled with a mandrel. The beam pattern of these feedhorns is comparable to that of corrugated horns in terms of symmetry and sidelobe level, despite being lighter and easier to manufacture. The sidelobe level is more than 20 dB below the on-axis response over the entire *Argus* band. The feedhorn specifications were determined with the aid of optical simulations that I performed and are presented in detail in §B.

2.5.3 LO System

The LO system is required to provide sufficient power to each of the 16 *Argus* pixels with minimal broadband noise. The minimum acceptable LO power level at the miniaturized receiver modules is -5 dBm. Power levels below this level lead to an increased mixer conversion loss, which can degrade the system noise temperature via Equation 2.8. Additionally, the IF power is more sensitive to fluctuations of the LO power at lower LO power levels. For both of these reasons it is desirable to maximize the LO power impinging on the miniaturized receiver modules; however, it is difficult in practice for *Argus* to deliver large amounts of LO power for two reasons. Firstly, a single synthesizer must supply the LO to all 16 pixels, which requires splitting the LO signal into many smaller signals. Secondly, the coaxial cables and microstrip lines that *Argus* uses have a significant amount of loss even after steps were taken to mitigate the losses. Achieving sufficient LO levels required the incorporation of several power amplifiers, which have the undesirable effect of adding broadband noise. The consequences of having too much broadband LO noise are covered in detail in §5.4.3. A tracking YIG filter was added to the system to keep the LO noise levels at acceptable levels.

A schematic of the LO system is shown in Figure 2.9. There are two frequency doublers in the LO chain, which are required since the synthesizer has a maximum frequency of 20 GHz. The tracking YIG filter was placed between the two frequency doublers because its operational bandwidth is 20–40 GHz. The LO signal for each pixel passes through four power amplifiers which are needed to achieve the >-5 dBm specification at the miniaturized receiver modules. A custom 4-way Wilkinson splitter at room temperature creates a separate LO signal for each of the 4-pixel cards. A piece of waveguide after the second frequency doubler serves as a high pass filter that rejects the residual fundamental tone from the frequency doublers. The LO power that impinges on the miniaturized receiver modules is shown for a typical four-pixel card in Figure 2.10.

2.5.4 IF System

The IF system conditions the output signals and ultimately transports them to the GBT backend electronics. The multilayer routing boards provide the initial stages of amplification and filtering, while transporting the signals out of the cryostat. The details of the cryogenic signal processing are given in §4. There are two different IF signal chains that are employed outside of the cryostat: pixels 1–8 are routed on *Argus*-dedicated optical links and pixels 9–16 are routed to the standard GBT IF rack. The warm IF electronics, discussed in §2.5.4, condition pixels 1–8 for a set of optical transmitters while preparing pixels 9–16 for the GBT IF converter modules. Ultimately, all 16 pixels are routed to the backend GBT electronics which are covered in §2.5.4.

Warm IF Boards

The warm IF electronics provide amplification, filtering, sideband separation and equalization for the *Argus* output signals. A schematic of the warm IF electronics, which was designed and fabricated by Rohit Gawande at Caltech, is shown in Figure 2.11. A quadrature hybrid provides sideband separation as described in §5.1.7. It is followed by a switch that allows the user to switch between the upper and lower

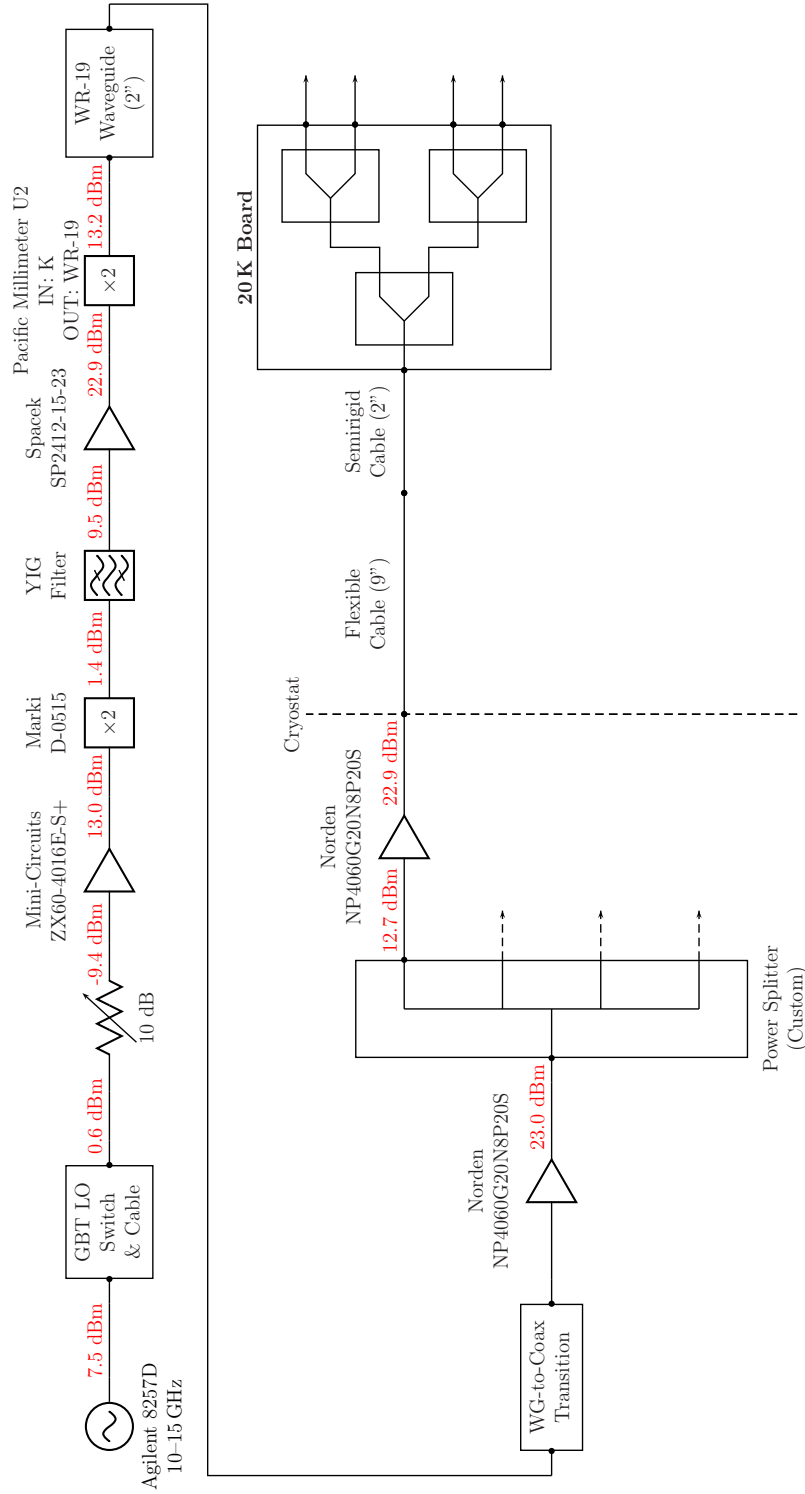


Figure 2.9: A schematic of the LO system. The LO system multiplies, amplifies, filters and splits the LO. The waveguide acts as a high pass filter to reject the fundamental tone from passing. The power values in red are the expected power levels at various points in the LO chain at a synthesizer frequency of 13.875 GHz (*i.e.* an effective LO of 111.0 GHz).

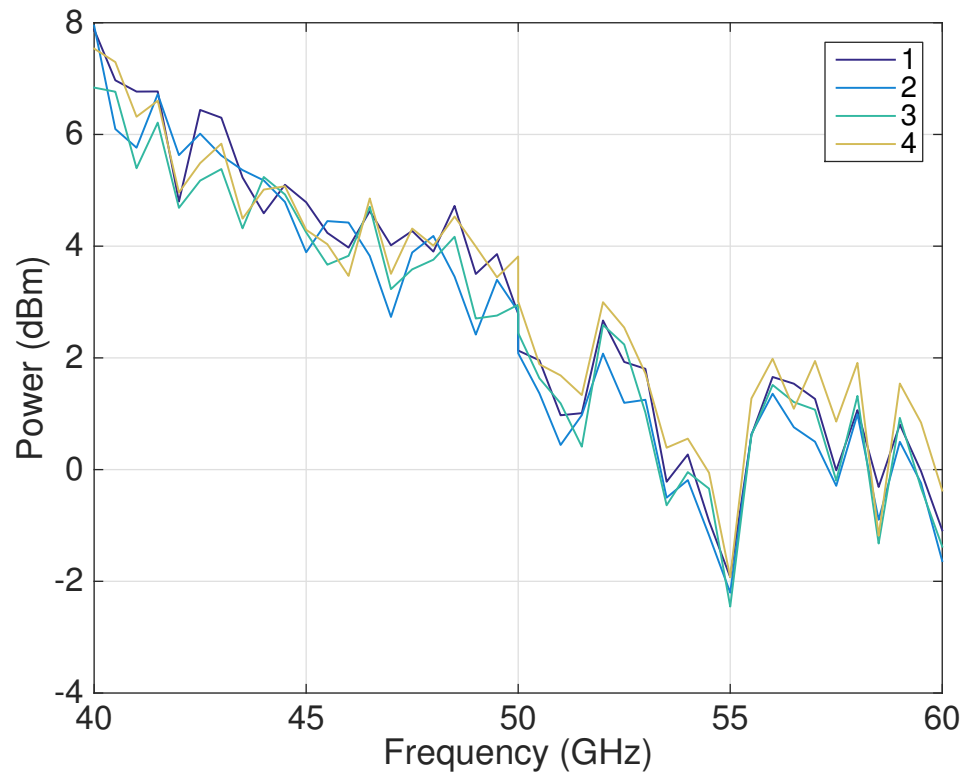


Figure 2.10: A plot of the output LO power from one of the 4-pixel cards as a function of LO frequency. The LO power decreases with LO power level because of ohmic losses in the system; however, the LO power is above the specification of -5 dBm across the entire LO frequency range for *Argus*.

sidebands. There are several stages of amplification and filtering which are followed by an equalizer. The fixed value attenuators were originally intended primarily for reducing standing waves between the amplification stages, which would adversely affect the instrument passband; however, these attenuators also had to be used to prevent saturation of the third and fourth amplifiers in each channel. The attenuations were chosen so that for pixels 1–8 a is 6 or 10 and b is 1–3 and for pixels 9–16 a is 5 and b is 10 as shown in Figure 2.11. A measurement of the linearity after settling on these attenuator values is described in §5.1.3. The output power level can be adjusted with the variable attenuator; the attenuation adjustment is both frequency and pixel dependent.

VEGAS Backend

The VErsatile GBT Astronomical Spectrometer (VEGAS) was installed in 2011 as an updated backend for the GBT [35, 36]. There are 16 inputs that are each capable of processing 1.25 GHz of bandwidth. The *Argus* IF band of 0.9–2.15 GHz was chosen to match the VEGAS bandwidth. VEGAS is built with the FPGA-based CASPER ROACH boards³. Each input has an 8-bit ADC that digitizes the signal before the FPGAs do the signal processing. There are many possible configurations for VEGAS, but for *Argus* the most common configuration will be to use a single spectral window of 1.25 GHz bandwidth. In this configuration the minimum possible resolution is 92 kHz and the minimum possible integration time is 1 ms. It is also possible to create 8 digital subbands per input with bandwidth 1–30 MHz.

2.5.5 Cryogenics

The *Argus* instrument is cooled with a two-stage, closed-cycle helium refrigerator that is based on the Gifford-McMahon thermodynamic cycle⁴. The operating temperature is ~ 70 K and ~ 25 K for the first and second temperature stages, respectively. Most of the focal plane array is thermally connected to the second stage. The cables and

³<http://casper.berkeley.edu/wiki/ROACH>

⁴CTI 1020

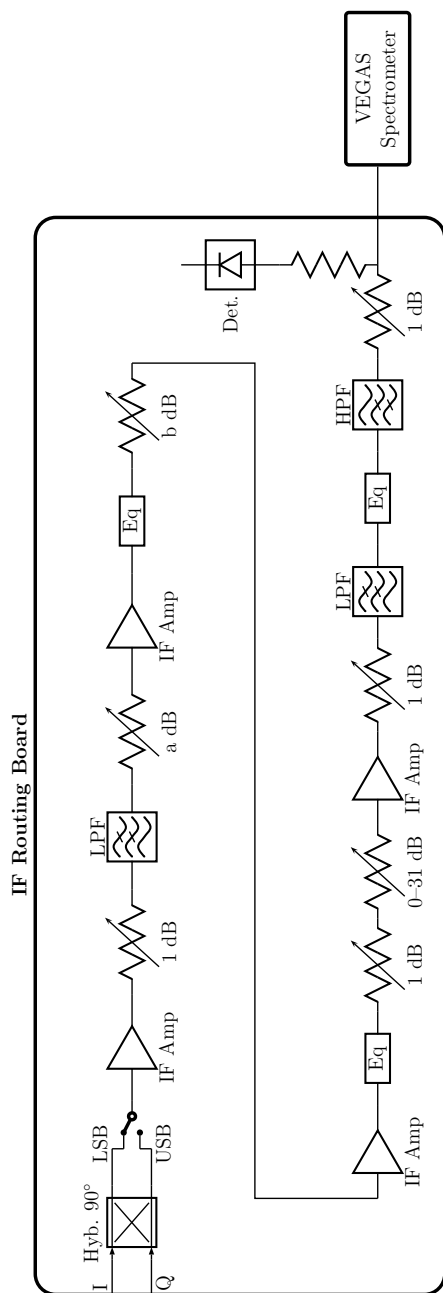


Figure 2.11: A schematic of the room temperature IF board. A quadrature hybrid separates the IF into its upper and lower sideband components. A switch allows the user to choose which sideband to observe. The following amplifiers, attenuators, and equalizers ensure compliance with the power and slope specifications for the VEGAS spectrometer. For pixels 1–8, a is 6 or 10 and b is 1–3. For pixels 9–16, a is 5 and b is 10.

Part	Loading (mW)				
	RF	DC	Conductive	Radiative	Total
LNAs	–	512	–	–	512
Mixers	–	24	–	–	24
Cold IF Amplifier	–	1,728	–	–	1,728
Flexible Coax Cables	49	–	5	–	54
Semirigid Coax Cables	56	–	94	–	150
Microstrip	127	–	–	–	127
IF Flexible Circuitry	–	–	1,368	–	1,368
DC Bias Lines	–	5	214	–	219
Radiation	–	–	–	1,500	1,500
System	232	2,269	1,681	1,500	5,683

(a) Loading on the second stage of the CTI 1020 ($T_2 \sim 25$ K).

Part	Loading (mW)				
	RF	DC	Conductive	Radiative	Total
Flexible Coax Cables	65	–	7,988	–	8,053
IF Flexible Circuitry	–	–	1,085	–	1,085
DC Bias Lines	–	7	170	–	177
Radiation	–	–	–	10,100	10,100
System	65	7	9,243	10,100	19,415

(b) Loading on the first stage of the CTI 1020 ($T_1 \sim 70$ K).Figure 2.12: A table of the heat loads on the *Argus* CTI 1020 cryostat for (a) the second stage at ~ 25 K and (b) the first stage at ~ 70 K.

flexible circuitry, which have a temperature gradient, are also attached to the first stage, which is capable of lifting more heat. The total cooling budget for *Argus* is shown in Table 2.12.

The cryostat design is illustrated in Figure 2.13. The cryostat has an octagonal base with connector flanges on each of the eight sides. The base was designed to be short relative to the height of the entire cryostat so that the *Argus* focal plane would be easily accessible when the top cylinders were removed. A 70 K shield fits over the array to block room temperature radiation from loading the second temperature stage. A room temperature outer cylinder is installed around the 70 K shield and the window is attached to a top plate.



Figure 2.13: A CAD drawing of the *Argus* cryostat. The connector feedthroughs are installed on the octagonal base. The cylindrical outer shell and the 70 K heat shield can be removed for full access to the focal plane array. The circular plate at the top of the drawing that holds the window was used for lab testing and was later replaced by a larger plate that adapts to the 24" diameter holes in the GBT turret.

2.5.6 Comparison with Similar Instruments

Argus distinguishes itself from previous 3 mm focal plane arrays by having lower system temperatures and a higher level of integration. The SEQUOIA array is a millimeter-wave imager with 16 dual-polarization pixels [37]. It is also a MMIC heterodyne array, but each of the MMIC components is housed in a separate package making the array less integrated and physically larger. The quoted receiver temperature for SEQUOIA was 50–80 K over the 85–116 GHz band, which was the previous state-of-the-art. This compares to the *Argus* receiver temperature of 39–65 K as presented in §5.1.1. Even earlier than this was the 15-pixel QUARRY focal plane array [38], which utilized cryogenic Schottky diode mixers as the front-end components. The receiver temperature was 250–350 K. Other fully integrated W-band heterodyne receiver modules have been presented in the literature [39, 40, 41, 42], but cryogenic noise data were not reported.

2.6 *Argus* Prototypes

Two prototype designs for the *Argus* array were constructed, pictured in Figure 2.14; they each informed the final production design. The first prototype, which will be called Prototype 1, was not built into an array, but instead the various parts of the cryogenic array were prototyped separately. A miniaturized receiver module was designed for the 82–100 GHz band, while the cryogenic routing components were designed for operation up to 20 GHz. The Prototype 1 receiver was originally envisioned as a proof-of-concept for a large-scale Cosmic Microwave Background interferometer as presented in [43]; however, the technological requirements for the *Argus* millimeter-wave spectroscopic imager were very similar to the original project goals: namely large bandwidth, ultra-low noise, and the ability to scale the array to many pixels. The second prototype, referred to in the following as Prototype 2, was a 4-pixel cryogenic array that was explicitly intended for *Argus*. This prototype extended the receiver RF bandwidth to 84–116 GHz by using an I/Q downconversion. Both of the prototypes built upon previous work in [44]. More information on the

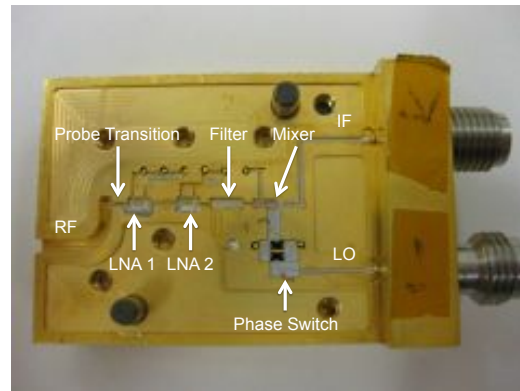
prototype designs are given in [45].

There were a number of significant changes between the design iterations, which are summarized in Table 2.3. The prototypes both used a fixed LO frequency and a very wide IF bandwidth, while the production modules used a tunable LO frequency and a 1.25 GHz IF bandwidth to match the backend capabilities of the GBT. The very wide instantaneous bandwidths that were demonstrated in the prototypes could eventually be leveraged in a future *Argus* upgrade. The downconversion scheme was another significant change between the two prototypes. The first prototype used a single sideband downconversion while the second prototype and the production *Argus* array use a double sideband I/Q scheme. Finally, the cryogenic signal routing systems are very different between the different designs due to the different IF and LO frequencies for which they were designed. The major differences between the different cryogenic signal routing designs are discussed in §4.1.

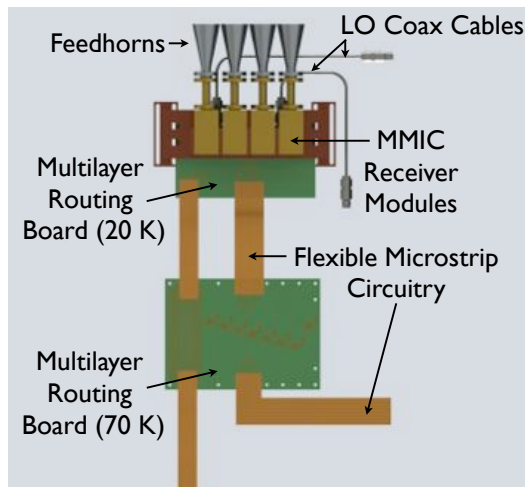
Table 2.3: Key differences between the first prototype, second prototype, and production version of *Argus*. There were significant changes in the frequency ranges, the downconversion scheme (§2.2.2, §3.2.2), and the cryogenic routing components (§4).

	Prototype 1	Prototype 2	Production & Pre-production
RF Frequencies	82–100 GHz	84–99 GHz & 101–116 GHz	76–116 GHz
LO Frequencies	40 GHz	50 GHz	39–57 GHz
IF Frequencies	2–20 GHz	1–16 GHz	0.9–2.15 GHz
Mixer	Single Sideband	I/Q (Double Sideband) Multiple Substrates	I/Q (Double Sideband) One Substrate
Multilayer Routing Boards	2 Boards Rogers RO4350B	2 Boards Rogers RO4350B	1 Board Taconic RF-35TC

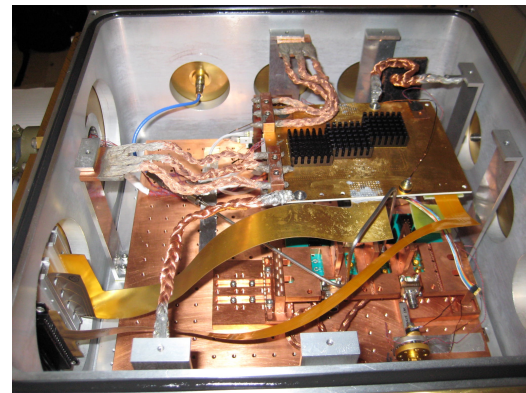
The evolution of the downconversion scheme between the different design iterations reflects the changing emphases in the design goals. In the Prototype 1 receiver, the emphasis was to keep the design as simple as possible; a single-sideband downconversion with a fixed LO frequency was implemented. The single-sideband downconversion is more straightforward than an I/Q double-sideband downconversion because it has



(a) Prototype 1 Receiver Module



(b) Prototype 2 Design



(c) Prototype 2 Photograph

Figure 2.14: (a) A photograph of the MMIC receiver module for *Argus* Prototype 1. (b) An annotated CAD drawing of the 4-pixel card for *Argus* Prototype 2, which was designed for wide instantaneous bandwidths. The IF amplifier used in the prototype card dissipates too much power to be placed on the 20 K stage and was therefore incorporated onto a second multilayer routing board on the 70 K stage. (c) A photograph of the assembled 4-pixel card for *Argus* Prototype 2.

just one IF output and does not require additional circuitry for sideband separation. The fixed LO frequency simplifies the design of the LO subsystem because it does not require broadband components. One of primary goals of the Prototype 2 design was to maximize the available RF bandwidth⁵. This was accomplished by moving to a double-sideband I/Q downconversion (§2.2.2). It was assumed in this design that a second frequency shift would need to be implemented in order to couple the IF to the GBT backend electronics, which have a fixed bandwidth of 1.25 GHz (§2.5.4). Specifically, a selected 1.25 GHz chunk of the 1–16 GHz IF signal would first be upconverted to a frequency above 16 GHz and then downconverted to a lower frequency suitable for readout by the GBT IF system. Finally, in the Pre-production and Production designs, it was decided that a second frequency shift was too difficult to implement; many of the components were required to have wide bandwidths and two additional synthesizers were needed. Therefore, the final designs utilized a tunable LO signal with a fixed IF frequency range of 0.9–2.15 GHz. The advantages of this approach compared to the prototype designs are that:

- The IF signal conditioning prior to the GBT IF system is straightforward since the frequencies do not require shifting.
- It is significantly easier to identify suitable cryogenic IF amplifiers with narrower bandwidths. There are relatively few commercially available low-noise surface-mount amplifiers in bandwidths extending to 16 GHz. Moreover, the bias power for amplifiers in general increases with bandwidth. Therefore, the wideband IF amplifiers required in this prototype designs needed to be installed on printed circuit boards that were thermally connected to the first stage of the cryostat ($\sim 70\text{K}$) with its higher cooling power (§4.1.2). The Pre-production and Production designs were able to forgo the first stage printed circuit board entirely, which simplified the design.
- The transmission line loss is small over the 0.9–2.15 GHz IF frequency range of the Pre-production and Production designs, which means that minimal equalization is necessary before sending the IF signal to the GBT IF system. By contrast,

⁵The other major goal was to reduce the receiver noise temperature over this bandwidth

the IF losses in the prototypes are significant. The loss is roughly linear with frequency out to 16 GHz and this leads to a significant slope in the IF passband.

- The tunable RF frequency coverage extends from 76–116 GHz with no gaps. The Prototype 2 design on the other hand had a gap in coverage centered around 100 GHz⁶.

The downsides to the Pre-production and Production designs are primarily related to the LO system. Namely:

- There were significant connector mismatches in the final LO system (§2.5.3). Improving this impedance match is straightforward at a fixed frequency, but challenging over a wide bandwidth.
- The selection of viable commercial components for the LO system is minimal for wide bandwidths. Moreover, the operational bandwidths of the wideband commercial components that do exist are typically restricted to the standardized telecommunications bands.

⁶This gap could in principle be minimized by improving the performance of the mixer at low frequencies; however, frequencies near DC are more susceptible to $1/f$ noise and so in practice there would still need to be a finite gap.

Chapter 3

Miniaturized Receiver Modules

The core technology for the *Argus* receiver are low-noise miniaturized receiver modules that are each a complete heterodyne receiver. Multiple components are integrated into a single compact module including a waveguide-to-coplanar waveguide probe transition, two low-noise amplifiers (LNAs), a filter, an equalizer, and an I/Q mixer as shown in Figures 3.1, 3.2, and 3.4. The low-noise amplifiers, which were designed by the NASA Jet Propulsion Laboratory and fabricated at Northrop Grumman Corporation, enable the *Argus* pixels to achieve state-of-the-art receiver temperatures. All of the receiver components are innately mass-producible, while the packaging was designed so that the receivers could in principle be automatically assembled. The small size of the miniaturized receiver modules and their mass-producibility make them well-suited to large-format arrays.

Four iterations of the miniaturized receiver modules are presented. They will be referred to as the *Argus* Prototype 1, Prototype 2, Pre-production, and Production designs as in §2.6. Lower receiver temperatures and wider bandwidths were achieved as the design iterations progressed (§3.4). The Prototype 1 receiver module had a 27–58 K noise temperature over the 82–100 GHz band [45], the Prototype 2 receiver module had a 27–45 K over the 75–111 GHz band [4], the *Argus* Pre-production receiver modules exhibited a noise temperature of 27–45 K over the 76–116 GHz frequency band [46], and the average Production receiver module has 27–52 K noise temperature over the 76–116 GHz band. Photographs of the four miniaturized receiver module

are shown in Figures 2.14 and 3.4. The workload for designing and testing these four versions of the miniaturized receiver modules was split between Stanford, Caltech, and the NASA Jet Propulsion Laboratory. The Production *Argus* multi-chip receiver module was designed and tested at Caltech. I personally worked extensively on the design and testing of Prototype 1. My involvement with the subsequent versions of the receiver modules was mostly in characterizing and troubleshooting at the system level.

This chapter is organized as follows. The amplifier technology is presented in §3.1. The receiver components, which we will call the chipset, are described in §3.2. The packaging scheme is covered in §3.3. Finally, the performance of the miniaturized receiver modules is detailed in §3.4.

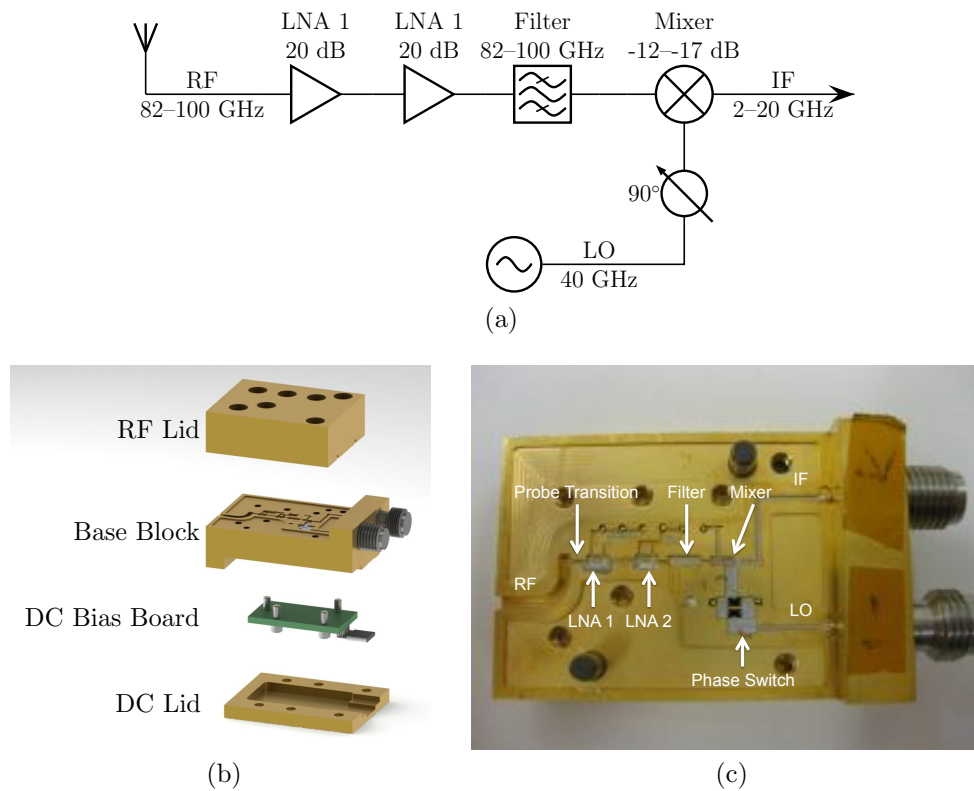
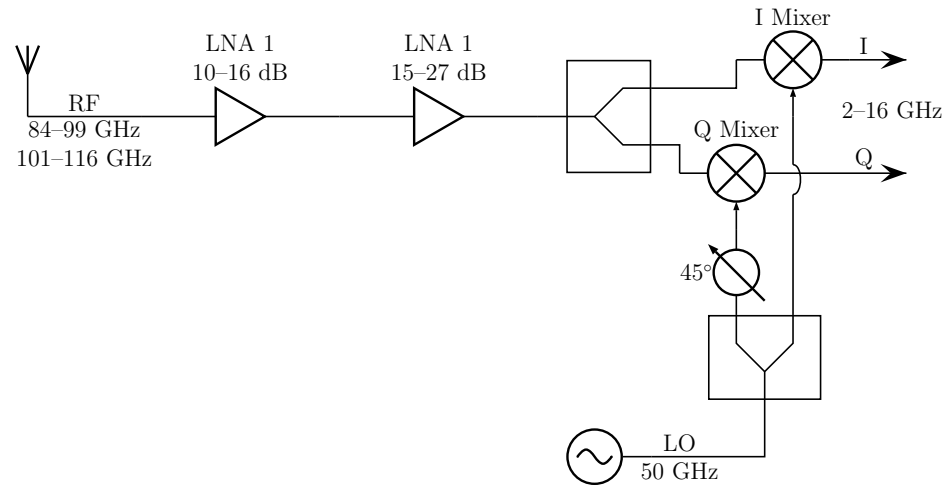
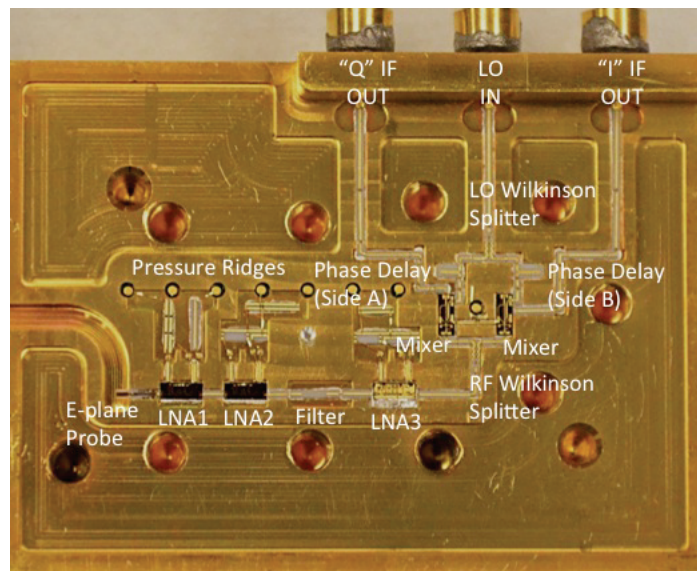


Figure 3.1: The *Argus* Prototype 1 miniaturized receiver module. (a) A schematic of the receiver module showing the gains and bandwidths of some of the key components. (b) A CAD drawing of the split-block receiver design. The components are mounted in cavities in the base block, while the RF lid provides a hermetic seal. (c) A photograph of the assembled receiver module before the lid was closed.



(a)



(b)

Figure 3.2: The *Argus* Prototype 2 miniaturized receiver module RF design. (a) A schematic of the receiver module showing the gains and bandwidths of some of the key components. The total receiver gain is approximately 15–27 dB. (b) A photograph of the assembled receiver module before the RF lid was closed.

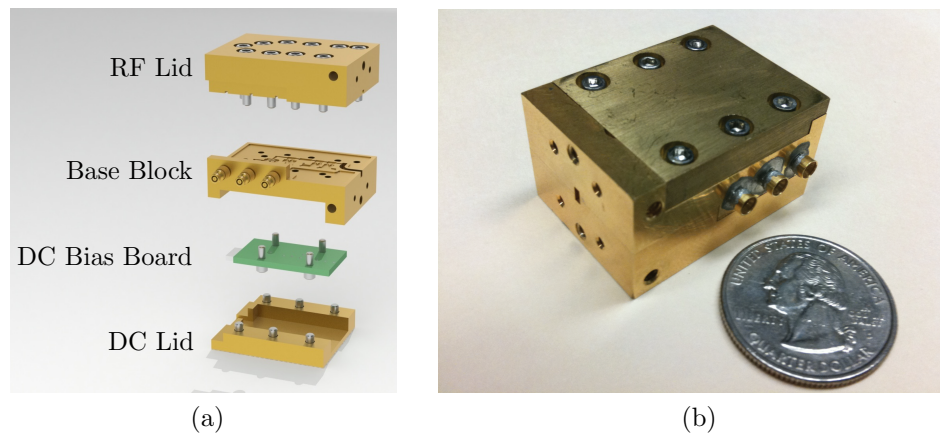
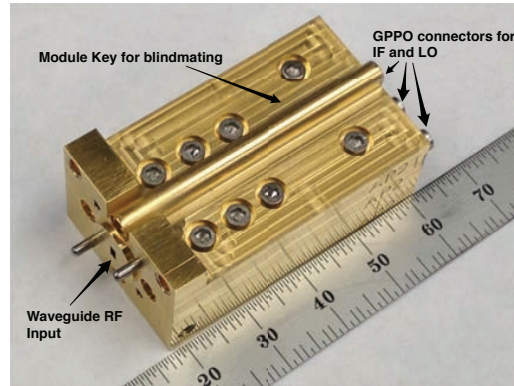
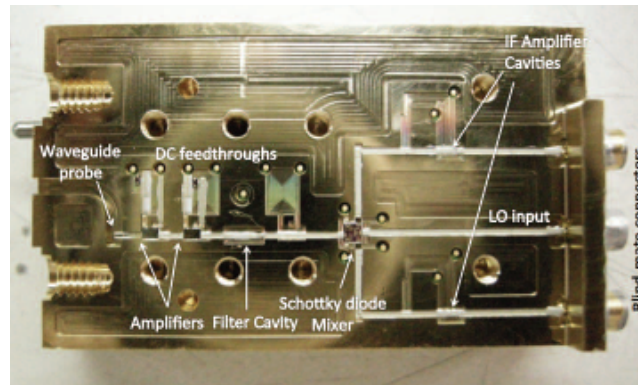


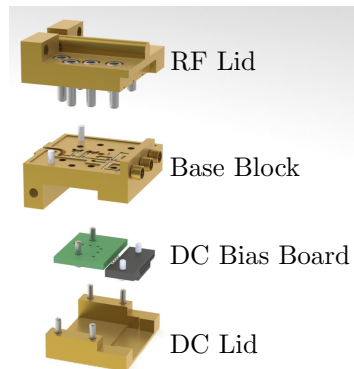
Figure 3.3: The *Argus* Prototype 2 miniaturized receiver module packaging. (a) A CAD drawing of the split-block receiver design. The components are mounted in cavities in the base block, while the RF lid provides a hermetic seal. The IF and LO connectors are miniaturized push-on connectors that launch from the side of the receiver module. (b) A photograph of the outside of the miniaturized receiver module after assembly.



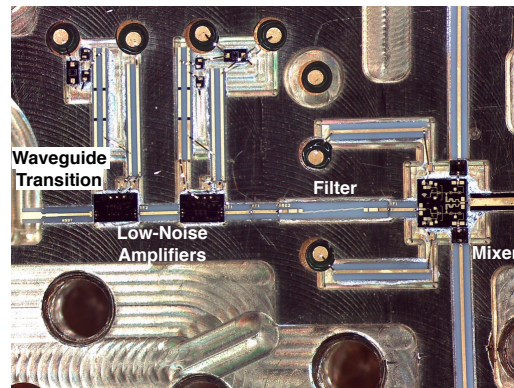
(a) Pre-production – Outside



(b) Pre-production – Inside



(c) Production – CAD



(d) Production – Inside

Figure 3.4: Photographs of the Pre-production and Production *Argus* miniaturized receiver modules. Both of these designs have a keying mechanism along the length of the receiver module that facilitates blind mating into the focal plane array.

3.1 Technology

3.1.1 Monolithic Microwave Integrated Circuits (MMICs)

Large-format heterodyne arrays require low-noise amplifiers and mixers that are mass-producible and easily packaged into small form factors, which can be achieved with Monolithic Microwave Integrated Circuits (MMICs). MMICs are microwave circuits where all of the circuit components are fabricated together on a single chip. For many applications MMIC technology has begun to replace Microwave Integrated Circuit (MIC) or hybrid technology where individual devices like transistors and passive components are bonded to a substrate and then interconnected. Both of these technologies have their advantages [47]. The advantages of using MIC technology are:

- MIC technology is relatively affordable in small quantities.
- The design process is faster for MIC technology since it is straightforward to iterate designs. Post-production tuning can easily be accomplished by modifying or adding passive components. MMIC technology, on the other hand, requires another wafer run for each iteration.
- Traditionally, MIC devices have exhibited lower noise because they use substrates with very small dielectric loss; however, MMIC technology has caught up through recent developments with cryogenically-cooled devices (see *e.g.* [48, 49, 50, 51, 52]).
- MIC devices are able to use passive components with higher quality factors.
- The device yield with MIC technology is high since malfunctioning parts can be omitted or replaced. On the contrary, the high level of integration in MMIC parts means that a failure in any component in the circuit causes the entire device to be compromised. Relatively low yield is still an area in need of improvement in cryogenically-cooled MMICs.

In contrast, the pros of using MMIC technology include:

- MMIC technology becomes cheap at large quantities due to economies of scale.

- MMICs are innately mass-producible. MIC amplifiers have a much more arduous assembly process. This is of little concern for small numbers of devices, but it makes mass-production challenging.
- In general more repeatable performance can be achieved with MMIC technology from device to device because the entire fabrication process is automated.
- MMIC devices have lower parasitic reactances, which enable designs with larger bandwidth.
- MMIC parts are smaller and easier to package than their MIC counterparts. This makes MMIC technology more attractive for large-format arrays.

While MIC parts do have a number of design advantages, MMIC parts are vastly superior when it comes to mass-production and ease of packaging (§3.3). *Argus* utilizes MMIC low-noise amplifiers and mixers in an effort to realize a design that is scalable to larger formats.

3.1.2 High-electron-mobility transistors (HEMTs)

A millimeter-wave heterodyne imaging array like *Argus* requires a front-end with ultra-low noise and high gain (§2.3) and oftentimes a wide bandwidth; a common way to achieve this is to use amplifiers that are based on high-electron-mobility transistors (HEMTs). HEMTs are a type of field-effect transistor (FET) that is formed via a junction between semiconductors with different bandgaps (*i.e.* a heterostructure). In general the heterojunction is formed between a thin n-type layer and an undoped layer¹ The discontinuity between the two conduction bands is arranged so as to make a narrow triangular-shaped potential well on the undoped side of the heterojunction as illustrated in Figure 3.5. Some of the free electrons from the n-type layer become confined in the thin layer that corresponds to the potential well; this is known as a two-dimensional electron gas (abbreviated 2DEG). The 2DEG electrons have very high mobilities (*i.e.* the channel has very low resistivity) because their path of travel

¹For the *Argus* amplifiers the n-type layer is InAlAs and the undoped channel layer is InAs as is depicted in Figure 3.5.

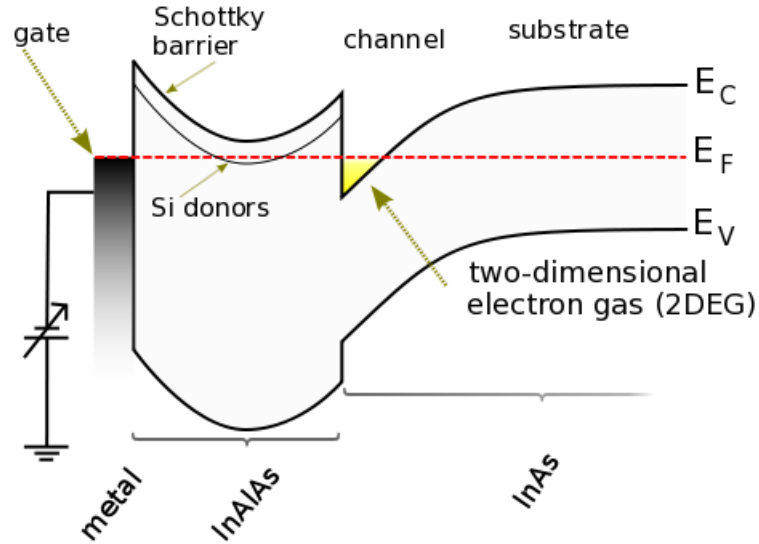


Figure 3.5: The band diagram for the heterojunction between an n-type InAlAs layer and an undoped InGaAs layer. The image is adapted from https://en.wikipedia.org/wiki/High-electron-mobility_transistor#/media/File:HEMT-band_structure_scheme-en.svg.

is through the undoped layer, which does not have impurities. The high electron mobilities can be leveraged for high gain and low noise at millimeter-wave frequencies and beyond.

The noise properties of HEMTs are described by a model proposed by Pospieszalski [2] that uses an equivalent circuit for a FET as shown in Figure 3.6a. The noise from the FET is modeled via thermal noise (*i.e.* Johnson-Nyquist noise) from the resistors. The noise contributions from the parasitic resistances at each terminal (r_d , r_g , and r_s) are governed by the physical temperature of the chip (T_a). The intrinsic noise of the FET (*i.e.* the noise measured after de-embedding the parasitic resistances) can then be described by two frequency-independent parameters: the effective temperatures of the gate (T_g) and the drain (T_d). The noise-equivalent circuit for the intrinsic FET is shown in Figure 3.6b. The noise contributions from the gate and drain are

$$\overline{e_{gs}^2} = 4kT_g r_{gs} \Delta f \quad (3.1)$$

and

$$\overline{i_{ds}^2} = 4kT_d g_{ds} \Delta f \quad (3.2)$$

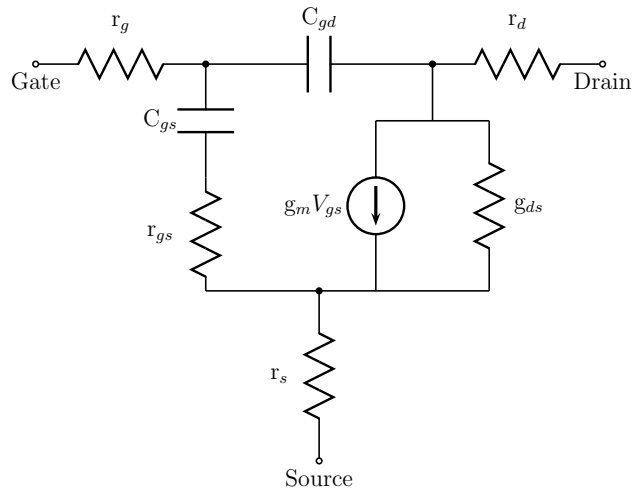
where k is the Boltzmann constant, T_g is the effective temperature of the gate, T_d is the effective temperature of the drain, r_{gs} is the gate-to-source resistance, g_{ds} is the drain-to-source resistance and Δf is the device bandwidth. The effective gate and drain temperatures have been observed to follow some empirical relations [53]. The effective gate temperature is roughly equal to the ambient temperature of the device, with a slight dependence on the drain current. Meanwhile, the effective drain temperature is proportional to the drain current and independent of the device temperature.

The Pospieszalski model gives a clear answer for how to minimize the noise of a FET. The minimum noise temperature of a FET (T_{min}), as predicted by the model, decreases with decreasing resistive values and increasing transistor speeds²:

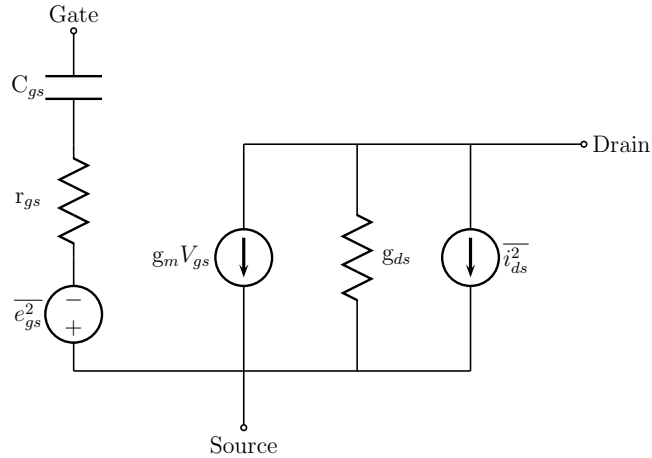
$$T_{min} \approx 2 \frac{f}{f_T} \sqrt{r_t T_d g_{ds} T_g} \quad (3.3)$$

where $r_t = r_s + r_g + r_{gs}$, f is the operating frequency, and the transistor speed is quantified by the transition frequency, f_T , which is a common figure of merit for transistors. Firstly, a significant improvement can be gained by cooling the device since T_g improves with temperature. In practice, cryogenic InP HEMTs are typically cooled to around 20 K, which in general improves the noise temperature by a factor of 7–10 [50]; below 20 K there are diminishing returns. Secondly, reducing the parasitic resistances can lead to significant improvements. For example, the gate resistance is oftentimes decreased by using a T-shaped gate that has a large surface contact area but maintains a small footprint at the n-type semiconducting layer and therefore a small gate length [49]. Thirdly, it is important to make sure that the drain current is as small as possible since T_d is affected linearly. A diagnosis for problematic drain currents is to pinch-off the FET and check for abnormally high drain currents. Finally, major improvements in device noise can be made by increasing the transition frequency,

²Equation 3.1.2 is valid only if $\frac{f}{f_T} \ll \sqrt{\frac{T_g}{T_d} \frac{1}{g_{ds} r_{gs}}}$.



(a) The equivalent circuit for a field-effect transistor.



(b) A noise-equivalent schematic for a field-effect transistor after de-embedding the parasitic resistances r_d , r_g and r_s .

Figure 3.6: The equivalent circuits of a field-effect transistor that are used in the Pospieszalski noise model [2].

f_T , which is given by

$$f_T = \frac{g_m}{2\pi C_{gs}} \quad (3.4)$$

Lower noise temperature components can be realized by increasing the transconductance, g_m , of the transistor or by decreasing the gate-to-source capacitance, C_{gs} . In practice, both of these approaches are being implemented to achieve state-of-the-art HEMT devices [54]. The transconductance can be improved by increasing the indium content of the channel layer. Meanwhile, the gate-to-source capacitance is improved by decreasing the gate length of the transistor.

3.2 Chip Set

The *Argus* miniaturized receiver modules integrate the following chips: a waveguide-to-microstrip transition [55], two low-noise amplifiers (§3.2.1), a filter, and a mixer (§3.2.2). The filters were added to define the bandpass and reject out of band power that could contribute to saturation of receiver components. In Prototype 1, the filter is also responsible for sideband separation. Prototypes 1 and 2 used the same 4-pole coupled line bandpass filters, which were implemented on 0.1 mm alumina substrate³. The insertion loss of the filter is approximately 1.5 dB and the 3 dB-bandwidth is 78–118 GHz. The Pre-production and Production designs used a high-pass filter and relied on the waveguide cutoff frequency for defining the lower edge of the bandpass.

3.2.1 Low-Noise Amplifiers

The low-noise amplifiers that are used in *Argus* have state-of-the-art noise temperatures and high gain over a large bandwidth, which is important for achieving low receiver temperatures (§2.3.3). Different amplifiers were utilized in the various design versions. All of the *Argus* low-noise amplifiers were built with either a 35 nm or 100 nm Indium Phosphide (InP) high electron mobility transistor (HEMT) process⁴ as indicated in

³The version of the Prototype 2 receiver module that is presented in this chapter had the filter replaced by a through line.

⁴The amplifiers were all designed by JPL collaborators and manufactured by the Northrop Grumman Corporation.

Table 3.1. The transition to 35 nm gate length devices is significant because these devices have higher transition frequencies, f_T , which can be leveraged to create devices with lower noise temperature⁵. The InP HEMT devices are known for their excellent cryogenic performance particularly at shorter gate lengths [49]. The Prototype 1 design used a four-stage 100 nm gate length device [56] and the Prototype 2 design utilized a two-stage 35 nm gate length device [50]. Meanwhile the amplifiers for the Pre-production design [51] and Production design [52] were both three-stage 35 nm gate length devices. A summary of the performance of the different amplifiers is given in Table 3.1. The Production devices were measured at the chip level with a cryogenic probe station [57], while the previous designs were characterized in a waveguide package. The cryogenic probe stations allow the low noise amplifier chips to be screened before being installed into miniaturized receiver modules. This ensures that the best amplifiers get chosen for the first amplification stage in the receivers.

The number of low-noise amplifiers changed between the different design iterations. In the Prototype 2 and Pre-production designs there was a concern that the low noise amplifiers would not have enough gain to overcome the noise contributions of all of the subsequent components because the gain of some of the low-noise amplifier candidates under consideration was relatively low. A third amplifier cavity was therefore incorporated into the design. In practice, the third amplifier was sometimes replaced by a through line when the gain of the first two amplifiers was sufficient. In the instances where there were three amplifiers present, the filter was placed between the second and third amplifiers to protect against saturation of the third amplifier. The Pre-production design additionally had the provision for IF amplifiers, but this functionality was never used because the cost of the amplifiers under consideration were prohibitively expensive.

3.2.2 Mixers

There were two different mixers that were utilized between the four *Argus* receiver module designs. The mixing scheme changed significantly between each design for

⁵See Equation 3.1.2 and the associated discussion.

Table 3.1: A summary of the low-noise amplifiers used in the *Argus* prototype and production designs and their performance over the 75–115 GHz frequency range.

Design	Technology	Noise Temp.	Gain	Ref.
Prototype 1	100 nm InP	30–60 K	>20 dB below 100 GHz	[56]
Prototype 2	35 nm InP	27–40 K	>15 dB below 103 GHz at room temperature	[50]
Pre-production	35 nm InP	24–42 K	28–30 dB below 110 GHz	[51]
Production	35 nm InP	23–50 K	22–27 dB	[52]

reasons that are well summarized in §2.6. Both mixers were implemented with antiparallel GaAs Schottky diode pairs⁶. They are both pumped with the second harmonic of the LO, which puts the required LO frequency at half that for a fundamental mixer. The advantage of such a subharmonic mixer is two-fold: it is possible to route the LO signal more efficiently because ohmic losses increase with frequency and higher frequency components are significantly more expensive because they are less commonly used in commercial applications and are more difficult to make.

The mixer for Prototypes 1 and 2, designed by Yu-Lung Tang and Sander Weinreb at Caltech, was not created for *Argus* but was used because of its availability. This mixer was intended for operation in the 70–90 GHz band⁷. The original characterization of this mixer was done with an LO frequency of 30–40 GHz with a 10 GHz IF frequency. I did a subsequent characterization where the RF range was modified to 75–115 GHz, the LO frequency was 40–50 GHz and the maximum IF frequency was 25 GHz. The results of this characterization are shown in Figure 3.7a. The data show that the mixer can be operated well outside its design bandwidth but at the expense of worse conversion loss. The conversion loss of the mixer when operated within its intended bandwidth is 12–15 dB, while for the extended bandwidth the conversion loss degrades to 12–25 dB. The performance at low IF frequencies degrades below 1 GHz, as illustrated in Figure 3.7b, because of a 1,188 fF capacitor on the IF path on the mixer chip. It should also be noted that the Prototype 1 and 2 receiver modules used this mixer in very different ways. In the Prototype 1 design, a bandpass filter

⁶They were built by United Monolithic Semiconductor (UMS).

⁷This mixer is called the “80MIX2”.

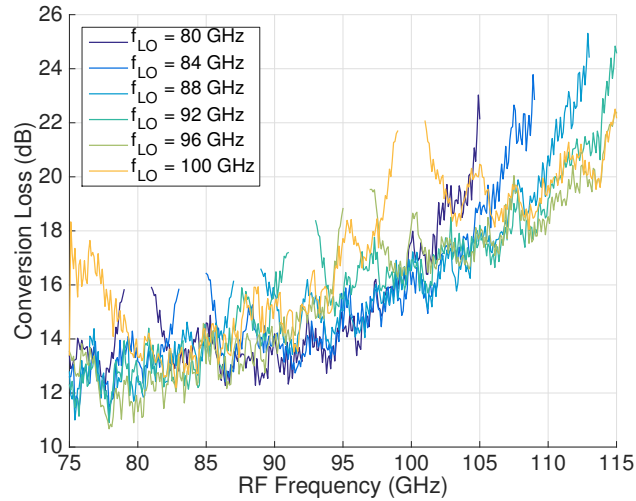
preceded a single mixer creating a single sideband receiver. In contrast, the Prototype 2 design used two mixers that were arranged to create an I/Q mixer. The mixers were driven with an LO that was 45° out of phase. The RF was split equally between the two mixers with a Wilkinson splitter.

For the Pre-production and Production *Argus* receiver modules a new mixer was designed by Rohit Gawande at Caltech [3]. This mixer utilized an I/Q downconversion scheme, but unlike in Prototype 2, the mixer was designed on a single substrate. In this mixer, which is schematically illustrated in Figure 2.3b, the RF input to the two mixers is driven 90° out of phase via a quadrature hybrid. In practice, the IF frequency that is used for this mixer is simply the *Argus* IF band of 0.90–2.125 GHz. The LO frequency in *Argus* is designed to be tunable over the 39–59 GHz band to allow access to the 76–116 GHz RF range. The conversion loss of this mixer at a fixed IF of 1 GHz is shown in Figure 3.8. The conversion loss ranges from 10–18 dB, which is sufficiently low to allow for a low receiver noise via Equation 2.8. It should be noted though that the mixer was characterized from an IF of 1–10 GHz so this design could in principle support a receiver with a larger instantaneous bandwidth. The conversion loss of the mixers is 12–18 dB across the *Argus* band at 10 dBm LO power, which is approximately the maximum LO power that impinges on the mixers at the lowest LO frequencies (Figure 2.10). The conversion loss degrades by only about 1 dB at an LO power of 0 dBm, which is roughly the LO power at the mixer at the highest LO frequencies.

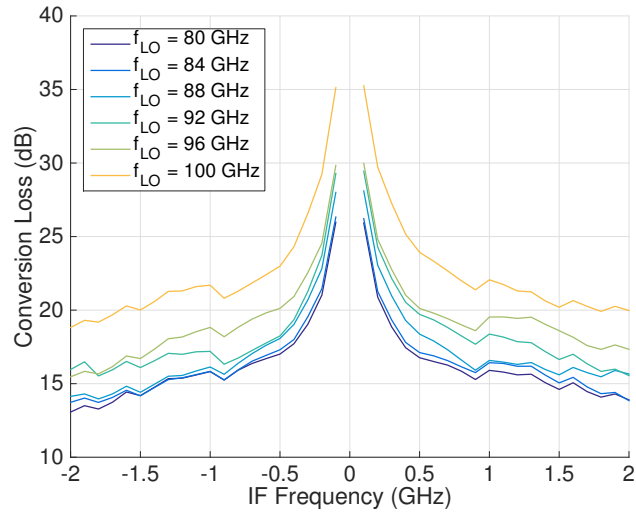
3.3 Packaging

The packaging design for the *Argus* receiver modules had to meet several criteria:

- Integrate all of the MMIC components into a single compact unit,
- maintain a low receiver temperature that is dominated by the first low-noise amplifier,
- be free of resonances that would affect the system stability,



(a) The conversion loss versus RF frequency where the IF is 1–25 GHz.



(b) The conversion loss at low IF frequencies (0.1–2.0 GHz).

Figure 3.7: The conversion loss for the mixer used in Prototypes 1 and 2. A range of LO frequencies from 40–50 GHz was used. (a) The performance as a function of the RF frequency. The IF frequency ranges from 1–25 GHz. Lower IF frequencies were measured, but a DC block capacitor causes the response to roll off significantly below 1 GHz. The conversion loss varies from 11–25 dB amongst the different LO configurations. A fixed 50 GHz LO frequency can be used to cover the entire 75–115 GHz frequency range with a conversion loss of 12–23 dB. (b) The conversion loss is plotted for only IF frequencies below 2 GHz in order to illustrate the degradation in performance due to the DC block capacitor on the mixer chip.

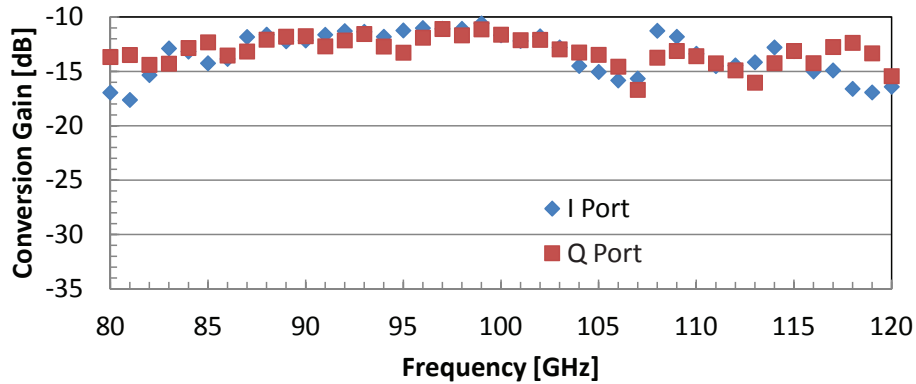


Figure 3.8: A plot of the conversion loss versus RF frequency for the mixer used in the Pre-production and Production receiver modules as reproduced from [3]. The IF frequency is fixed at 1 GHz. The conversion loss ranges from 10–18 GHz over the 80–120 GHz band.

- have low pixel-to-pixel cross talk,
- and is amenable to mass production.

The *Argus* receiver modules utilize a split-block package, illustrated in Figures 3.1b, 3.3a, and 3.4c, where the RF components are installed into cavities in a base block and a second block is attached as a lid. The RF lid provides a hermetic seal in conjunction with pressure ridges along the RF path in the base block, which provides RF isolation between components and between different pixels. When joined, the base block and RF lid form a WR-10 waveguide input at their interface. The blocks are all gold-plated brass, which minimizes the ohmic loss from the waveguide that would otherwise deteriorate the system temperature⁸. The RF components are mounted in 0.015” deep cavities in the base block using silver epoxy⁹. The transverse dimensions of the cavities were carefully chosen to avoid in-band resonances. The components are then interconnected with gold ribbon wire bond. The distances between components is kept small for several reasons: the parasitic inductance from the wirebonds is minimized, which improves the impedance match between components, the insertion

⁸via Equation 2.8

⁹EPO-TEK H20E

loss is minimized and the required size of the packaging is as small as possible. While the *Argus* receiver modules are hand-assembled, the split-block concept is conducive to automated assembly via pick-and-place machines and automatic wire bonding machines. This feature will become important for future *Argus*-like arrays that have significantly more pixels.

The external features of the *Argus* production receiver modules are designed to allow broken or poorly performing modules to be swapped without having to remove an entire card. It is required that the installation and removal of modules be done blindly since the pixels are closely packed. A blind mate was incorporated via two design decisions: a length-wise keying mechanism for precise placement of the receiver module during installation and the use of push-on connectors that do not require direct access to the connectors for installation or removal. The keying mechanism was machined with wire EDM and is shown in Figure 3.4.

The IF and LO are routed through a high-frequency push-on connector¹⁰. The connectors are rated up to 60 GHz, which is above the maximum LO frequency for *Argus* (Table 2.2). The concept of implementing the high-frequency push-on connectors was first implemented in Prototype 2 where the connectors launched from the side of the receiver modules. The connectors were moved to the side opposite the feedhorn in the Pre-production and Production designs for two reasons: the receiver modules could be more closely packed after the change and because the mating connectors on the multilayer routing connectors were found to be mechanically unreliable in Prototype 2. In Prototype 1, the connectors were instead K and V precision coaxial connectors¹¹, which were used because of their compatibility with standard test equipment. The DC connectors in the Production *Argus* design are 9-pin strip connectors¹² that are also amenable to blind mating.

The bias circuitry for the low noise amplifiers and mixers is located on the base block opposite on the opposite side of the RF components. A printed circuit board routes the bias voltages into the receiver and includes protection circuitry and resistive

¹⁰Corning Gilbert B007-M43-01-TAB-X Hermetic Shroud

¹¹Anritsu V102F-R & K102F-R

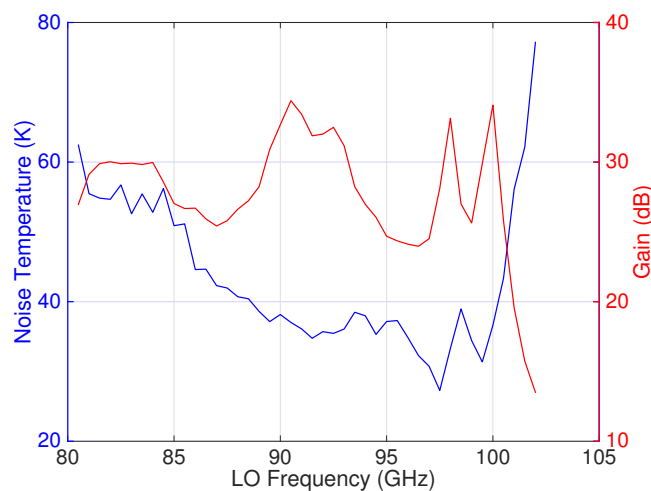
¹²Omnetics PSM-09-AA-M-GS-1-6 & Omnetics SSO-09-WD-18.0-C-M-GS-1-6

dividers. Hermetic DC feedthroughs¹³ pass the bias voltages from the DC side of the base block to the RF side. A second lid is provided for the DC side of the base block. This lid is less important because it does not provide the hermetic seal. Instead, its purpose is primarily to prevent unintentional shorts or damage to any of the bias components.

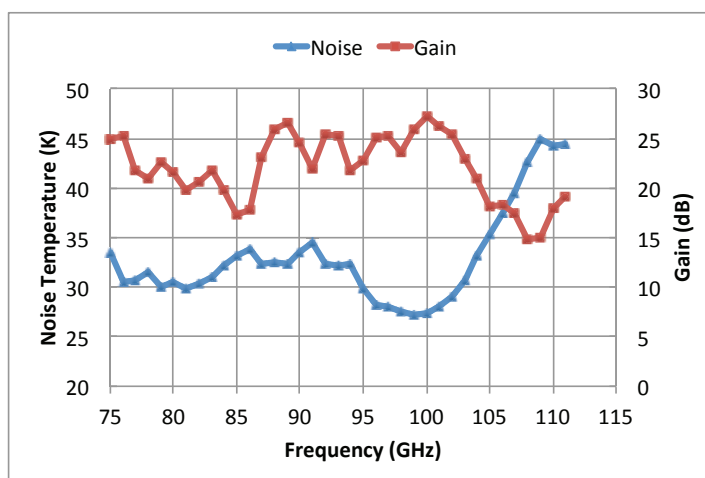
3.4 Performance

The cryogenic noise temperature of the *Argus* receiver modules was measured via the Y-factor method (see Appendix A). The Prototype 1, Prototype 2, and Pre-production receiver modules were measured with a variable thermal load (VTL) that was implemented with a waveguide termination, a heater, and a diode temperature sensor. The VTL temperature was set to 25 K and 50 K for the cold load and hot load, respectively. A piece of stainless steel waveguide provided a thermal break between the VTL and receiver module. The physical temperature of the MMIC module was fixed with a PID control loop while the VTL temperature was changed. The Production modules used a custom waveguide calibration vane that was developed at Caltech. The measurement results are shown in Figures 3.9 and 3.11. I personally measured the Prototype 1 and Pre-production receiver module performances. Each design iteration achieved lower receiver noise and wider bandwidths than the designs before it. All of the designs have good performance at the HCN (88.632 GHz) and HCO⁺ (89.189 GHz) high density gas tracers. The Prototype 2, Pre-production, and Production designs additionally have good performance at C¹⁸O (109.782 GHz) and ¹³CO (110.201 GHz), which are important tracers for the total molecular gas mass, while just the Pre-production and Production designs work well at the CO (115.271 GHz) line. Further details on the testing and results can be found in [45, 4, 46].

¹³Thunderline-Z TL1946

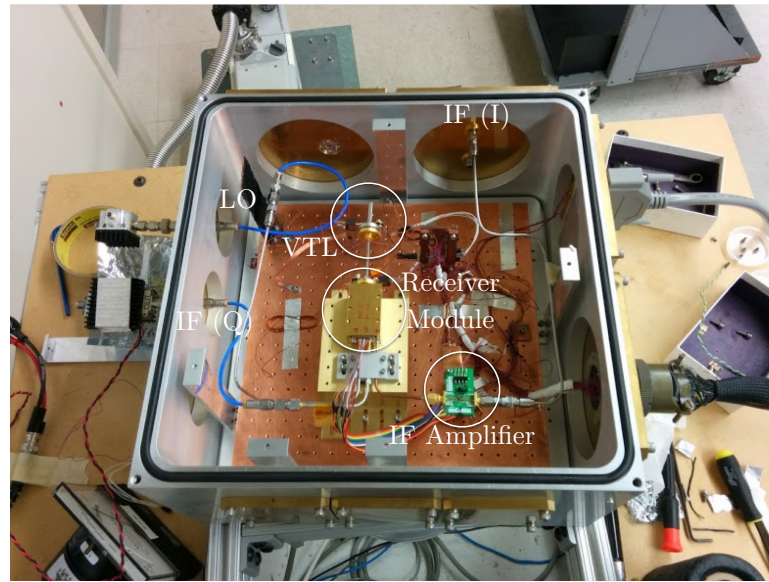


(a) Prototype 1

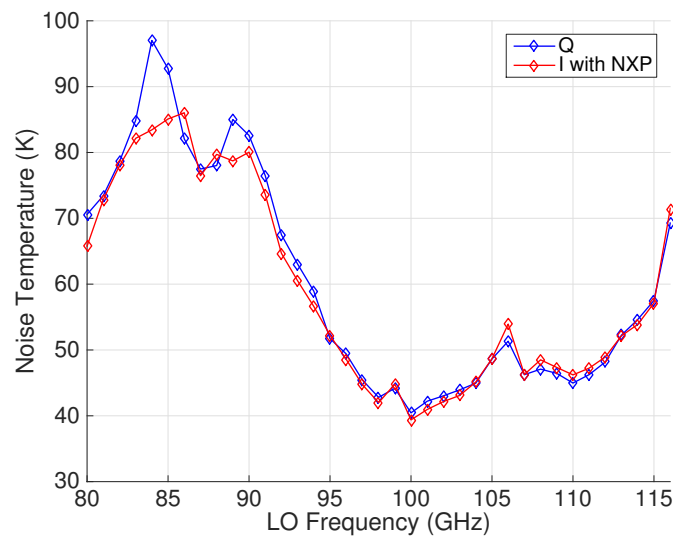


(b) Prototype 2

Figure 3.9: (a) The performance of the *Argus* Prototype 1 receiver module. This receiver has good performance from 81–102 GHz, which covers the astronomically important HCN (88.632 GHz) and HCO⁺ (89.189 GHz) high density gas tracers, but it does not cover any lines for CO or its isotopomers. (b) The performance of the *Argus* Prototype 2 receiver module, which is reproduced from [4]. The performance is good from 75–111 GHz, which is an improvement upon the Prototype 1 receiver. The Prototype 2 receiver can therefore measure the C¹⁸O (109.782 GHz) and ¹³CO (110.201 GHz) lines, which are important for tracing the total molecular gas mass and measuring the column density of the gas; however, like the Prototype 1 receiver, it is unable to measure the CO (115.271 GHz) line.



(a)



(b)

Figure 3.10: (a) The measurement setup for characterizing the noise temperature of the Pre-production receiver module. The I channel included an NXP BGU7003W amplifier, which was one of the *Argus* amplifier candidates (§4.1.2). The amplifier was added as a check that the gain of the receiver module was sufficiently high to overcome the noise from the amplifier and that the reflection between the two components was not prohibitively high. (b) The measured performance of the Pre-production Receiver in this measurement setup. The channel with the cryogenic IF amplifier had similar performance to the channel without the amplifier.

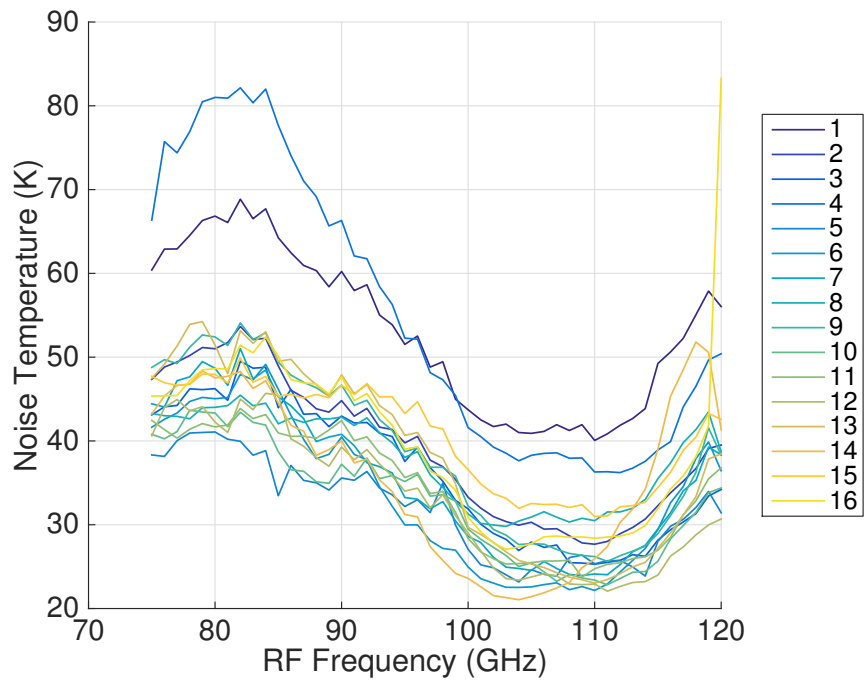


Figure 3.11: The measured performance for the Production *Argus* receiver modules as measured by Rohit Gawande at Caltech. The noise performance is good over the entire *Argus* bandwidth of 76–116 GHz, although the performance degrades below 85 GHz. The average receiver has 27–52 K noise temperature across the 76–116 GHz *Argus* bandwidth. There is a sweet spot at 108 GHz where it achieves a record low spot noise temperature of 23 K.

Chapter 4

Cryogenic Signal Distribution

This chapter presents the development of a scalable distribution system for the *Argus* IF, LO, and DC signals. The *Argus* receiver was designed to be highly scalable, which required a signal routing system that was mass-producible, economical, and compact. Designing the cryogenic signal distribution system was one of the major technical challenges associated with building a scalable array. It was accomplished by using multilayer printed circuit boards and flexible circuitry as the core components in the distribution system. The development of this subsystem was a major research endeavor that I undertook.

The cryogenic signal distribution system had two phases of prototyping before the *Argus* production boards were constructed. The first phase culminated in components for the 4-pixel *Argus* Prototype 2 array (§2.6), which had a fixed LO frequency and a very wideband IF frequency range. The second phase led to the production *Argus* boards and flexible circuitry, which accommodate a tunable LO frequency and a smaller IF frequency range. Both prototyping phases had four iterations, which were used to tweak designs and perfect the build process. The resulting multilayer board designs from both prototyping phases are presented in §4.1.1 and the flexible circuit microstrip lines, which are used to provide a thermal break in the IF between the cryogenic *Argus* front-end and the room temperature electronics, are discussed in §4.2. The interface between the multilayer routing boards and the flexible circuitry is provided by wirebonds, which is covered in §4.2.1. Finally, the performance of the fully assembled

signal distribution system is presented in §4.3.

4.1 Multilayer Printed Circuit Boards

The signals are routed to and from the miniaturized receiver modules (§3) via multilayer printed circuit boards. The boards provide a compact and cost effective way to route a large number of signals. A photograph and a CAD drawing for one of the production boards are shown in Figures 4.1a and 4.1b, respectively. The LO is routed on the top layer, the IF is routed on both the top layer and an interior layer, and the DC is on a separate interior layer. This section presents some of the key details of the board design. The choice of materials is discussed in §4.1.1, the IF system is presented in §4.1.2, and the LO system is covered in §4.1.3.

4.1.1 Construction

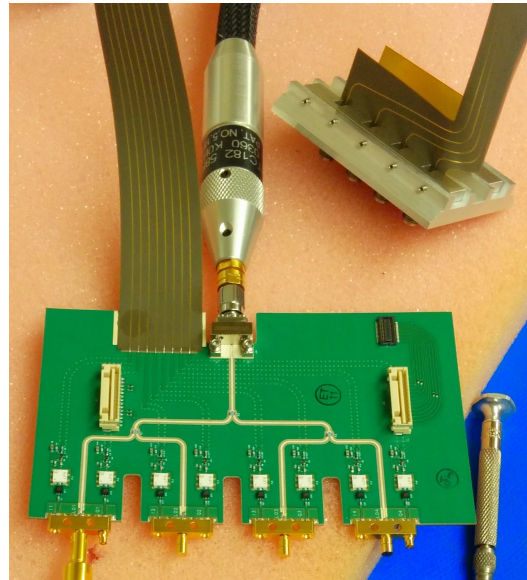
The multilayer printed circuit boards involve a number of boards or “cores”, which have copper on both sides and are laminated together with alternating layers of an adhesive material called “prepreg”¹. A summary of the multilayer board properties for the prototype and production designs is given in Table 4.1. The prototype board used cores that are made from hydrocarbons and ceramic², while the production boards were changed to PTFE-based cores³ for their lower loss properties (§4.1.3). The technical specifications for the cores and prepregs used in the two prototyping phases are given in Tables 4.2 and 4.3. Both of these substrates have high thermal conductivity and coefficients of thermal expansion well-matched to copper, which make them well-suited to cooling. Moreover, both materials have stable performance with frequency which simplifies the design process.

The prototype and production boards both use a core cap construction where the outermost materials in the boards (*i.e.* the caps) are cores and the layers are fused together with a single press. Table 4.4 shows the arrangement of the materials, known

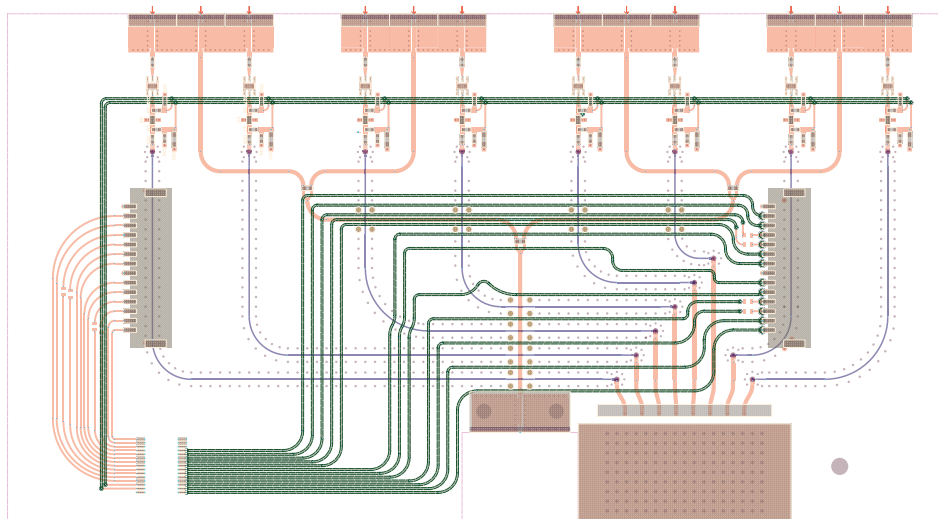
¹Prepreg is material that is “pre-impregnated” with a resin that cures when heated.

²Rogers RO4350B

³Taconic RF-35TC



(a)



(b)

Figure 4.1: (a) A photograph of the production multilayer routing board. (b) A CAD drawing of the production signal routing board. The board has six layers: a top layer with microstrip and co-planar waveguide (red), an embedded stripline layer (violet), an embedded layer for DC lines (green), and three reference ground planes (not shown). The pads at the top are for custom push-on connectors for the IF and LO (§3.3). The ground pad in the lower right is for attaching the flexible microstrip lines (§4.2).

Table 4.1: A summary of the multilayer routing board properties for the prototype and production receivers.

	Prototype	Production
Number of Layers	6	6
Thickness	0.069"	0.041"
Core Material	Hydrocarbon/Ceramic	PTFE-based
Finish	Electroless Nickel Immersion Gold (ENIG)	Immersion Silver (IAG)

Table 4.2: Technical specifications for the core materials used for constructing the multilayer printed circuit boards. The coefficients of thermal expansion (CTE) are well matched to copper in the transverse directions (*i.e.* x and y). The copper surface roughness is quoted for 0.5 oz/ft² electrodeposited copper. The PTFE-based cores are capable of supporting lower loss transmission lines than the hydrocarbon/ceramic cores because of their superior loss tangent and copper surface roughness.

	Hydrocarbon/Ceramic Cores	PTFE-based Cores
Product	Rogers RO4350B	Taconic RF-35TC
Available Thicknesses	0.004", 0.0066", 0.010", 0.0133", 0.0166", 0.020", 0.030", 0.060"	0.005", 0.010", 0.020", 0.030", 0.060"
Dielectric Constant (ϵ_r)	3.48 @ 10 GHz	3.50 @ 10 GHz
Loss Tangent ($\tan \delta$)	0.0037 @ 10 GHz	0.0011 @ 10 GHz
Thermal Conductivity	0.69 W/m/K	0.92 W/m/K
CTE_x	14 ppm/°C	11 ppm/°C
CTE_y	16 ppm/°C	13 ppm/°C
CTE_z	35 ppm/°C	34 ppm/°C
Copper Surface Roughness (Dielectric Side)	2.8 μ m	1.16 μ m

Table 4.3: Technical specifications for the prepreg materials used for constructing the multilayer printed circuit boards. The low loss tangent of the prepreg for PTFE-based cores allow for transmission lines with very low insertion losses.

	Prepreg for Hydrocarbon/Ceramic Cores	Prepreg for PTFE-based Cores
Product	Rogers RO4450B	Taconic FR-28-0040-50
Thickness	0.004"	0.0041"
Dielectric Constant (ϵ_r)	3.54 @ 10 GHz	2.75 @ 10 GHz 2.70 @ 40 GHz
Loss Tangent ($\tan \delta$)	0.004 @ 10 GHz	0.0014 @ 10 GHz 0.0017 @ 40 GHz
Thermal Conductivity	0.60 W/m/K	0.25 W/m/K

as the “stack-up”, that was used to construct the multilayer routing boards. In this approach the signal lines are etched directly onto the copper-cladded cores instead of being patterned onto foil, which leads to better impedance control. The single press lamination is also more reliable than a multi-stage pressing construction. An attempt was made to fabricate a multilayer board using a two-stage press, which was unsuccessful because the shrinkage and expansion of the copper traces during the first press led to misalignment of the traces in the second press. The delivered boards in this attempt therefore had an unexpected number of opens and shorts.

There are a couple of constraints on the thicknesses of the different layers in the multilayer board stack-up. Warpage is an important factor that must be considered when creating a stack-up. Best practice dictates that a stack-up is balanced, meaning that the board is symmetrical about its mid-plane⁴; a balanced stack-up minimizes the risks of warpage. An additional constraint is that the edge mount connectors that are used for the LO perform best when the total board thickness is less than a quarter wavelength at the highest operating frequency. The maximum LO frequency for *Argus* is 58 GHz, which translates to a maximum board thickness of 0.0509". This criterion prevents connector resonances at the edge of the board between the top and bottom layers, a phenomenon that was seen in prototyping and which is discussed in

⁴In a core cap construction the mid-plane would ideally be in the center core.

Table 4.4: Details of the multilayer routing board stack-ups. The metal layers are all 0.5 oz/ft² electrodeposited copper, which has a thickness of 0.0007”.

Prototype	Production
Layer 1 – IF/LO Signal Lines	
Core (0.010”)	Core (0.010”)
Layer 2 – Ground Plane	
Prepreg (0.016”)	Prepreg (0.008”)
Layer 3 – IF Signal Lines	
Core (0.0166”)	Core (0.010”)
Layer 4 – Ground Plane	
Prepreg (0.012”)	Prepreg (0.004”)
Layer 5 – DC Bias Lines	
Core (0.010”)	FR4 (0.005”)
Layer 6 – Ground Plane	

further detail in §4.1.3. It was not practical to achieve both perfect balance and a total thickness of less than 0.0509”; however, the stack-up for the production board in Table 4.4 was chosen to have a reasonable compromise between balance, which prevents warpage, and thinness, which improves the edge mount connector performance.

4.1.2 IF Design

The IF chain on the multilayer routing boards, which is shown schematically in Figure 2.5, provides low-noise amplification and routes the signals away from the miniaturized receiver modules (§3). Prototyping the IF chain involved identifying and testing commercial surface mount components for their suitability for cryogenic operation. In particular, a number of commercial amplifier candidates were characterized cryogenically as described in §4.1.2. After amplification, the IF signals are routed on one of the interior layers of the board using stripline in order to allow the IF and LO lines to cross as pictured in Figure 4.1b. An RF transition between layers was designed that works to 20 GHz and is presented in §4.1.2. The IF chain additionally includes an attenuator⁵ at the input to improve the impedance match with the miniaturized

⁵Hittite HMC652LP2E

receiver modules and a low-pass filter⁶ that defines the IF bandpass. The performance of the assembled IF chain is presented in §4.3.

IF Amplifiers

One of the foremost differences between the prototype and production routing boards was the IF amplification scheme. Both designs utilized a commercial surface mount amplifier, but the vastly different bandwidth requirements (see Table 2.3) led to very different approaches. The prototypes implemented a broadband amplifier⁷ that worked to 20 GHz. These devices dissipated too much power to be placed on the multilayer routing board that is attached to the second stage of the cryostat (~ 25 K) and so they were instead placed on a second routing board that was heat sunk to the first stage of the cryostat (~ 70 K), which has more heat lift. The production design, on the other hand, had a narrower IF bandwidth specification (0.90–2.15 GHz) and therefore lower power devices could be utilized; this allowed for the IF amplifier to be thermally attached to the second stage of the cryostat (~ 25 K).

Four IF amplifier candidates, which are summarized in Table 4.5, were evaluated cryogenically before the production boards were constructed. Data sheets for all of these amplifiers were available with room temperature specifications. These particular amplifiers were chosen as candidates because their bandwidth covered the *Argus* IF band, they exhibited low noise at room temperature, and their required bias powers were modest. The amplifiers were cooled in the test setup shown in Figure 4.2, which included stainless steel semirigid coaxial cables to provide a thermal break in the signal lines. The cryogenic performance of the amplifiers is shown in Figure 4.3. The Avago VMMK-2303 was selected as the IF amplifier for the production design because its cryogenic gain was relatively constant with frequency, its noise temperature was among the best of the four candidates, and its quoted input and output reflection coefficients⁸ were significantly better than the other amplifiers. Before finalizing the selection of the Avago VMMK-2303, one of the test boards was subjected to multiple

⁶Mini-Circuits LFTC-3300+

⁷Hittite HMC460LC5

⁸<http://www.avagotech.com/docs/AV02-2002EN>

thermal cycles with setups that happened to vary slightly. The cryogenic gain at each cooldown is shown in Figure 4.4. The board did not fail after repeated thermal cycling and the minor variations in gain could potentially be explained by setup changes, including differences in the thermal resistance of the heat sinks that affected the final temperatures.

Table 4.5: Specifications for the *Argus* IF amplifier candidates for the production design. All of the amplifiers cover the 0.90–2.15 GHz *Argus* IF bandwidth.

Model	Technology	Bandwidth	
		f_{min} (GHz)	f_{max} (GHz)
NXP BGU7003W	SiGe	0.04	6.0
Avago MGA-87563	GaAs	0.50	4.0
Infineon BGA628L7	SiGe	0.40	6.0
Avago VMMK-2303	GaAs E-pHEMT	0.50	6.0

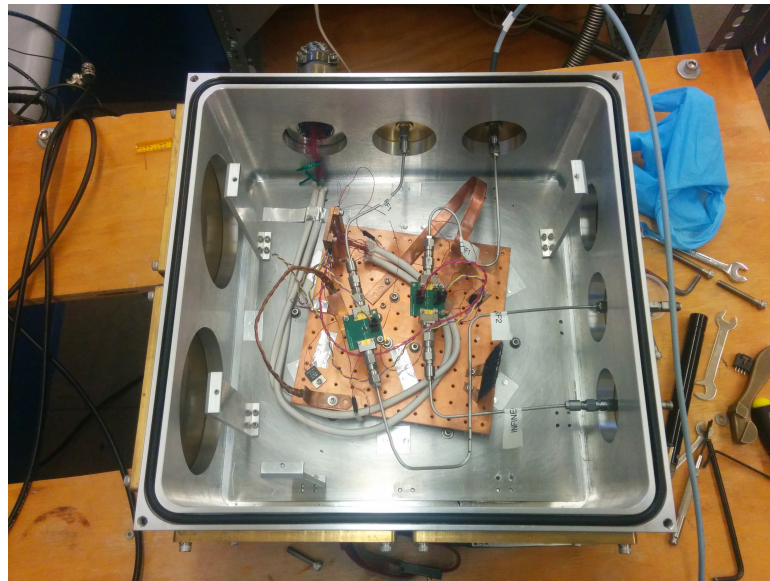
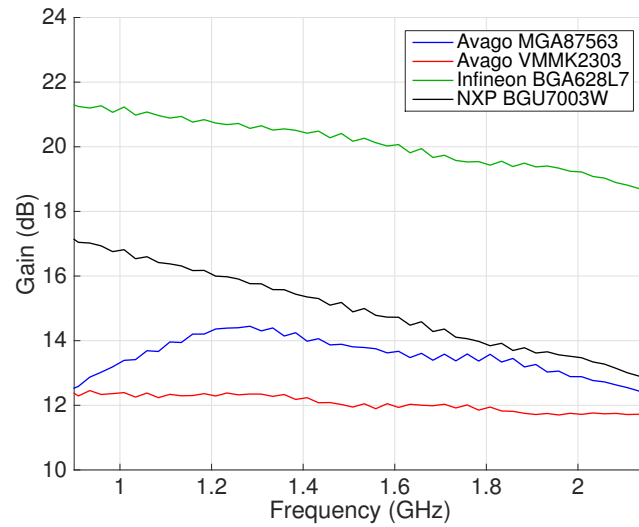
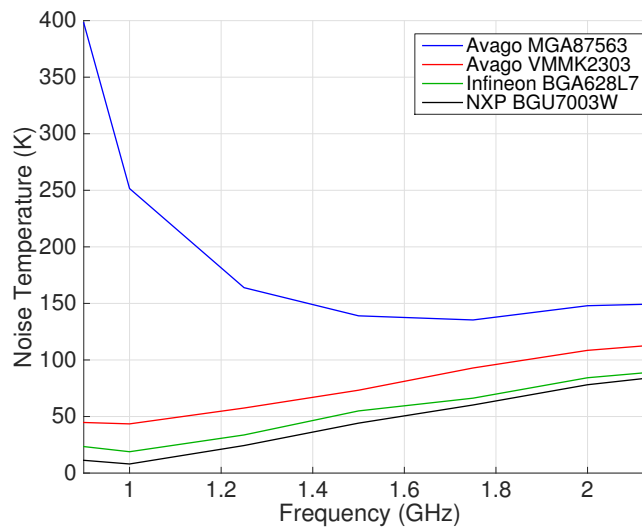


Figure 4.2: The measurement setup for cryogenically characterizing the IF amplifier candidates. Semirigid coaxial cables with stainless steel outer conductors were used as the thermal break between the cooled amplifier and the room temperature test components.



(a)



(b)

Figure 4.3: The performance of the four cryogenic IF amplifier candidates for *Argus*. Shown here are (a) the gain and (b) the noise temperature over the 0.90–2.15 GHz IF band. Notably the noise temperatures were *not* corrected for the effect of the coaxial cables; the noise temperatures are for the entire system shown in Figure 4.2.

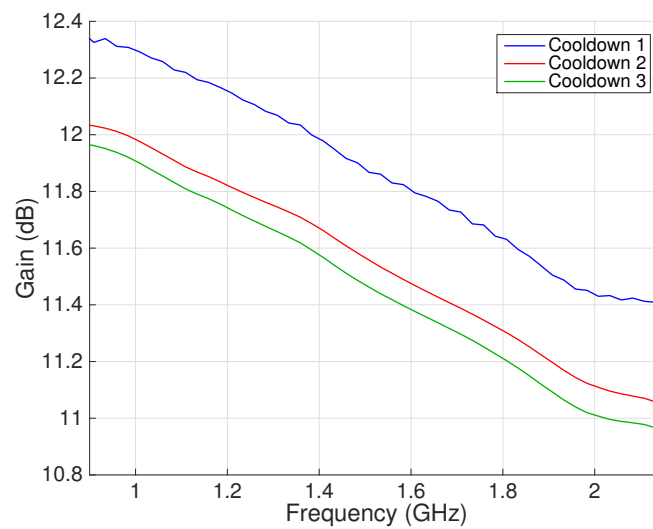
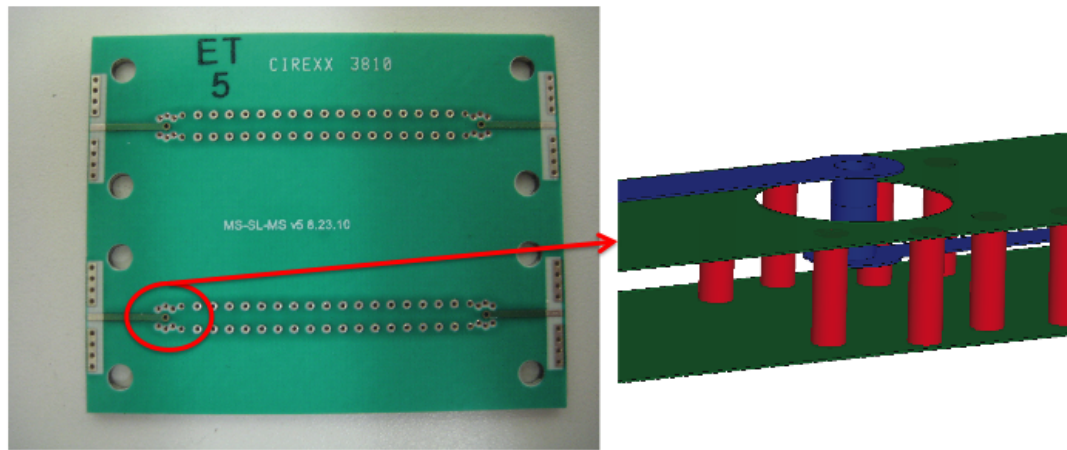


Figure 4.4: The Avago VMMK-2303 amplifier was thermally cycled several times and the gain was checked for reproducibility. The amplifier did not fail after repeated coolings. This model was eventually selected as the cryogenic IF amplifier for *Argus*. The measurements were interspersed over the span of months which meant that the test setups were similar but not exactly the same. Differences in the amplifier temperature might account for the slight change in gain levels.

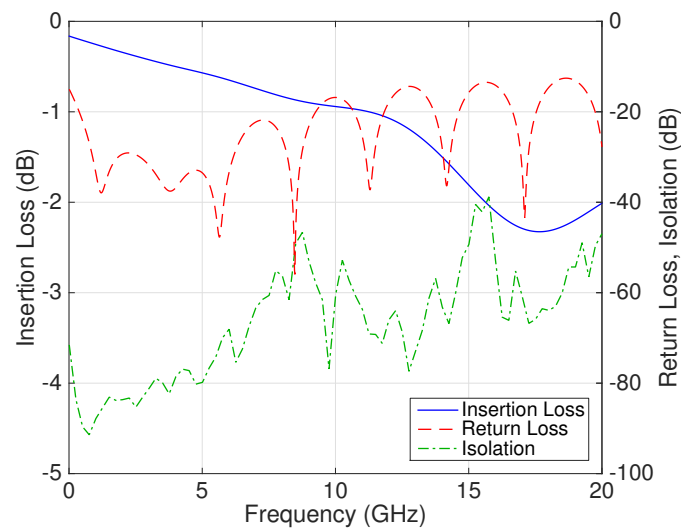
Microstrip-to-Stripline Transition

The stripline layer is accessed via stripline-to-microstrip transitions, which are illustrated in Figure 4.5a. These transitions employ coaxial vias [58], where the signal via is surrounded by a number of ground vias, forming a coaxial transmission line. The ground vias also function to suppress unwanted parallel plate modes that are generated at the transition and propagate through the dielectric. A wall of vias along each side of the stripline was included to further reduce cross-talk between lines. A test board with back-to-back stripline-to-microstrip transitions was constructed to test the performance of the transitions as shown in Figure 4.5a. The test board has two identical signal lines that are spaced by 1.0". The total length of the transmission lines is 1.5". The performance of the test board is shown in Figure 4.5b. The measurements were made up to 20 GHz, which is well above the *Argus* IF band of 0.90–2.15 GHz; the wide bandwidth performance could potentially be utilized for a future *Argus* upgrade. The measurements include the performance of the test connectors⁹, which were the reference planes for these measurements. The worst case return loss is 15 dB over the DC–20 GHz band, which is suitably low to avoid significant standing waves between the coaxial transitions and other components. The insertion loss is less than 2.5 dB, which is dominated by the transmission lines. The upper limit for the loss per coaxial transition is then 1.25 dB at 20 GHz and significantly less at lower frequencies. Finally, the average isolation is 53 dB across the band with a peak of 39 dB. The cross-talk of the entire IF system should therefore not be dominated by the transmission lines on the multilayer routing boards, but should instead be limited by the flexible circuitry (§4.2).

⁹Southwest Microwave 1492-02A-5 & 1493-01A-5



(a)



(b)

Figure 4.5: (a) Left: A photograph of a test board with two back-to-back stripline-to-microstrip transitions. The two signal chains are separated by 1.0". Right: A CAD model of the transition. (b) The performance of the test board. These measurements demonstrate that the microstrip-to-stripline transitions are not the dominant source of insertion loss in the IF chain. The return loss is better than 20 dB over the *Argus* band, which minimizes the level of standing waves in the system.

4.1.3 LO Design

The primary challenge in designing the LO system for the multilayer routing boards was achieving sufficient LO power at the output of the boards. The four routing boards are preceded by a four-way LO splitter at room temperature (see Figure 2.5.3) and are themselves responsible for splitting the LO four ways to complete the 16-way split. These two sets of splitters reduce the LO power reaching the miniaturized receiver modules by a factor of 16. It is therefore imperative to minimize any further reductions in LO power. The insertion loss from transmission lines and connector launches was minimized through several iterations of the design and is presented in §4.1.3. It was also important that the splitter had low insertion loss over the entire *Argus* bandwidth of 39–58 GHz, which is demonstrated in §4.1.3.

Microstrip Loss

The LO signals are routed on the top layer of the multilayer routing board on microstrip lines. There are three dominant sources of loss for a microstrip circuit: substrate loss, metal loss, and radiation loss. Substrate losses occur when the fields inside the substrate dissipate into heat; this loss is quantified by the loss tangent ($\tan \delta$). Metal loss occurs because the copper has finite conductivity, which leads to ohmic losses. The resistance, R , for a microstrip line is

$$R = R_{sh} \frac{L}{W} \quad (4.1)$$

where R_{sh} is the sheet resistance, L is the length and W is the width of the conductor. Additionally, the metal loss is exacerbated by the surface roughness of the metal, which increases the effective L . Finally, the radiation losses are primarily from impedance discontinuities that radiate. Coaxial connector launches in particular can be a major source of radiation losses, potentially becoming significant at higher frequencies (typically above 30 GHz).

Each of the microstrip loss mechanisms was mitigated in the *Argus* production boards via careful design. The prototype cards experienced unacceptably high microstrip losses at the LO frequencies of 39–58 GHz, which required design changes

that are described below. The high microstrip losses are problematic because they lead to insufficient LO power at the mixer and a severe degradation in its conversion loss (§3.2.2).

The substrate loss is minimized simply by choosing core and prepreg materials with low loss tangent. The loss tangent improved by a factor of 3.4 between the prototype designs and production designs, as shown in Table 4.2, which significantly improved the substrate losses. Additionally, the solder mask contributes significantly to the substrate loss. This contribution was reduced between the prototype and production designs by removing the solder mask around the LO traces. The measured insertion loss of test boards with different amounts of solder mask removed around the vicinity of the LO traces is shown in Figure 4.6a. In the production design, the solder mask was removed over a width of 0.066" beyond which there are diminishing returns.

The metal loss is decreased by using larger microstrip widths (per Equation 4.1) and utilizing metals with high conductivities and low surface roughnesses. In practice larger widths can be achieved for a given impedance by either using a substrate with a low dielectric constant, ϵ_r , or a thicker substrate. Both cores have $\epsilon_r \approx 3.5$ and a thickness of 0.010", which requires a microstrip width of ~ 0.021 " for a 50Ω line¹⁰. The metal loss was improved between the prototype and production designs primarily through improved surface roughness on the dielectric side of the copper traces. The surface roughness of the electrodeposited copper improved by over a factor of two between the designs as shown in Table 4.2. Another consideration was the type of metal finish that the copper was plated with in order to achieve improved wirebonding and soldering. Despite the fact that most of the signal currents flow on the dielectric side of the copper traces, there is a significant current density that travels through the finish. It was therefore also important to select a finish with high conductivity for managing the metal losses. The insertion loss for boards with no finish (*i.e.* bare copper), an IAg finish, and an electroless nickel immersion gold (ENIG) finish are shown in Figure 4.6b. The IAg finish does not increase the insertion loss of the microstrip lines since its conductivity is similar to copper, but the ENIG

¹⁰Care must be taken to avoid resonances or overmoding in the microstrip line. The rule of thumb is to keep $W < \lambda/8$ and $h_{substrate} < \lambda/4$.

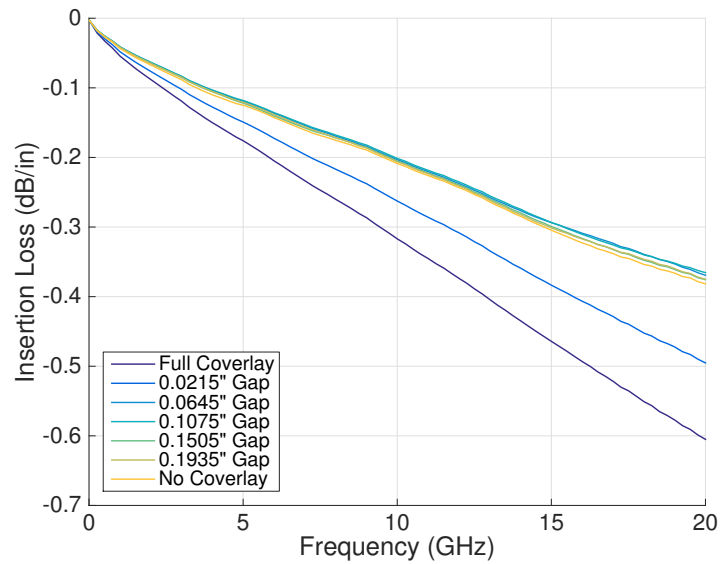
finish increases the loss by about 50% because the nickel layer has relatively high conductivity. The prototype boards used an ENIG finish because the possibility of increased loss from the finish had not been considered in that design, while the *Argus* production boards used an immersion silver (IAg) finish.

Radiation losses were improved by changing the connector launch. In the prototype design, there were many frequencies with very poor transmission through the LO signal path. Through simulation it was discovered that the poor performance was being caused by radiation at the connector launch that was then resonating in the gap between the connector and the board. The resonance is illustrated in A CAD image from a finite element model solver¹¹ as shown in Figure 4.7. The resonances were detuned in the production board by making the following modifications:

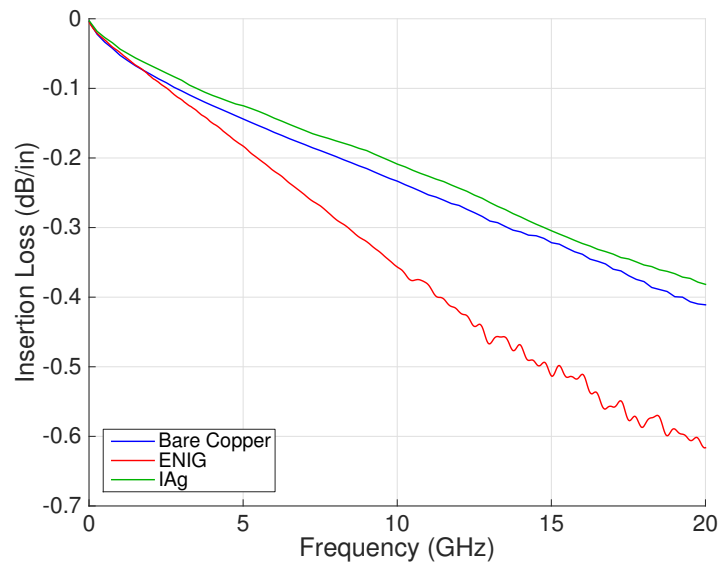
- The board thickness was decreased by a factor of 0.8 between designs, which moved the resonant frequency of the cavity formed between the board and the connector out of the *Argus* LO frequency range.
- The final production board utilized a coplanar waveguide launch instead of microstrip. The coplanar waveguide launch keeps the fields more contained due to the proximity of its ground planes.
- The interior ground planes were receded away from the board edge, which reduced the quality factor of the cavity that had formed.

The insertion loss of the LO microstrip lines improved significantly after addressing the metal loss, the substrate loss, and the radiation loss as discussed above. The insertion loss of a test board after the modifications is shown in Figure 4.9. It should be emphasized that all of these measurements were performed at room temperature. A further reduction in loss is expected at cryogenic temperatures at which the conductivity of copper is higher.

¹¹ANSYS HFSS



(a)



(b)

Figure 4.6: (a) The insertion loss is plotted for various levels of solder mask removal. The solder mask contributes to substrate losses. The solder mask was removed over a width of three times the microstrip trace width. Further removal does not improve the insertion loss. (b) The insertion loss is shown for three different choices of surface finish: none (*i.e.* bare copper), immersion silver (IAg), and electroless nickel immersion gold (ENIG). The production boards utilized an IAg finish, which does not degrade the insertion loss.

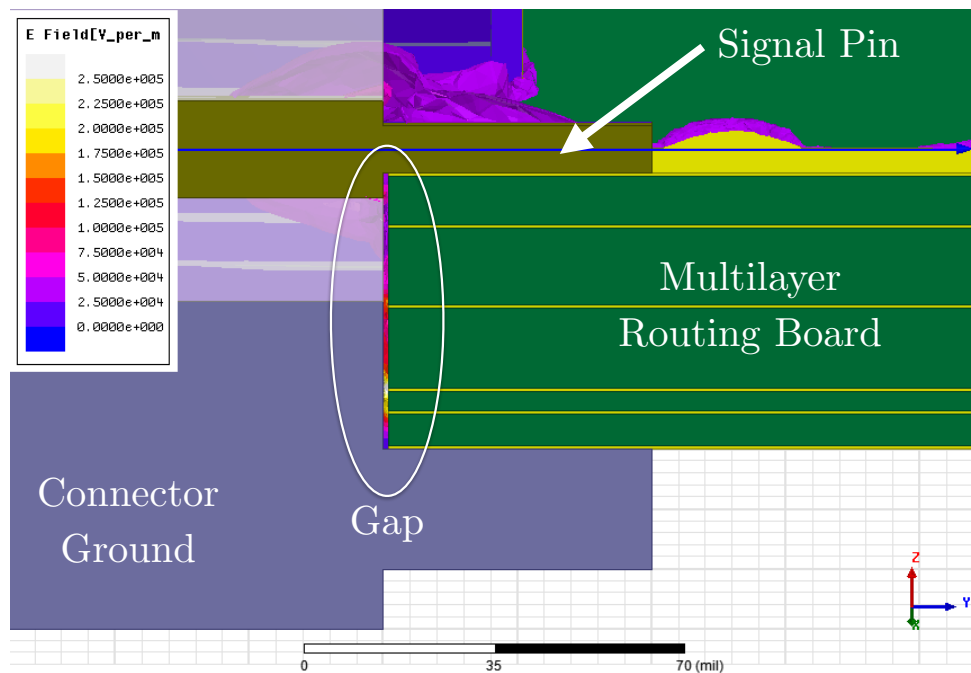


Figure 4.7: A finite element model of a prototype version of the *Argus* LO coaxial connector launches. The signal is shown radiating into the 0.001” gap between the board and the connector, which formed a resonant cavity. This effect led to poor connector performance. This effect was mitigated by decreasing the board thickness, changing from a microstrip launch to coplanar waveguide, and receding the interior layers of the multilayer routing board.

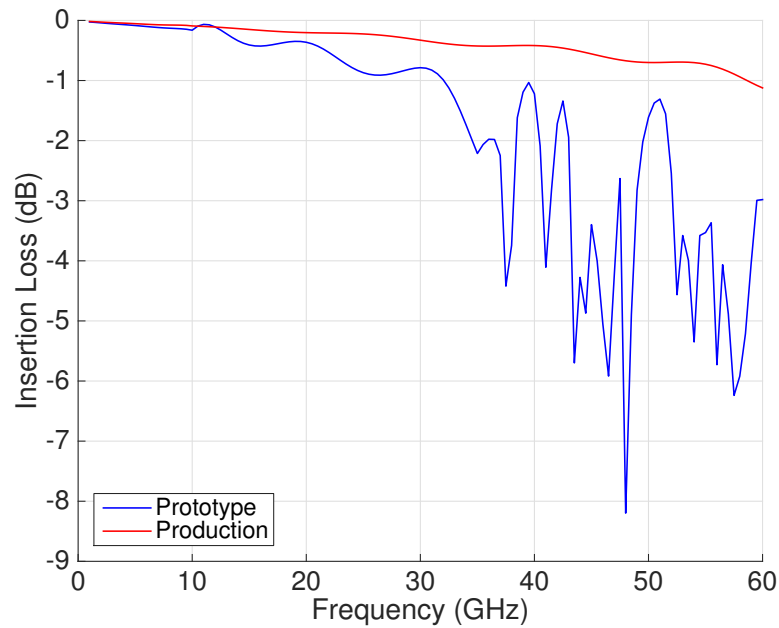


Figure 4.8: The simulated insertion loss for the LO coaxial connector launches. The prototype board suffered from a resonance in the gap between the multilayer printed circuit board and the connector as illustrated in Figure 4.7. The simulated insertion in this prototype design is high and has many spectral features, which can be attributed to this resonance. The resonance was detuned by decreasing the board thickness, changing from a microstrip launch to a coplanar waveguide launch, and receding the ground planes. The resulting simulated performance is adequate for providing sufficient LO power to the *Argus* receivers over the 39–59 GHz band.

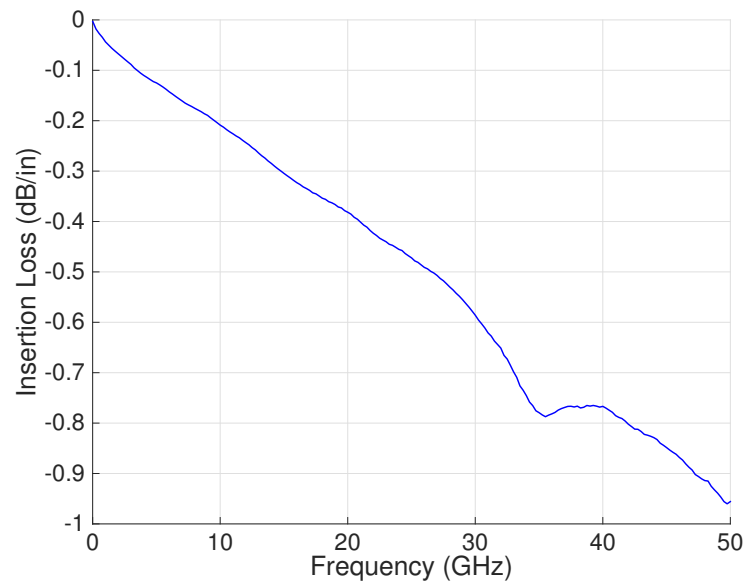


Figure 4.9: The microstrip insertion loss per inch after the substrate losses, metal losses, and radiation losses were improved via prototyping.

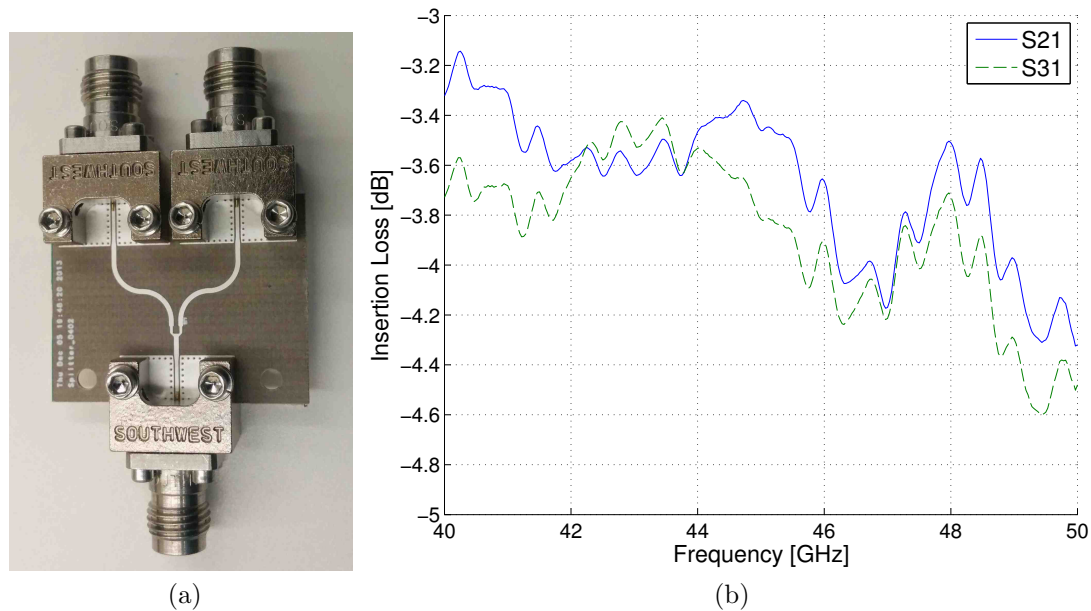


Figure 4.10: (a) A photograph of a Wilkinson splitter test board on 0.010" PFTE-based core. (a) The measured performance of the Wilkinson splitter test board. The insertion loss of the connectors and the microstrip leads have been subtracted.

Splitters

The prototype and production designs used different LO splitters. The prototype card utilized a rat-race coupler to split the LO. It was selected because it is straightforward to manufacture due to its planar design and lack of surface mount components; however, it is not inherently wideband; the output ports have an amplitude imbalance away from the design frequency. The LO splitting on the production boards instead used a Wilkinson splitter, which is pictured in Figure 4.10a. A Wilkinson splitter was chosen because it is relatively broadband, compact, and is impedance matched at all ports. The 100Ω isolation resistor is a high frequency flip-chip resistor¹², which has an appropriately small reactance up to 50 GHz. The performance of the splitter is shown in Figure 4.10b, which demonstrates that splitter has <2 dB insertion loss beyond the 3 dB splitting.

¹²Vishay Thin Film Microwave Resistors

4.2 Microstrip Flex Circuit Interconnects

Microstrip lines on flexible circuitry provide a means for transferring IF signals between temperature stages with low thermal loading. There is one IF flexible circuit in *Argus* per card and each card carries eight signals. The flexible circuit substrate is 0.005" polyimide¹³ and has a 0.0007" thick copper cladding. The microstrip traces are 0.011" in width with a 1.0" reference ground plane. The cross sectional area of copper for one flexible circuit carrying eight signals is 0.0007 in², which is comparable to semirigid cable and sufficient for providing a thermal break. A prototype version of the flexible circuitry was constructed as pictured in Figure 4.11a. The total length is 10.6" and the center-to-center line spacing is 0.10". The ground plane on the prototype is split into two: one half has a solid ground plane and the other half has a patterned ground plane for lower thermal conductivity. The RF performance for this prototype, as reproduced from [5], is shown in Figure 4.11b. The microstrip flexible circuitry with solid ground planes yields an insertion loss of 0.076 dB/GHz/in and a cross-talk of <25 dB up to 20 GHz. The measured cross-talk is for nearest neighbor lines; the nearest neighbor lines run parallel for 8.2–8.8". The patterned ground plane leads to a very slight increase in insertion loss and a modest increase in cross-talk. It was not used in the *Argus* cards because the solid ground plane had sufficiently low heat load; however, the patterned ground plane would likely prove useful in future *Argus*-like instruments with more pixels. The prototyping of the flexible circuitry was done by Andrew Harris at the University of Maryland, which is detailed in [5]. I implemented the technology into the *Argus* focal plane array.

The flexible circuitry requires custom interconnects at the multilayer routing board and cryostat wall. At the board interface, the ground plane of the polyimidecircuitry is soldered to a ground pad on the top layer of the board. The signal lines are then intended to be connected via aluminum wire bonds, although in practice these lines were attached with wire and solder in the *Argus* production cards. This interface is covered in more detail in §4.2.1. At the cryostat wall, a custom feedthrough was designed, which is shown in Figure 4.12. The hermetic seal at the feedthroughs is

¹³DuPont Pyralux AP-8555R

provided by glass bead connectors, which are epoxied to the metal base. The signal pins are soldered to the microstrip lines on the flexible circuitry, while custom clamps provide grounding and strain relief.

4.2.1 Wirebond Interface

The connection between the multilayer routing boards and the flexible circuits was designed to be formed by soldering the ground plane of the flexible circuit to a ground pad on the top layer of the board and then wire bonding the signal traces together. A photograph and a finite element model¹⁴ of this interface is shown in Figures 4.13a and 4.13b, respectively. The wire bond is a wedge-bonded aluminum wire bond with a diameter of 0.001". The expected performance of this interface, as obtained through the finite element model, is shown in Figure 4.13c. The insertion loss is low from DC to 15 GHz, but was seen to degrade significantly with increasing wirebond lengths. The return loss is better than 20 dB across the *Argus* band of 0.90–2.15 GHz, but is marginal above 10 GHz. If this design were used for a future *Argus*-like instrument with >10 GHz IF bandwidth, then it would be desirable to improve the impedance match at higher frequencies¹⁵.

In the *Argus* production boards the wirebond interface had to be replaced by a soldered wire connection because of a mistake during assembly. The printed circuit board assembly company accidentally got solder over the wirebond pads, which made them unsuitable for wirebonding. The soldered wire connection was adequate for the *Argus* IF range of 0.90–2.15 GHz. There were no features in the measured performance of the IF system (§4.3.1) that could be attributed to the wirebonds; however, this solution would likely not work well at higher frequencies.

¹⁴ANSYS HFSS

¹⁵This could be accomplished by using multiple wirebonds, which would decrease the inductance of the wirebond connection, or by introducing a capacitive match to counteract the inductance of the wirebond.

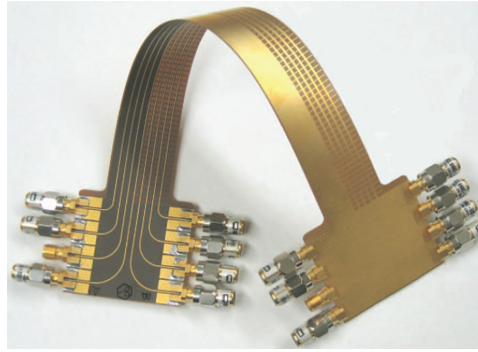
4.3 Performance

4.3.1 IF System

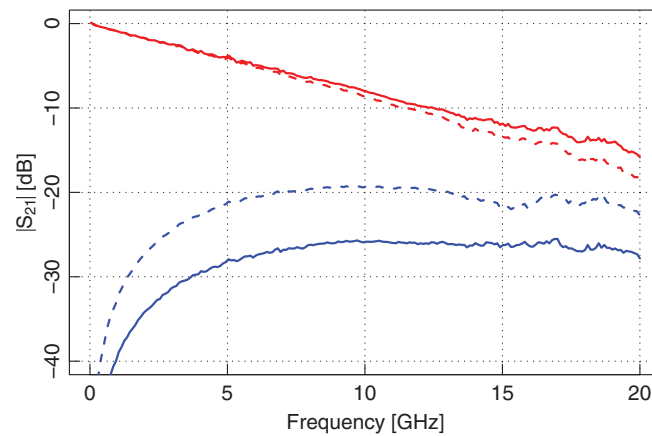
The performance for four channels of IF system was measured cryogenically. The gain, noise temperature, and cross-talk are shown in Figure 4.14. The ripple that is seen in the gain is from the switches that were used in the test setup and not from the instrument itself. The gain is sufficiently high and the noise temperature is sufficiently low that the noise contribution from all receiver components after the miniaturized receiver modules should have a contribution of <1 K to the receiver noise per Equation 2.8. The noise temperature of the multilayer routing boards is significantly higher than that of the the amplifier (§4.1.2) because of the 2 dB attenuator at the input (see the schematic in Figure 2.5). The cross-talk is less than 20 dB across the *Argus* band, which is dominated by the microstrip flexible circuitry (§4.2).

4.3.2 LO System

The LO performance of the multilayer routing board was checked at room temperature with a vector network analyzer. The insertion loss for a typical board is shown in Figure 4.15. The ripple is due to connector mismatch. While the impedance match at the LO connectors was improved significantly through prototyping (§4.1.3), the impedance match on the production *Argus* boards was still marginal. The performance of the snap-on connectors that interface with the miniaturized receiver modules was sensitive to assembly tolerances. Insufficient solder between the ground on the connector and the board as well as connector misalignment were seen to degrade performance. Despite the ripple that is seen in the passband of the routing boards, the LO power impinging on the miniaturized receiver modules was sufficient (§2.5.3).

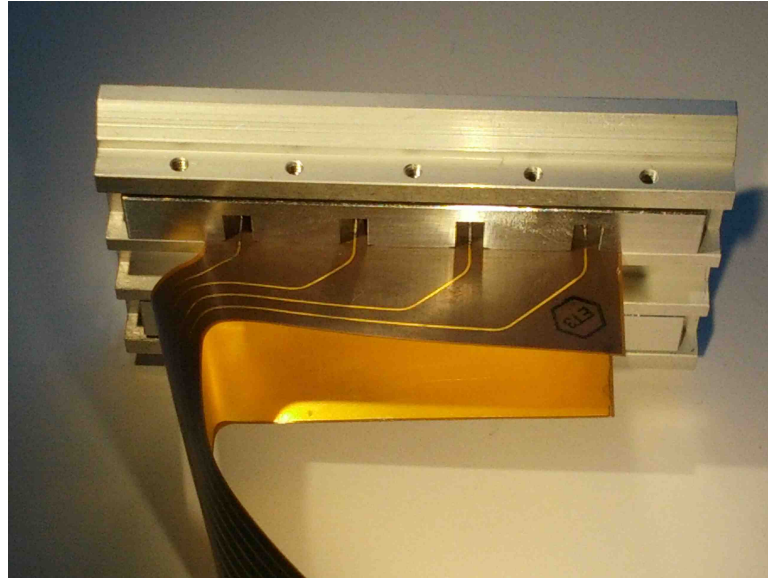


(a)



(b)

Figure 4.11: (a) A photograph of a prototype of the microstrip flexible circuitry. (a) The performance of the prototype as reproduced from [5]. The insertion loss is shown in red and the nearest neighbor cross-talk is shown in blue. The solid traces correspond to microstrip lines with a solid ground plane and the dashed traces correspond to the patterned ground plane. The patterned ground plane decreases the thermal conductivity at the expense of a small increase in insertion loss and a modest increase in cross-talk; the patterned ground plane was not implemented in the *Argus* boards because the heat loading from the flexible was already sufficiently low. The solid ground plane provides an insertion loss of 0.076 dB/GHz/in.



(a)



(b)

Figure 4.12: A hermetic feedthrough was designed for the IF signals. (a) On the inside of the cryostat the flexible microstrip lines are soldered to glass bead connectors. Clamps provide a ground connection and strain relief. (b) The IF interface on the outside of the cryostat is a pattern of 8 SMA connectors.

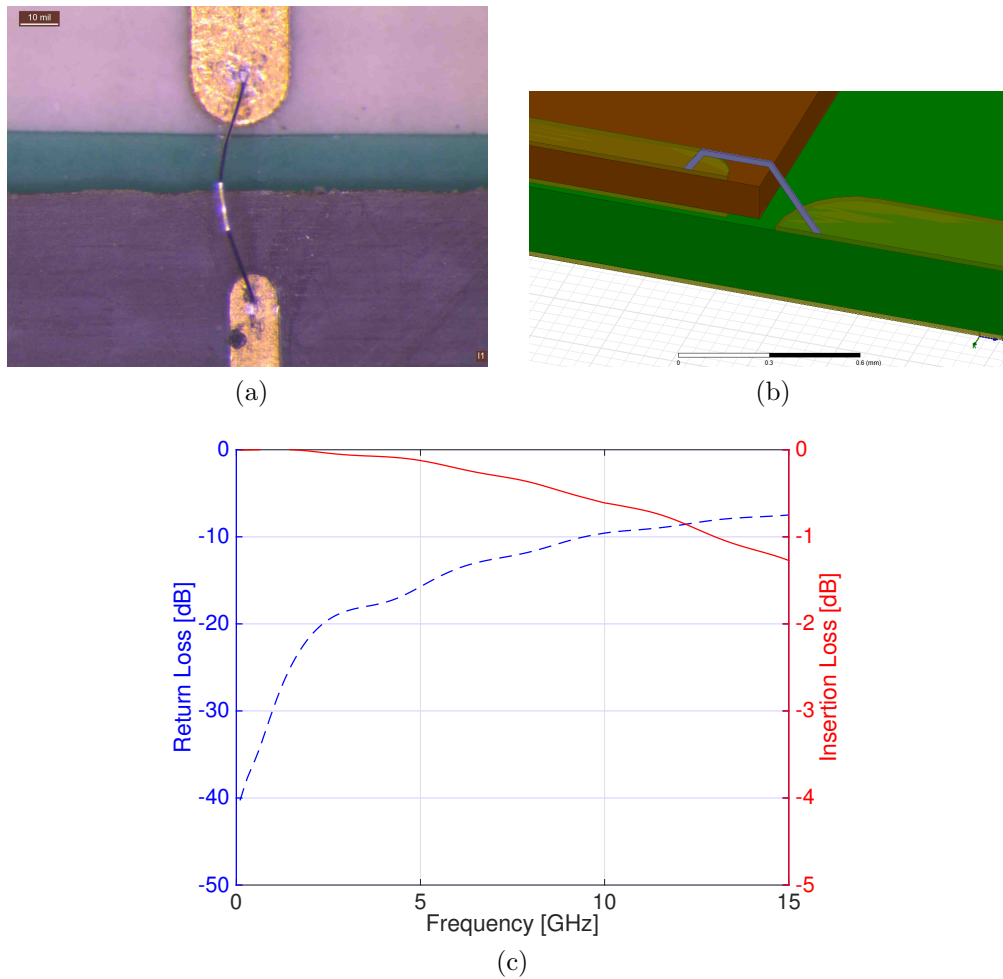


Figure 4.13: (a) A photograph of the wirebond interface. (b) An HFSS model of the wire bond to flexible circuit interface. The model is split in half in order to capitalize on the H-plane symmetry of the fields. (c) The insertion loss and return loss for this interface. The microstrip lines have been de-embedded from the model.

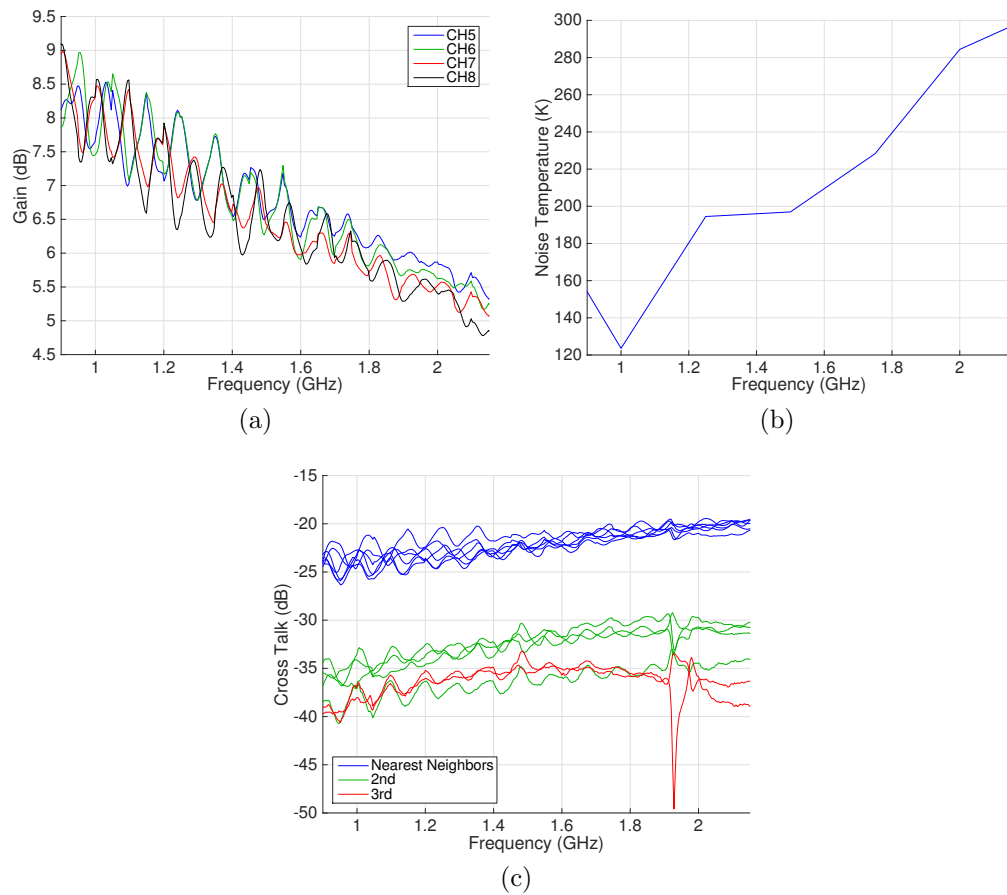


Figure 4.14: The cryogenic IF routing was characterized for four channels. Shown in the sub-panels are (a) the gain, (b) the noise temperature, and (c) the cross-talk between channels.

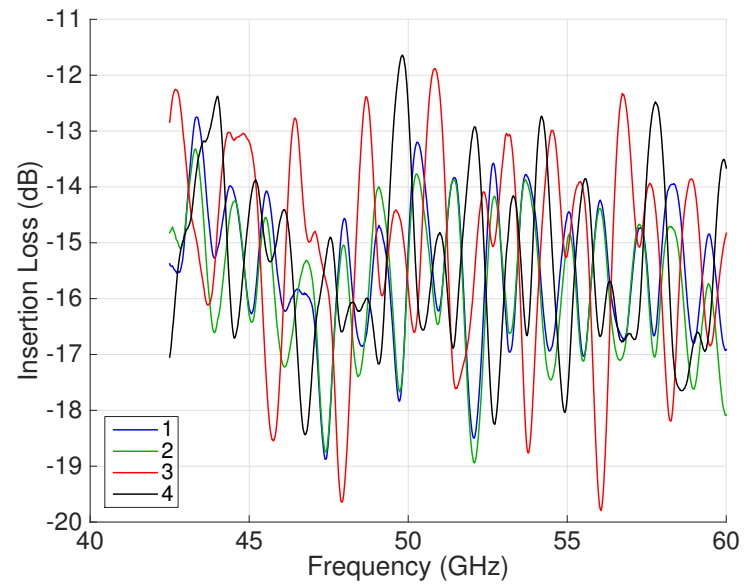


Figure 4.15: The insertion loss in the LO chain for a typical multilayer routing board. The 4-way split accounts for 6 dB of the insertion loss. The ripple is due to impedance mismatches at the input and output connectors. The performance is sufficient to route enough LO power to the miniaturized receiver modules (§2.5.3).

Chapter 5

Argus Commissioning

The 16-pixel *Argus* receiver is a powerful millimeter-wave imager that is now operational at the Robert C. Byrd Green Bank Telescope (GBT). *Argus* measured first light on March 30, 2016; this culminated roughly two years of integration and testing of the array and several years of prototyping before that. The performance of the array needed to meet the specifications that are dictated by the *Argus* science objectives (§2.4) before it could be installed on the telescope. The instrument was characterized in the lab first at Stanford in 2014–2015 and then again at the Jansky Lab at the GBT in January and February 2016 before being installed on the telescope on March 9, 2016. In the lab, the *Argus* array demonstrated an average receiver temperature of 39–65 K, which should translate to system temperatures of 100–255 K (125–488 K) when observing at an elevation of 90° (30°).

This chapter is organized as follows. Laboratory measurements of the *Argus* receiver are presented in §5.1. Preliminary calculations for the optimal On-The-Fly (OTF) mapping configurations are given in §5.2. The plan for calibrating mapping observations is discussed in §5.3. A summary of some of the troubleshooting that was performed during *Argus* integration and testing is given in §5.4. The details of the instrument commissioning at the GBT are provided in §5.5. Previous sections have tackled the science objectives (§1.2) and the instrument specifications required to achieve this science (§2.4) and can be referenced for additional details.

5.1 Receiver Characterization in Lab

The *Argus* receivers were characterized in the Stanford lab and the Jansky Lab at the GBT prior to deployment. The instrument performance needed to meet the specifications that were laid out in §2.4. A summary of the specifications that were verified via laboratory measurements is provided in Table 5.1.

Table 5.1: A table of the specifications for the *Argus* receiver that were measured in the lab along with the relevant section. These specifications are a subset of the design specifications presented in §2.4.

Test	Specification	Section
Receiver Temperature (T_{Rx})	<60 K	§5.1.1
Dynamic Range	>8 dB linear at $T_A = 300$ K	§5.1.3
IF Power	>-5 dB	§5.1.4
Passband Slope	<10 dB	§5.1.5
Spectroscopic Allan Time (τ_A)	30 s	§5.1.6
Image Rejection Ratio (<i>IRR</i>)	>13 dB	§5.1.7

5.1.1 Receiver Temperature

The noise temperatures of the *Argus* receivers were characterized through the standard Y-factor measurement (Appendix A). A photograph of the test setup for these measurements is depicted in Figure 5.1 and the corresponding schematic is shown in Figure C.1. The hot load is a piece of microwave absorber¹ attached to an automated chopper wheel. When the chopper wheel is in the OFF position the receiver sees the cold load, which is a different piece of microwave absorber² placed in a bath of liquid nitrogen at 77 K. The liquid nitrogen is kept in a styrofoam box, which is transparent in the millimeter-wave regime. This allows for the receiver to be kept in an upward position looking through the box, which is logistically easier than pointing the receiver

¹Cuming Microwave C-RAM FAC

²Eccosorb CV

downward into a cold load on the floor. The box was lined with a plastic sheet because many types of styrofoam boxes were observed to be permeable to liquid nitrogen.

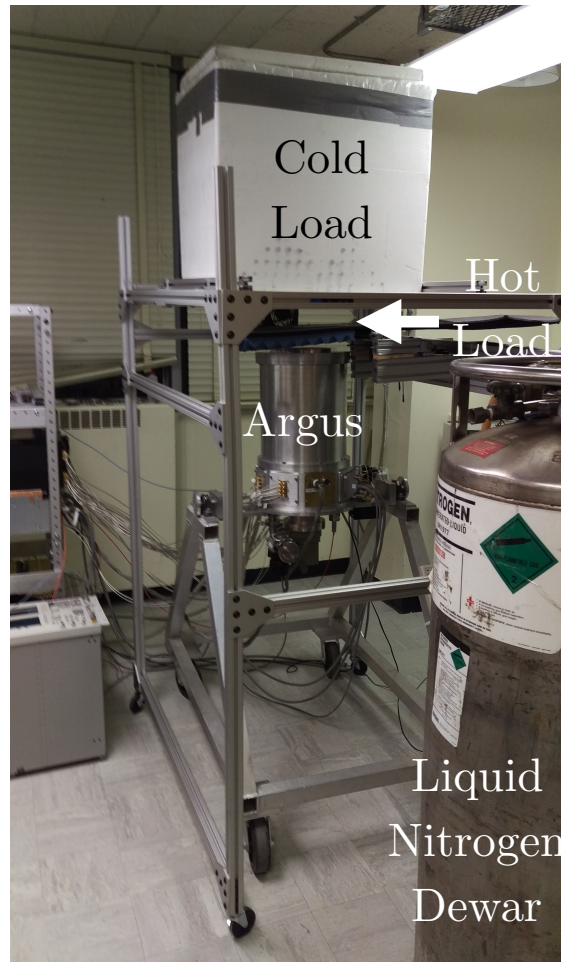


Figure 5.1: A photograph of the test setup for measuring the receiver noise temperature. The white styrofoam box contains an absorber that is immersed in a liquid nitrogen bath at 77 K, which together comprise the cold load. A piece of room temperature absorber is moved over the window (and below the styrofoam box) by a stepper motor to provide the hot load.

The noise temperature results for all 16 of the *Argus* pixels are shown in Figure 5.2. The average pixel has a receiver temperature that varies between 39–65 K across the RF passband. The receiver temperature of the system narrowly misses the specification of 60 K at the lower end of the operating bandwidth due to excess noise from the

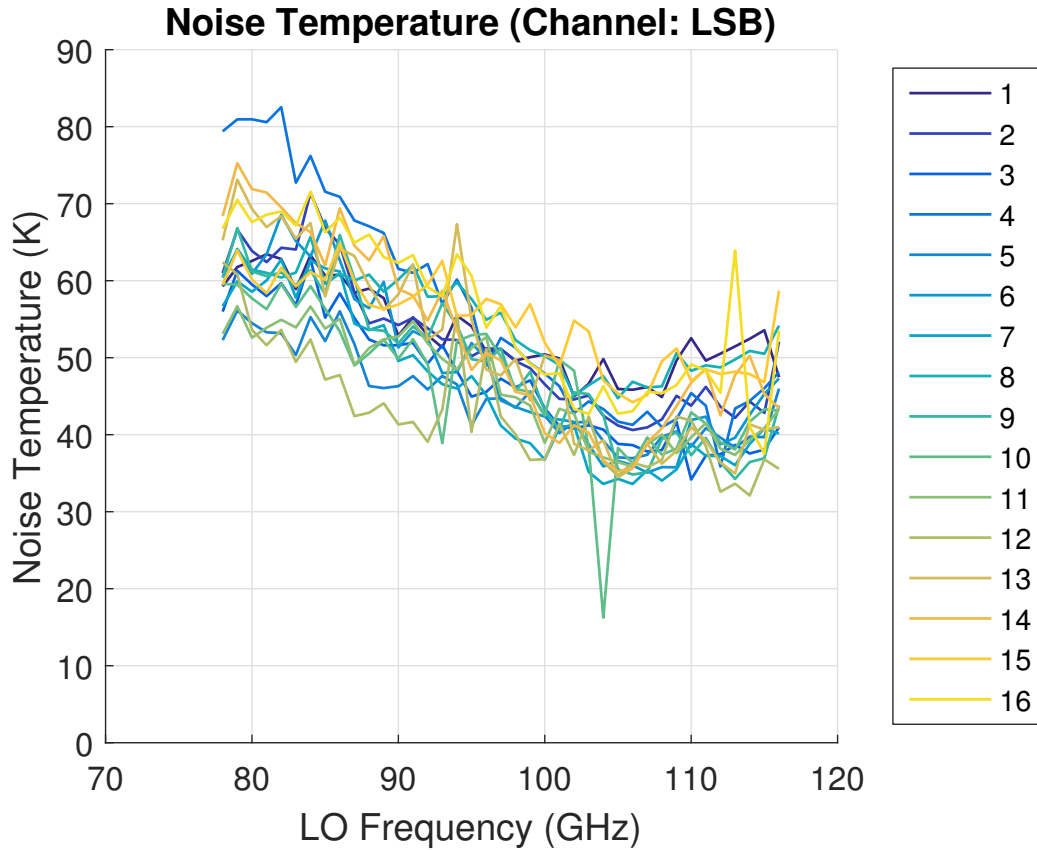


Figure 5.2: The receiver temperature for all 16 *Argus* pixels as measured in the lab. The noise temperature for an average receiver is 39–65 K and meets the specification of 60 K at all but the lowest frequencies in the *Argus* passband.

miniaturized receiver modules at those frequencies (see Figure 3.11); however, the performance is well within the specification at the frequencies of the four spectral lines, HCN & HCO⁺ and C¹⁸O & ¹³CO (see §1.2), that were a focus of the *Argus* characterizations and fine-tunings.

5.1.2 Expected System Temperature

The system temperature is the effective noise temperature of the receiver together with the telescope and the atmosphere. The atmosphere plays a particularly significant role in determining the system temperature because it both attenuates the incoming

signal and emits thermal radiation. The system temperature, T_{sys} , is given by

$$T_{sys} = (T_{rx} + T_{atm} + T_{spill}) e^{\tau/\sin(z)} + T_{CMB} - T_{atm} \quad (5.1)$$

where T_{rx} is the receiver temperature, T_{atm} is the effective physical temperature of the atmosphere, T_{spill} is the noise contribution from spillover pickup from the telescope, T_{CMB} is the noise from the cosmic microwave background, τ is the atmospheric opacity, and z is the elevation of the observation. In practice the spillover temperature can be calculated from the spillover efficiency and is around 3 K at the GBT. The temperature of the cosmic microwave background is known to be approximately 2.725 K.

The expected system temperature for *Argus* was calculated and is plotted in Figure 5.3. The receiver noise temperature T_{rx} is shown in Figure 5.2, the calculated spillover efficiency that is used to find T_{spill} is shown in §B.2, typical values for the atmospheric opacity were obtained from the GBT’s Dynamic Scheduling System calculator³, T_{atm} was assumed to be 273 K, and el was taken to be either 90° or 30°. The expected system temperature for an average pixel is 100–255 K (125–488 K) when observing at an elevation of 90° (30°).

5.1.3 Dynamic Range

The dynamic range of *Argus* is the range of input powers over which the system is linear. The dynamic range is potentially limited by the linearity of the *Argus* IF components, which can become saturated at sufficiently high powers. The initial version of the warm IF electronics (§2.5.4) had problems with the final two amplifiers saturating when the receiver was observing a room temperature load. The linearity of these amplifiers was considered in the design but incorrectly. The 1 dB saturation power specifications (*i.e.* P1dB) were given in the amplifier datasheets for a continuous-wave (CW) tone as is standard; however, the *Argus* signals are broadband and noise-like. The difference between a CW voltage signal and a white noise signal of the same power is illustrated in Figure 5.4. Despite having the same power, the peak signals over short timescales are vastly different. The CW signal has a peak voltage that is a factor of

³https://dss.gb.nrao.edu/calculator-ui/war/Calculator_ui.html

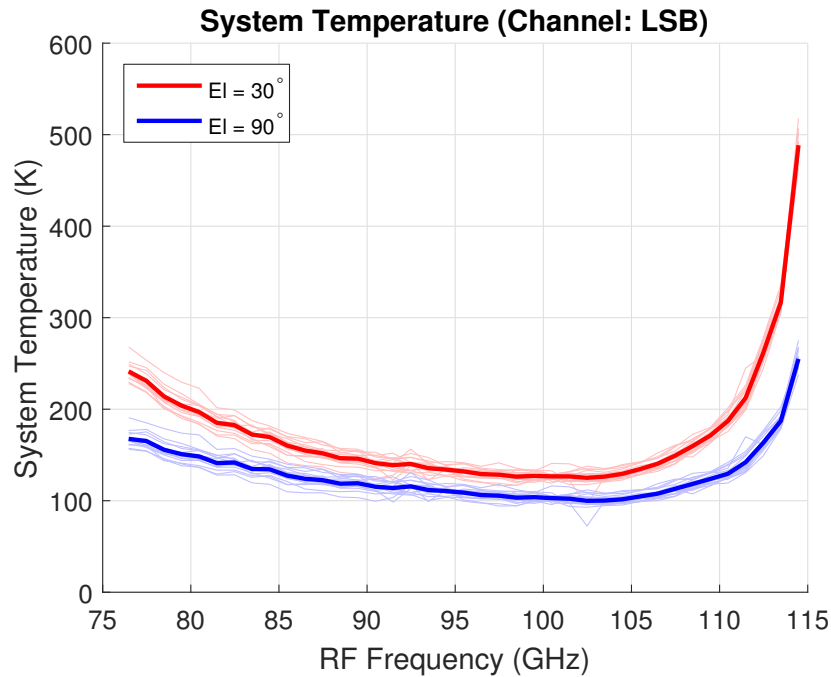


Figure 5.3: The expected system temperature versus frequency for observations at an elevation of 30° and 90° . The light traces show the system temperature for the individual pixels and the dark traces are the average system temperatures.

$\sqrt{2}$ larger than the RMS voltage, while the white noise signal occasionally has peaks that are significantly larger. The amplifiers are able to become saturated over short timescales, which means that broadband noise-like signals lead to saturation at lower power levels than CW signals. Ultimately it was found that additional attenuation was needed beyond what was provided in the initial design. The variable attenuator in the warm IF electronics was of limited use in addressing this problem because it is located before the final amplifier (as shown in the circuit schematic in Figure 2.11) and so unfortunately it is only useful in mitigating the saturation of the final amplifier, but not the penultimate amplifier.

The linearity of the *Argus* warm IF components was checked after the attenuator values were adjusted by inserting a variable attenuator in front of the warm IF components and then comparing the input and output powers for different attenuator settings. The on-board variable attenuator before the final amplifier was kept fixed at 20 dB so that the final amplifier would be safely in its linear regime and only the

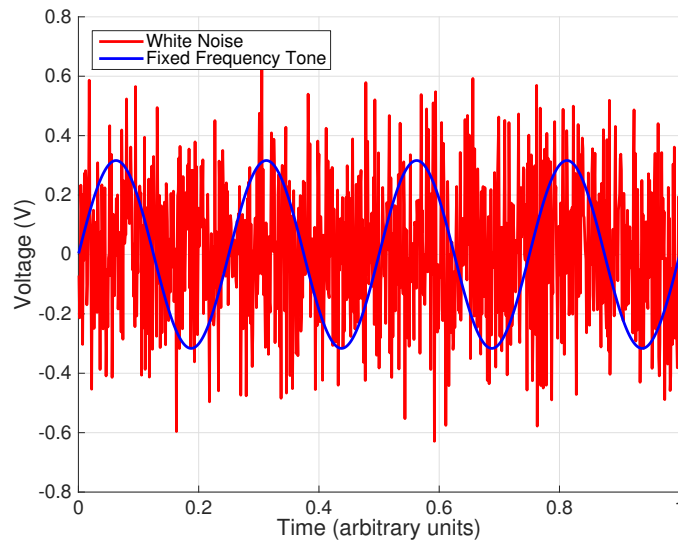


Figure 5.4: A plot of two signals with 0 dBm power: a white noise signal and a continuous-wave tone (*i.e.* a sine wave). A 50Ω impedance is assumed. Despite the fact that both traces have the same average power, the instantaneous power of the white noise trace occasionally experiences brief spikes. The warm IF electronics were originally designed using saturation specifications that were deduced using continuous-wave measurements; however, since *Argus* measures noise-like signals that occasionally have short timescale spikes in power, some of the amplifiers in the warm IF electronics system were driven into saturation. The attenuators in the system were adjusted to account for this issue as shown in §2.5.4.

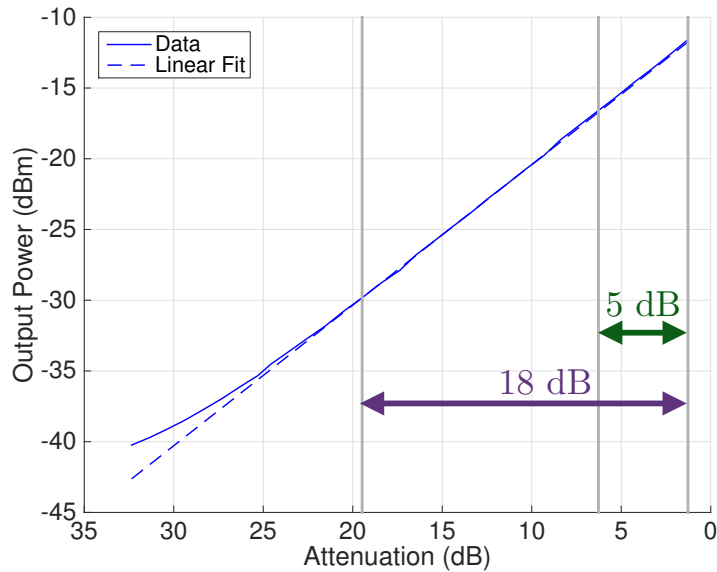


Figure 5.5: The linearity of the warm IF system for pixel 6. A variable attenuator was inserted at the input of the warm IF electronics and varied from 1–32 dB. The IF system is linear over an 18 dB dynamic range, which meets the specification of 5 dB. At the highest attenuation levels the noise temperature of the warm IF components leads to a deviation from linearity.

penultimate amplifier might saturate. The measurement results for a representative pixel are presented in Figure 5.5, which shows no evidence of saturation over a dynamic range of 18 dB. All deviations from linearity within that range are <0.2 dB and can be attributed to measurement error. The input power received at the warm IF electronics box from the cryogenic focal plane is frequency dependent; the frequency with the highest power for a given pixel was used in these measurements to ensure that the warm IF channels were operating in the linear regime across all frequencies. Higher output powers can be achieved by lowering the attenuation of the variable attenuator (§5.1.4).

5.1.4 IF Power

Half of the *Argus* IF channels have a strict output power requirement for interfacing with the GBT electronics. The IF channels fall into two categories: those that use

Argus-dedicated optical links (pixels 1–8) and those that connect to the GBT IF rack (pixels 9–16). The eight *Argus*-dedicated IF fiber links require \sim -5 dBm output power going into the optical transmitters⁴⁵. On the other hand, the other eight pixels are amplified in a GBT IF converter module that accepts a wide range of input powers before being launched onto fiber.

Achieving adequate power at the warm IF electronics output was not straightforward because of the increased attenuation that was added to ensure linearity (§5.1.3). The output IF power was maximized by varying the attenuation of the variable attenuator before the final amplifier and choosing the lowest attenuation value where that amplifier was still in its linear regime. The resulting power levels for each receiver are plotted in Figure 5.6. The IF powers were measured with a spectrum analyzer. The spectra were integrated from 10 MHz to 6 GHz since the \sim -5 dBm output power specification is for the total IF power. About 75% of the measured power was inside the 0.9–2.15 GHz *Argus* IF band. The power levels were adjusted using the variable attenuator on the warm IF electronics boards. The attenuator levels for pixels 1–8 were adjusted to be as low as possible while maintaining linearity, while for pixels 9–16 the attenuators were set so that the IF power was -25 dBm when the receiver was observing a room temperature load.

5.1.5 Passband Slope

The IF passbands for the *Argus* receivers have a significant amount of spectral structure. The IF spectra were measured for each pixel with a spectrum analyzer while the receivers were observing a room temperature load. A typical spectrum is shown in Figure 5.7. There are two significant features. The first is a \sim 1.2 GHz sinusoid that originate from LO standing waves on the multilayer routing boards (see Figure 4.15). The LO noise from the synthesizer, power amplifiers, and frequency multipliers is downconverted into the IF; in this way the standing waves are imprinted onto the

⁴Ortel 3530 Transmitter

⁵The desired power level for the optical transmitters is actually 0 dBm according to the datasheet; however, laboratory measurements showed no degradation in the system noise temperature when using a -5 dBm power level.

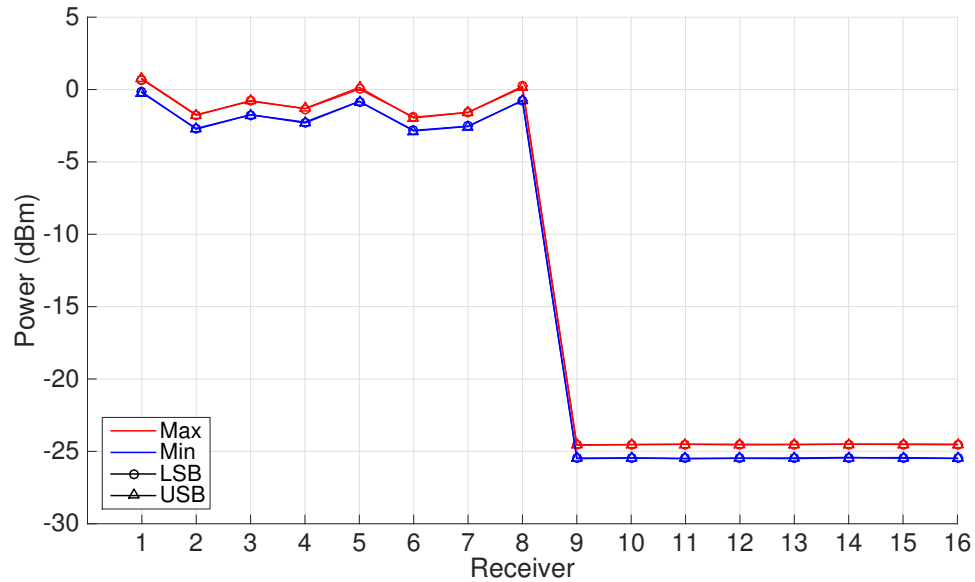


Figure 5.6: The IF power of each of the 16 pixels while observing a room temperature load. Pixels 1–8 were adjusted so that the IF power was as high as possible without saturation in the IF chain. The specification is -5 dBm, but higher powers are desirable. Pixels 9–16 to not have a strict specification and were set to ~ -25 dBm

IF. This phenomenon also affected the receiver noise temperatures and is discussed in more detail in §5.4.3. The second feature that is seen in all pixels is a spectral slope where the output power becomes greater with increasing IF. There is ~ 2 dB of linear slope, which is due to the equalizer in the warm IF electronics (§2.5.4); the equalizer overcompensates for ohmic loss in the system. This slope could be improved by adjusting the equalizer, which would also have the effect of increasing the IF power. The peak-to-peak power for each pixel is shown in Figure 5.8. All of the pixels meet the 10 dB specification. Pixel 12 has a large slope at one particular LO frequency, but is otherwise consistent with all of the other pixels. Even with this outlier data point, pixel 12 meets the slope specification.

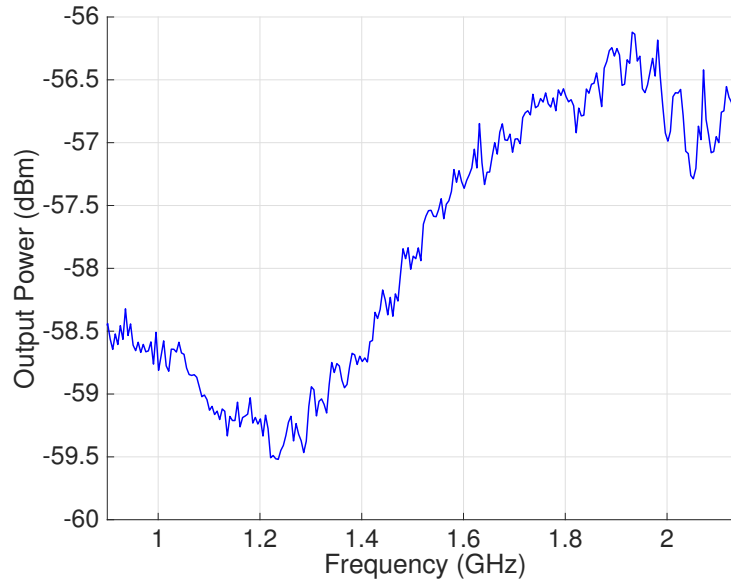


Figure 5.7: A typical IF spectrum as measured with a spectrum analyzer with 5 MHz resolution bandwidth. There are two important features. The first is a sinusoidal component, which has a trough at ~ 1.2 GHz and peak at ~ 1.9 GHz. This feature is from LO-to-IF leakage; the LO noise is downconverted into the IF. The LO lines on the multilayer routing board have ~ 1.2 GHz standing waves from connector mismatch (see Figure 4.15), which is the source of the sinusoids seen in the IF spectrum. This phenomenon increased the receiver noise temperature as discussed in §5.4.3. This problem was mitigated by filtering the LO signal, but yet the effect of LO noise can still be seen in the IF spectrum. The second feature is a rising slope of ~ 2 dB across the *Argus* band of 0.90–2.15 GHz. This slope is seen in all pixels and can be attributed to the equalizer in the warm IF electronics (§2.5.4), which overcompensates for ohmic losses in the system. The slope could be flattened and the IF power levels could be increased by adjusting the equalizer.

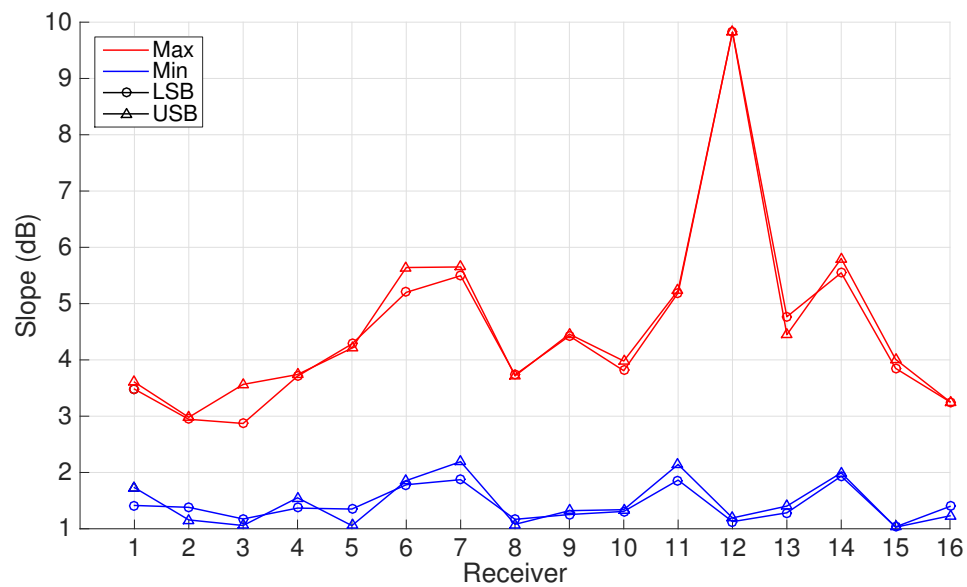


Figure 5.8: The peak-to-peak power in the IF spectrum for all 16 pixels. The large peak-to-peak power for pixel 12 was observed at just one of the LO frequencies over which *Argus* was characterized. The IF spectra for this pixel were otherwise unremarkable. Despite this data point, all pixels meet the 10 dB specification for IF slope.

5.1.6 Stability

Two methods were used to quantify the stability of the *Argus* system: Allan variance measurements and waterfall measurements. Both of these measurements were performed in the lab with the receivers observing a room temperature load. Ultimately both procedures will be repeated with the receivers observing the cold sky. The most significant difference between measuring in lab and on the sky is the white noise level. The room temperature absorber that was used in all of the laboratory measurements results in higher white noise levels than observations on the cold sky and can mask instrument instabilities on short to intermediate timescales. On the other hand, the laboratory Allan variance measurements had a large bandwidth (200 MHz); both the channel size and spectral line widths of observed lines will have smaller bandwidths, which will lead to higher white noise levels when observing on the sky. Therefore, compared to the laboratory measurements, it will be possible to integrate for longer periods of time on the sky before the measurement uncertainty becomes dominated by instrument instabilities. Another difference between the laboratory measurements and observations on the telescope is that the atmospheric instabilities can contribute to the total system stability when the cold sky is being observed; however, this atmospheric contribution is expected to be subdominant to the instrument instabilities for spectroscopic measurements (see *e.g.* [59]).

Allan Variance Measurements

Allan variance measurements are a common way to characterize the stability of radiometer systems [60, 61]. The concept of Allan variance was originally conceived in the context of atomic frequency standards [62], which illustrates that this method is sufficiently general that it can be applied to any type of instrument; however, the focus here is to present the mechanics for understanding the stability of a spectrometer like *Argus*. Given a signal $s(t)$ we consider the integrated signal over time τ :

$$s(\tau) = \int_0^\tau s(t)dt \quad (5.2)$$

The Allan variance of the signal is then defined by [62]:

$$\sigma_A^2(\tau) \equiv \sigma^2(\tau)/2 = (\langle s(\tau)^2 \rangle - \langle s(\tau) \rangle^2)/2 \quad (5.3)$$

The observations under consideration are noise-dominated, which permits the assumption that $\langle s(\tau) \rangle = 0$. Equation 5.3 then simplifies to

$$\sigma_A^2(\tau) = \frac{1}{2} \langle s(\tau)^2 \rangle \quad (5.4)$$

Heretofore it has been assumed that the data are a continuous function, $s(t)$, with infinite time resolution. In practice though the data are collected in a discrete number of integrations. For the case of N integrations the Allan variance becomes:

$$\sigma_A^2(\tau) = \frac{1}{2(N-1)} \sum_{n=1}^N (s(n) - \langle s \rangle)^2 \quad (5.5)$$

To better understand the stability of an actual instrument it is useful to consider specific types of noise. Noise spectra can typically be decomposed into power law contributions:

$$S(f) \propto f^{-\alpha} \quad (5.6)$$

In particular, there is in general a white noise term ($\alpha = 0$), a $1/f$ noise term ($\alpha = 1$) that is common to electronic components, and a low frequency drift term ($\alpha = 2 - 3$). The corresponding Allan variance for a particular power law contribution is

$$\sigma_A^2(\tau) \propto \tau^{\alpha-1} \quad (5.7)$$

For white noise the Allan variance is inversely proportional to the integration time, as would be expected from the radiometer equation (Equation 2.6).

The measured total power Allan variance for *Argus* was measured at two frequency ranges in the IF band. The setup, whose schematic is shown in Figure C.2, includes a two-channel filter bank with filter bandwidths of 980–1150 MHz and 1790–1920 MHz.

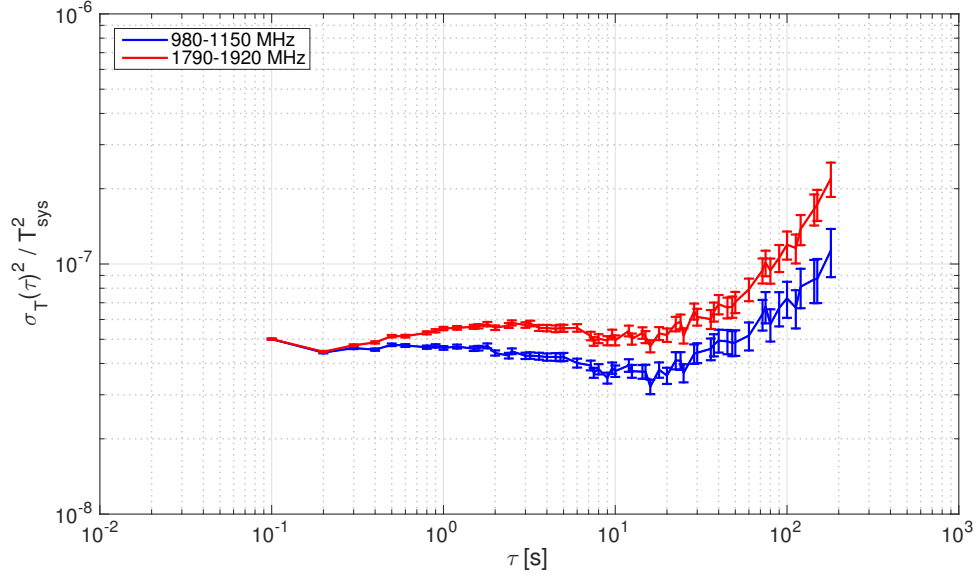


Figure 5.9: The total power Allan variance for pixel 3. The RF frequency was set to 85.5 GHz with the LO configured for a lower sideband configuration.

The IF signal is sent to a power meter⁶ and the power time series was continuously sampled and binned into 0.1 s bins. The resulting data are plotted in Figure 5.9. The $1/f$ component ($\alpha = 1$), which appears as a constant in these plots, is the dominant contribution. Importantly, there is a strong correlation in noise between the two channels, which is leveraged in the following analyses.

In spectroscopic observations it is typically not the total power stability that matters but the stability of a spectral line relative to the continuum. The spectroscopic Allan variance measures the stability of frequency channels relative to each other. Measuring the spectroscopic Allan variance gives a higher Allan time because the low frequency drift tends to be highly correlated across the channels.

To measure the spectroscopic Allan variance one starts with the normalized quantity

$$s(t) = \frac{1}{\sqrt{2}} \left[\left(\frac{x_i(t)}{\langle x \rangle} - \frac{y_i(t)}{\langle y \rangle} \right) + 1 \right] \left(\frac{\langle x \rangle + \langle y \rangle}{2} \right) \quad (5.8)$$

⁶An Agilent E4418B power meter and Agilent E4412A power sensor.

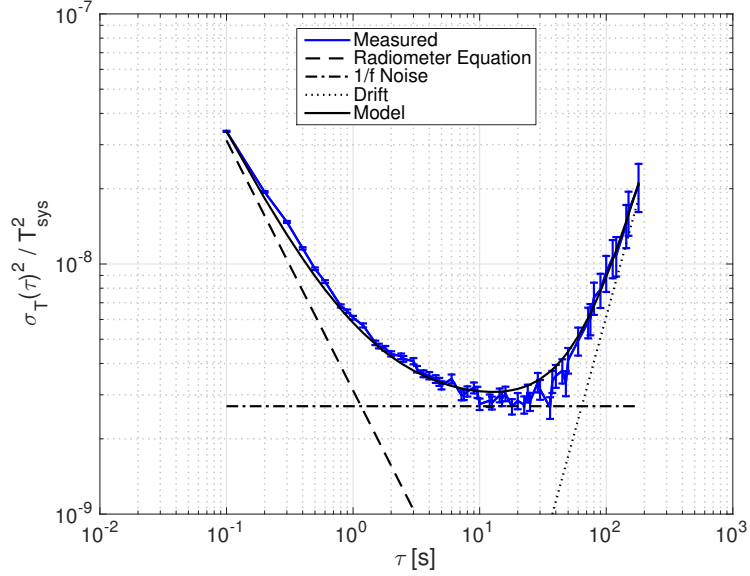


Figure 5.10: The spectroscopic Allan variance for pixel 3. The RF frequency was set to 85.5 GHz with the LO configured for a lower sideband configuration. The noise is fit to a model with three components: radiometric noise, $1/f$ noise, and drift.

where $x(t)$ and $y(t)$ are the signals in two distinct frequency channels. The spectroscopic Allan variance can then be found by analyzing this normalized quantity with Equation 5.5.

The spectroscopic Allan variance was calculated using the same data that was used in Figure 5.9 and is plotted in Figure 5.10. The three power law contributions were fit to the data and are shown in the plot. At small integration times, the Allan variance is dominated by white noise, which improves with integration time via the radiometer equation (Equation 2.6). At longer integration times the curve flattens out as $1/f$ fluctuations dominate. Finally, as the integration time increases even further the low frequency drift takes over. The noise parameters from the modeled fit to the laboratory data are shown in Table 5.2. The minimum in the Allan variance plots is known as the Allan time, τ_A . The Allan time is critical for finding the optimal switching speeds and scan lengths for an observation, a topic which is discussed in detail in §5.2.

The spectroscopic Allan time for observations on the sky will be different than the value measured in the laboratory (Table 5.2) because of the different levels of

Table 5.2: The noise parameters extracted from the spectroscopic Allan variance data depicted in Figure 5.10. The $1/f$ contribution to the Allan variance and the drift power law index α are expected to be the same on the sky as in the laboratory. The Allan time, on the other hand, depends on the white noise level, which depends on the measurement configuration.

Parameter	Value
Allan Time (τ_A)	12.7 s
$1/f$ Contribution to Allan Variance (σ_A^2/T_{sys}^2)	2.7×10^{-9}
α , Drift Power Law Index	2.85

white noise being measured. There are two factors that contribute to this difference: the effective temperature of the object being observed and the bandwidth of the measurement. In the laboratory measurements the receivers see a room temperature absorber, which emits more thermal noise than the cold sky. The bandwidth of the laboratory measurements was also relatively wide (~ 200 MHz), which lowers the measured white noise per Equation 2.6. The level of white noise when observing the cold sky, σ'_T , is related to the white noise observed in the lab, σ_T , by

$$\frac{\sigma'_T}{\sigma_T} = \frac{T'_{sys}}{T_{Rx} + T_{Room}} \left(\frac{\Delta\nu}{\Delta\nu'} \right)^{1/2} \quad (5.9)$$

where τ_A is the spectroscopic Allan time of the laboratory measurements, T'_{sys} is the expected system temperature of the instrument (§5.1.2), T_{Rx} is the receiver noise temperature (§5.1.2), T_{Room} is the ambient room temperature, $\Delta\nu$ is the bandwidth of the laboratory measurements, and $\Delta\nu'$ is the relevant observational bandwidth (*i.e.* either the channel bandwidth or the spectral line width if the channels are binned). The noise model from Figure 5.10 was modified to account for the change in white noise that is expected for on-the-sky observations using Equation 5.9. The expected Allan variance curves for three different observational bandwidths are shown in Figure 5.11. Two of the bandwidths considered correspond to the channel widths of VEGAS modes: 1,465 kHz⁷ and 92 kHz⁸. The third case, 5,000 kHz, is the line width of a 17 km/s

⁷VEGAS Mode 1 (H1K/HBW)

⁸VEGAS Mode 2 (H16K/HBW)

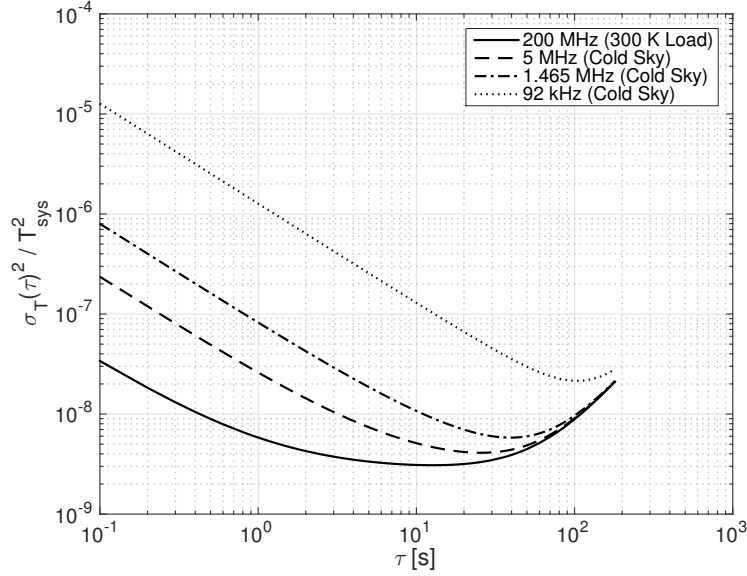


Figure 5.11: The expected spectroscopic Allan variance for observations on the cold sky. The radiometric component of the Allan variance is dependent on the bandwidth of the observation. Considered here are channel width for two VEGAS configurations (92 kHz and 1,465 kHz) and the spectral line width of a 17 km/s HCN line (5,000 kHz), the latter of which could be binned to form an image.

HCN line, which might be binned together when creating a map.

The expected spectroscopic Allan time for observations on the sky, τ'_A , can be found approximately through

$$\tau'_A = \tau_A \left(\frac{T_{sys}^{\prime 2}}{(T_{Rx} + T_{Room})^2} \frac{\Delta\nu}{\Delta\nu'} \right)^{1/\alpha} \quad (5.10)$$

where α is the power law index of the drift ($\alpha = 2.85$ from Table 5.2). This equation simply gives the minimum of the model Allan variance traces in Figure 5.11. The spectroscopic Allan times for the three configurations under consideration are given in Table 5.3.

The Allan time influences the observation strategy. It is recommended to keep the integration time for a receiver below the Allan time for maximal observing efficiency. Integrations longer than the Allan time give baseline noise in each measurement bin that is higher than the radiometer equation contribution and also time variable.

Table 5.3: The expected Allan times for observations on the sky. These are simply the minima of the spectroscopic Allan variance models that are plotted in Figure 5.11. Alternatively, Equation 5.10 can be used to predict the Allan time of an arbitrary observational configuration.

Bandwidth (kHz)	Expected Allan Time (τ_A)
92	103.8 s
1,465	39.4 s
5,000	25.7 s

This in turn leads to unnecessary errors when performing baseline subtraction. The calibration procedure is also informed by the Allan time as shorter Allan times demand more frequent calibration. Scan strategies and calibration are covered in more detail in §5.2.

Waterfall Measurements

Another common way to analyze the stability of a system is through waterfall plots. The *Argus* IF channels were connected to a custom single-channel spectrometer in the Jansky Laboratory at the GBT and a room temperature load was presented at the RF input to the receivers. Repeated 60 s integrations were performed for each pixel over the course of 30 minutes. The waterfall plot for a typical pixel is shown in Figure 5.12. Each spectrum is normalized by the the initial spectrum and offset from the previous spectrum in the plot by a fixed amount. The principle advantage of this characterization method is that it simulates the conditions of an actual observation on the telescope. The waterfall plots were qualitatively checked for spectral features that may have appeared as time elapsed. In general the normalized spectra remained relatively flat, with only very broad spectral features that could easily be removed in an observation via baseline subtraction⁹; however, as it was noted above, the room temperature load generates more white noise than the cold sky; some of the instrument instabilities on short and intermediate timescales are therefore likely masked in the lab, but will be relevant on the telescope. Nevertheless, the results shown in Figure 5.12 were an important demonstration of the instrument stability.

⁹The feature at 1.2 GHz is a measurement artifact from a clock in the spectrometer circuit.

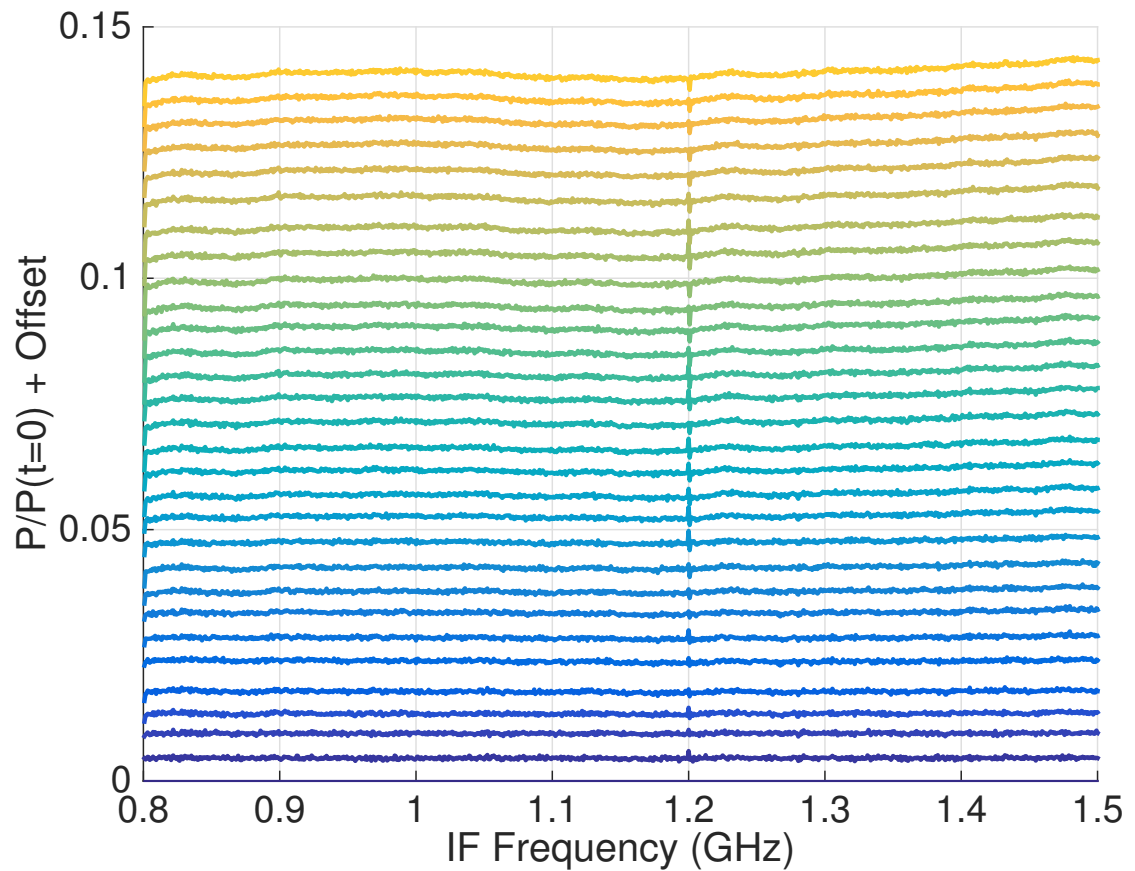


Figure 5.12: A typical waterfall plot showing 30 IF spectra that are each integrated for 60 s and normalized to the first integration. The bottom trace is the first integration and each subsequent measurement is plotted above the previous one with an offset. The topmost trace therefore shows the stability of the passband over 30 minutes. The passband remained relatively flat over 30 minutes, which was a qualitative indication that *Argus* is stable enough to do useful science. The observed spectral features in this measurement would be straightforward to remove in an observation with baseline subtraction.

5.1.7 Image Rejection

Argus utilizes an I/Q downconversion scheme (§2.2.2). A double-sideband RF signal is downconverted by two mixers that are out of phase. The mixers and their IF signals are denoted by I and Q for in-phase and quadrature-phase, respectively. The output from each mixer is given by Equations 5.11 and 5.12:

$$v_I(t) = A_{I,usb}e^{i(\nu_{usb}-\nu_{LO})t} + A_{I,lsb}e^{i(\nu_{lsb}-\nu_{LO})t} \quad (5.11)$$

$$v_Q(t) = A_{Q,usb}e^{i[(\nu_{usb}-\nu_{LO})t+\phi]} + A_{Q,lsb}e^{i[(\nu_{lsb}-\nu_{LO})t-\phi]} \quad (5.12)$$

where A_I (A_Q) is the amplitude of the in-phase (quadrature-phase) IF signal, ν_u (ν_l) is the RF frequency of the upper (lower) sideband, ν_{LO} is the effective LO frequency¹⁰, and ϕ is the phase difference between the two mixers. In an ideal system $\phi = 90^\circ$ and $A_I = A_Q$, however, in practice there are inevitably phase and amplitude imbalances that are frequency dependent.

The I and Q signals can be separated into their upper and lower sideband components by combining them in a quadrature hybrid or doing an analogous procedure in software. Equations 5.11 and 5.12 can be used to solve for the output signals from the hybrid:

$$\begin{aligned} v_{usb} &= v_I(t) + v_Q(t)e^{-i\psi} \\ &= (A_{I,usb} + A_{Q,usb}e^{i(\phi-\psi)})e^{i(\nu_{usb}-\nu_{LO})t} \\ &\quad + (A_{I,lsb} + A_{Q,lsb}e^{-i(\phi+\psi)})e^{i(\nu_{lsb}-\nu_{LO})t} \end{aligned} \quad (5.13)$$

$$\begin{aligned} v_{lsb} &= v_I(t) + v_Q(t)e^{i\psi} \\ &= (A_{I,usb} + A_{Q,usb}e^{i(\phi+\psi)})e^{i(\nu_{usb}-\nu_{LO})t} \\ &\quad + (A_{I,lsb} + A_{Q,lsb}e^{-i(\phi-\psi)})e^{i(\nu_{lsb}-\nu_{LO})t} \end{aligned} \quad (5.14)$$

where ψ is the phase difference between the quadrature hybrid ports and should ideally be 90° .

If it is assumed that the mixer and quadrature hybrid are perfect (*i.e.* $\phi = 90^\circ$,

¹⁰For *Argus* the effective LO frequency is twice the actual LO frequency since the mixers are sub-harmonically pumped.

$\psi = 90^\circ$ and $A_I = A_Q = A$), then Equations 5.13 and 5.14 reduced to Equations 5.13 and 5.14, which shows that the upper and lower sidebands separate completely.:

$$v_{usb} = 2Ae^{i(\nu_{usb}-\nu_{LO})t} \quad (5.15)$$

$$v_{lsb} = 2Ae^{i(\nu_{lsb}-\nu_{LO})t} \quad (5.16)$$

In reality though, the sideband separation will be imperfect due to both the hybrid and the mixer. The contamination of the desired sideband, or signal, by the undesired sideband, known as the image, can be quantified by the image rejection ratio or *IRR*:

$$\begin{aligned} IRR &= \left| \frac{v_{lsb}}{v_{usb}} \right|^2 \\ &= \left| \frac{(A_{I,usb} + A_{Q,usb}e^{i(\phi+\psi)})e^{i(\nu_{usb}-\nu_{LO})t}}{(A_{I,usb} + A_{Q,usb}e^{i(\phi-\psi)})e^{i(\nu_{usb}-\nu_{LO})t}} \right|^2 \\ &= \left| \frac{A_{I,usb} + A_{Q,usb}e^{i(\phi+\psi)}}{A_{I,usb} + A_{Q,usb}e^{i(\phi-\psi)}} \right|^2 \end{aligned} \quad (5.17)$$

It is useful to make the following parameter substitutions:

$$A_{I,usb} = A_{Q,usb}(1 + \epsilon) \quad (5.18)$$

$$\phi + \psi = \pi - \chi \quad (5.19)$$

where ϵ and χ are the amplitude and phase imbalances, respectively. Applying these

substitutions yields

$$\begin{aligned}
IRR &\approx \left| \frac{A_{Q,usb}(1 + \epsilon) + A_{Q,usb}e^{i(\pi-\chi)}}{2A_{Q,usb}} \right|^2 \\
&\approx \left| \frac{(1 + \epsilon) + e^{i(\pi-\chi)}}{2} \right|^2 \\
&= \left| \frac{(1 + \epsilon) - e^{-i\chi}}{2} \right|^2 \\
&\approx \left| \frac{(1 + \epsilon) - (1 - \chi)}{2} \right|^2 \\
&= \left| \frac{\epsilon + \chi}{2} \right|^2 \\
&\approx \frac{(\epsilon^2 + \chi^2 + 2\epsilon\chi)}{4}
\end{aligned} \tag{5.20}$$

If it is further assumed that the amplitude and phase imbalances contribute equally to the IRR ($\epsilon = \chi = \delta$), then the IRR becomes

$$IRR = \delta^2 \tag{5.21}$$

Table 5.4: Specifications for the amplitude and phase imbalances that would be required to achieve a particular IRR target. The first number given assumes that the amplitude and phase imbalances contribute equally to the IRR , while the value in parentheses assumes that just one of these factors is contributing to the IRR and the other one is negligibly small.

IRR Target	δ	Amplitude Balance (A_I/A_Q)	Phase Balance (χ)
10 dB	0.32 (0.63)	2.4 dB (4.3 dB)	18.1° (36.2°)
13 dB	0.22 (0.45)	1.8 dB (3.2 dB)	12.8° (25.7°)
15 dB	0.18 (0.36)	1.4 dB (2.6 dB)	10.2° (20.4°)
20 dB	0.10 (0.20)	0.8 dB (1.6 dB)	5.7° (11.5°)

The image rejection ratio was measured in lab using the measurement setup pictured in Figure 5.13. The corresponding schematic is depicted in Figure C.3. A continuous-wave signal was transmitted to the input of all of the receivers and then

a spectrum analyzer¹¹ was used to measure the signal and image in the IF. The data from these measurements are presented in Figure 5.14. The majority of data points meet the 10 dB specification. The few data points that missed specifications were permitted after repeated optimizations failed to improve the performance. The affected LO frequencies will not be used for observing HCN & HCO⁺ and C¹⁸O & ¹³CO for which *Argus* was optimized; however, If these LO frequencies are used, the instrument will still yield scientifically useful data.

5.2 On-The-Fly Mapping

On-The-Fly (OTF) mapping is an efficient observing technique for generating images of relatively large areas of sky [63]. Instead of observing at a number of discrete positions on the sky, in OTF mapping the telescope continuously scans across the source. There are two major advantages to the OTF approach: it avoids the significant overhead times associated with re-pointing the telescope and the images can be made more quickly, which minimizes the effect of instabilities from the instrument or the atmosphere.

The OTF imaging process involves taking a series of source and reference observations. The data taken as the telescope slews across the source will be referred to as the ON configuration. The source data acquisition is periodically interrupted to measure an area of blank sky, which will be called the OFF configuration, that serves as a calibration spectrum used to correct for drifts in the system. A sequence of ON integrations together with a single OFF measurement is called a scan; each observation is made up of a series of scans. The total integration time for a scan is $t_{scan} = Nt_{ON} + t_{OFF}$ where N is the number of positions measured on source between two OFF measurements, t_{ON} is the integration time for each on source sky position, and t_{OFF} is the integration time for each calibration measurement. The radiometer

¹¹Agilent E4446A

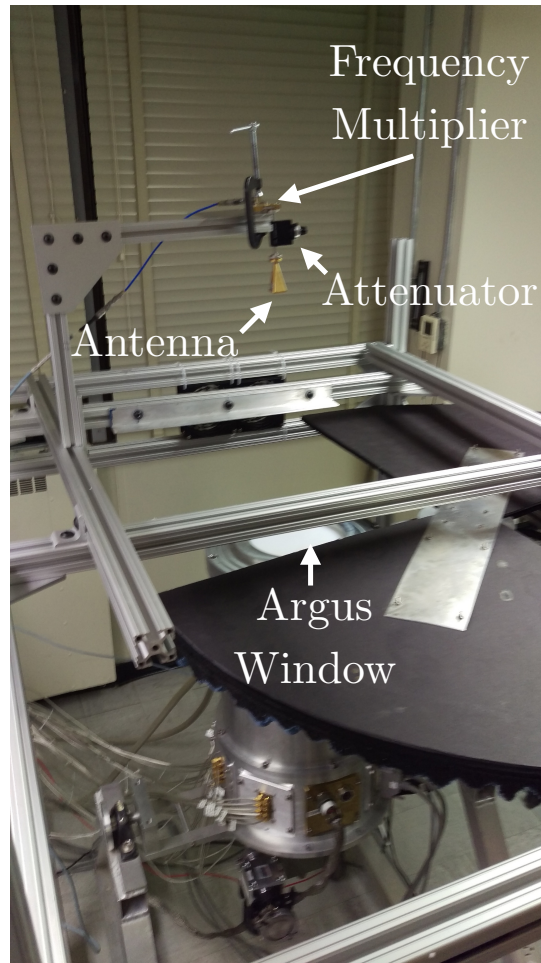


Figure 5.13: A photograph of the test setup for measuring the image rejection ratio. A fixed frequency signal is injected into the input of the receivers via a synthesizer, frequency multipliers, a variable attenuator, and a feedhorn antenna. The signal and image are then measured at the IF output with a spectrum analyzer.

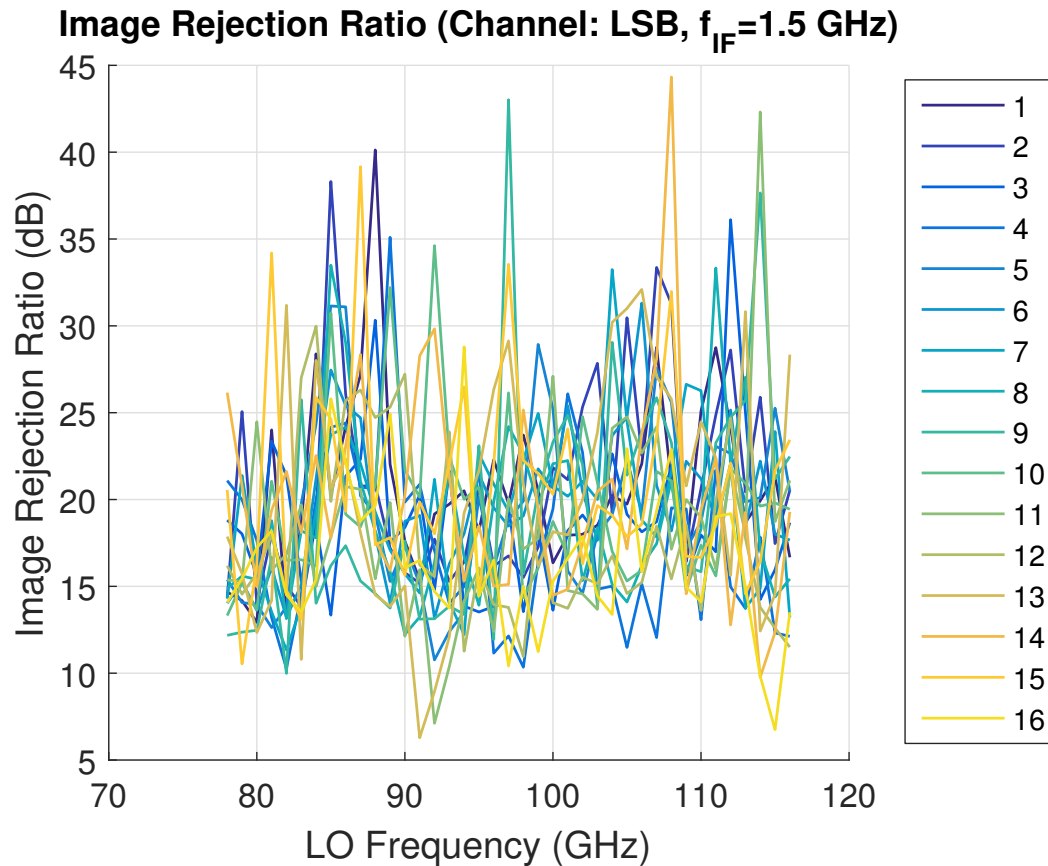


Figure 5.14: The image rejection data for all 16 *Argus* pixels. The majority of pixels and frequencies meet the 10 dB specification. The handful of data points below specification could not be improved after repeated optimizations. These data were eventually deemed good enough to do useful science despite not meeting the specification in part because these LO frequencies will not be used for observing HCN & HCO⁺ and C¹⁸O & ¹³CO for which *Argus* was optimized.

equation (Equation 2.6) is modified to give the sensitivity, σ , of a single integration as

$$\sigma = \frac{T_{sys}}{\eta\sqrt{\Delta\nu}} \left[\frac{1}{t_{ON}} + \frac{1}{t_{OFF}} \right]^{1/2} \quad (5.22)$$

where η is the observing efficiency.

The optimal sensitivity for a fixed scan time, assuming no dead time between ON and OFF scans, is therefore achieved when the following function is minimized:

$$\begin{aligned} f(t_{ON}) &= \frac{1}{t_{ON}} + \frac{1}{t_{OFF}} \\ &= \frac{1}{t_{ON}} + \frac{1}{t_{scan} - Nt_{ON}} \end{aligned} \quad (5.23)$$

The derivative of $f(t_{ON})$ is

$$\begin{aligned} \frac{\partial f}{\partial t_{ON}} &= \frac{\partial}{\partial t_{ON}} \frac{1}{t_{ON}} + \frac{1}{t_{scan} - Nt_{ON}} \\ &= -\frac{1}{t_{ON}^2} + \frac{1}{(t_{scan} - Nt_{ON})^2} \\ &= -\frac{1}{t_{ON}^2} + \frac{N}{t_{OFF}^2} \end{aligned} \quad (5.24)$$

The minimum of $f(t_{ON})$, found by taking $\frac{\partial f}{\partial t_{ON}} = 0$, is achieved with an OFF integration time of $t_{OFF}^{opt} = \sqrt{N}t_{ON}$. The corresponding sensitivity is

$$\sigma^{opt} = \frac{T_{sys}}{\eta\sqrt{\Delta\nu}t_{ON}} \left[1 + \frac{1}{\sqrt{N}} \right]^{1/2} \quad (5.25)$$

In practice there is in fact dead time between ON and OFF configurations and yet Equation 5.2 remains relatively accurate and is commonly used as a rule of thumb for planning observations [64]. Equation 5.2 indicates that longer scans (*i.e.* larger N) lead to better sensitivity. An alternative to OTF mapping would be to use position switching (§5.3.3) where every discrete on-source pointing is associated with an off-source reference observation (*i.e.* $N = 2$). Equation 5.2 illustrates that OTF mapping is potentially much more efficient than such an alternative. A typical scan

might have a total scan time of about 2 minutes with a 0.5 s integration time, which would correspond to $N = 1200$. In this example, Equation 5.2 gives the sensitivity as 1.014 times the sensitivity for an observation where all time is spent on source (Equation 2.6). In principle N could be increased by decreasing the integration time; however, the gain in sensitivity would be small, while the increase in data rate could be substantial. The maximum length of each scan, which could also be leveraged to increase N , is limited by the stability of the instrument, which is discussed in detail in the following paragraphs.

It is possible to suppress the effects of instrument gain fluctuations on an observation with an appropriate observing scheme. One way accomplish this for OTF mapping of extended sources is to scan across the length of the source faster than the time scale of the drifts, which is roughly the Allan time (§5.1.6) [65]. The GBT is limited to slew speeds of $36^\circ/min$ when the temperature is above 17°F and half this speed in $-10 - -17^\circ\text{F}$ conditions [36]. If a $10^\circ \times 10^\circ$ patch of sky were being imaged then a 1 min scan time, for example, would allow the source to be transversed multiple times before the reference observation. It is relevant to note that another way to suppress the effects of instrument or atmospheric instabilities is by periodically switching the state of the observation. If the switching is faster than the Allan time then the on- and off-source measurements can be differenced to remove the drifts. This procedure is discussed for position switching and frequency switching in §5.3.3 and §5.3.4, respectively. Frequency switching could be used in conjunction with OTF mapping.

Since the stability of the system limits the maximum scan length, it is useful to consider the Allan variance of an observation that is the difference between a signal measurement, x_s , and a reference measurement, x_r . The difference signal, d , is

$$d = x_s - x_r \quad (5.26)$$

The spectroscopic Allan variance can be found using Equation 5.5:

$$\sigma_A^2 = (\sigma_s^2 + \sigma_r^2) / 2 - g_{sr} \quad (5.27)$$

where

$$g_{sr} = \langle (x_s - \langle x_s \rangle) (x_r - \langle x_r \rangle) \rangle \quad (5.28)$$

is the correlation function of the datasets. If the signal and reference datasets have the same variance ($\sigma_s^2 = \sigma_r^2 = \sigma^2$), which is likely to be true for astronomical signals that are noise-dominated, then Equation 5.2 becomes

$$\sigma_A^2 = \sigma_r^2 - g_{sr} \quad (5.29)$$

If the signal and reference are correlated over the period of observation, then the Allan variance of the differential signal becomes less than the Allan variance of the raw data; however, for white noise there is no correlation and no improvement in the Allan variance. The switching speed between the signal and reference measurements should therefore be faster than the $1/f$ variations and low frequency drift; however, there is no point in switching too fast because the dead time involved with switching will diminish the observing efficiency.

The optimal observing time for a given number of integrations and dead time in each scan was solved for by [64]. It was assumed that the low frequency drift has a power law (α) of 2–3. The optimum source integration time t_{ON} and reference integration time t_{OFF} were found to be

$$\frac{t_{ON}}{\tau_A} \approx 0.53 \left(\frac{t_d}{\tau_A} \right)^{0.23} \frac{1}{N^{0.69}} \quad (5.30)$$

$$t_{OFF} = \sqrt{N} t_{ON} \quad (5.31)$$

where τ_A is the spectroscopic Allan variance, t_d is the dead time associated with each scan, and N is the number of integrations. When planning an observation an observer can:

1. First determine the maximum bandwidth that will be used when binning channels in the image analysis, as this determines the Allan time, τ_A (§5.1.6).
2. Then choose an integration time, t_{ON} , making sure that the image will be sampled at least 2.5 points per beamwidth [63].

3. Next, Equations 5.30 and 5.31 can be used to solve for the number of integrations per scan and the integration time in the OFF position.
4. Finally, the integration time may need to be iteratively changed to ensure that the scan time is sensible.

In the spectroscopic Allan variance measurements done during commissioning (§5.1.6), a 30 s specification was set. Equation 5.30 can be used to better motivate this criterion. Rearranging Equation 5.30 yields

$$\tau_A \approx \frac{N^{0.90} t_{ON}^{1.30}}{0.44 t_d^{0.30}} \quad (5.32)$$

If it is desired to have a 2 min total scan time (t_{scan}) with an integration time (t_{ON}) of 0.2 s, then the number of integrations per scan (N) is 600. If it is further assumed that the dead time per scan (t_d) is 20 s for the GBT [66] then the required spectroscopic Allan time (τ_A) is 36 s, which is similar to the specification.

5.3 Calibration

Attaining scientific quality images requires careful calibration to account for changes in the atmosphere, the instrument noise and gain and the response of the telescope. There are a number of different calibration procedures that will be useful for *Argus* observations. In general these procedures fall into two categories: reference measurements that help to scale the output signals to meaningful units and/or that reject fluctuations in the instrument or atmosphere and then calibration measurements for the optical performance of the telescope.

There are several useful units that can be used when making astronomical images. Astronomical sources can in general be approximated as black bodies with a spectral radiance, $B_\nu(\nu, T)$, given by the Planck Law:

$$B_\nu(\nu, T) = \frac{2h\nu^3}{c^2} \frac{1}{e^{h\nu/kT} - 1} \quad (5.33)$$

The spectral radiance has SI units of $\text{W}/\text{m}^2/\text{str}/\text{Hz}$. An image will typically display the measured flux, $S = \int \int B d\Omega$, which is the brightness integrated over the angular size of the source or pixel. The SI units for flux are $\text{W}/\text{m}^2/\text{Hz}$, but astronomers commonly use the non-SI unit of Jy instead. In the 3 mm regime it is reasonable to invoke the Rayleigh-Jeans approximation where it is assumed that that $h\nu/kT \ll 1$. Equation 5.33 then becomes

$$B_\nu(\nu, T) \approx \frac{2kT\nu^2}{c^2} \quad (5.34)$$

or

$$B_\nu(\lambda, T) \approx \frac{2kT}{\lambda^2} \quad (5.35)$$

The antenna noise power for a single polarization instrument that is observing a black body is

$$\begin{aligned} P_A &= \frac{1}{2} \times B_\nu \times A\Omega \times \Delta\nu \\ &= \frac{1}{2} \times \frac{2kT}{\lambda^2} \times \lambda^2 \times \Delta\nu \\ &= kT\Delta\nu \end{aligned} \quad (5.36)$$

where the factor of 2 comes from the fact that only one of the polarizations is measured, $A\Omega$ is the optical throughput and $\Delta\nu$ is the observation bandwidth. The antenna temperature in the Rayleigh-Jeans approximation is therefore simply the effective black body temperature of the source, which is termed the brightness temperature and is measured in units of Kelvin. In the following calculations all signals are written as brightness temperatures, but can be related to noise powers, spectral radiances or flux units through the above equations.

The expected calibration procedures that will be used with *Argus* are discussed below. Some of the calibration procedures use reference measurements that are to be differenced with an on-source observation. This difference eliminates any noise that is common between the two measurements and ideally leaves just the desired signal:

$$V_{signal} = V_{ON} - V_{OFF} \quad (5.37)$$

Procedures that difference the signal with a reference are discussed first including position switching (§5.3.3), a calibration vane (§5.3.1), and frequency switching (§5.3.4). It is also necessary to find the gain, g , of the receiver to convert units from voltage into brightness temperature:

$$T_{sys} = gV_{OFF} \quad (5.38)$$

This can be accomplished with either the *Argus* chopper vane (§5.3.1) or a flux calibration (§5.3.2). Finally, the calibration procedures that relate to the telescope optics are the pointing and focus measurements (§5.3.5) and the automatic out-of-focus (AutoOOF) holography measurements of the telescope surface (§5.3.6).

5.3.1 Chopper Vane

Argus is equipped with a calibration vane, which is used to convert measured signals into meaningful units of flux. The *Argus* chopper vane is a paddle with pyramidal polypropylene-based absorber¹² that is mechanically moved into and out of the optical path. The absorber is broadband and its performance is mostly frequency independent, which simplifies the calibration procedure. The unit conversion is made using a calibration method that compares the detected signal when the calibration vane is in place to an observation of blank sky [67]. This difference measurement is given in temperature units as

$$\Delta T_{cal} = T_{abs} - [T_{sp} + \eta_{sp} (1 - e^{-\tau A}) T_{atm}] \quad (5.39)$$

where ΔT_{cal} is the equivalent temperature of this calibration difference signal, T_{abs} is the physical temperature of the calibration vane, η_{sp} is the spillover efficiency (see §B.2), τ is the atmospheric opacity, A is the airmass and T_{atm} is the effective temperature of the atmosphere. The calibration vane is equipped with a temperature sensor so that T_{abs} is well known. The cosmic microwave background radiation was not included because it contributes equally to both measurements and cancels out when the difference is taken. There are a few of simplifying assumptions that can be

¹²Keating Tessellating TeraHertz RAM

made that uncover the utility of this calibration measurement. Firstly, the spillover temperature can be assumed to be from the atmosphere:

$$T_{sp} = (1 - \eta_{sp}) (1 - e^{-\tau}) T_{atm} \quad (5.40)$$

With this assumption Equation 5.39 becomes

$$\begin{aligned} \Delta T_{cal} &= T_{abs} - (1 - e^{-\tau}) T_{atm} \\ &= (T_{abs} - T_{atm}) + T_{atm} e^{-\tau} \end{aligned} \quad (5.41)$$

If the temperature of the calibration vane is roughly the same as the effective temperature of the atmosphere (*i.e.* $T_{abs} \approx T_{atm} = T$), then Equation 5.41 becomes

$$\Delta T_{cal} \approx T e^{-\tau} \quad (5.42)$$

which is proportional to the atmospheric attenuation.

The antenna temperature, T_A , is the equivalent temperature at the receiver input during an observation. The contribution of the antenna temperature that is from a source can be measured by doing a difference measurement between the source and a patch of blank sky, yielding ΔT_A . In this way the contribution of atmospheric emission is removed; however, the received signal is still attenuated from passing through the atmosphere. The antenna temperature of the source without atmospheric attenuation is given by $\Delta T'_A$:

$$\Delta T_A = \Delta T'_A e^{-\tau} \quad (5.43)$$

The calibrated strength of a signal in units of antenna temperature can be solved for by taking the ratio between Equations 5.42 and 5.43:

$$\Delta T'_A \approx T \frac{\Delta T_A}{\Delta T_{cal}} \quad (5.44)$$

In practice the signals from the telescope are uncalibrated voltages that relate to the equivalent temperatures through a gain factor, g , via $T_{signal} = gV_{signal}$. This implies that $\frac{\Delta T_A}{\Delta T_{cal}} = \frac{\Delta V_A}{\Delta V_{cal}}$. Therefore Equation 5.44 provides a very simple way of roughly

calibrating arbitrary voltages into proper physical units. The simplifying assumptions that were made limit the accuracy of this calibration method. There are a number of correction factors that can be applied to account for these assumptions [68]. The most significant correction is that for the temperatures not being equal. If this assumption is relaxed, then Equation 5.44 becomes

$$\Delta T'_A \approx T_C \frac{\Delta T_A}{\Delta T_{cal}} \quad (5.45)$$

where

$$T_C = T_{atm} + (T_{abs} - T_{atm}) e^\tau \quad (5.46)$$

In practice, the equivalent atmospheric temperature (T_{atm}) is determined through modeling and the atmospheric opacity (τ) can be determined through detailed weather forecasts¹³.

5.3.2 Flux Calibration

Flux calibration offers another way to determine the gain of a telescope. This method involves observing a calibration source with a well known flux. The calibration source could be either a planet or one of the ALMA Band 3 flux calibrators¹⁴, which are mostly bright quasars. The gain is determined by differencing the flux calibrator observation with a nearby off source observation:

$$g = \frac{T_{flux.cal}}{V_{flux.cal} - V_{OFF}} \quad (5.47)$$

Compared to the chopper vane method of determining telescope gain (§5.3.1) this method is more accurate but slower. It is recommended to do at least one flux density calibration per observing session.

¹³<http://www.gb.nrao.edu/~rmaddale/Weather/>

¹⁴<https://almascience.eso.org/sc/>

5.3.3 Position Switching

A position-switched observation uses a reference observation of an emission-free region of blank sky to account for the signal contribution from the system temperature. This method of subtracting the baseline emission can be utilized for both point source observations and mapping. In practice the antenna temperature is proportional to this difference signal:

$$\begin{aligned} T_A &= gV_{ON} - V_{OFF} \\ &= T_{sys} \frac{V_{ON} - V_{OFF}}{V_{OFF}} \end{aligned} \quad (5.48)$$

where Equation 5.38 gives the gain, g , for the instrument. For point sources it is typical to observe an equal amount of time in the on and off source. For mapping the reference position is measured before a scan as discussed in §5.2. Optionally the reference position can be measured again after a scan in which case each integration uses an interpolation of the two reference measurements. In both cases the IF bandwidth must be chosen so that there are a significant number of blank channels that can be used for the baseline fit.

Position switching can correct for changes in the system temperature that happen on timescales longer than the time between reference observations. The telescope slew speed is limited to $36^\circ/\text{min}$ so the dead time between a source observation and a reference observations of an off source region of blank sky can be relatively long. This means that an observation must have slow switching periods and/or significant overhead times, the latter which implies low observing efficiencies. For observations of compact sources there are two strategies that can be used to circumvent these constraints. One method is to use a “nod” observation where the source is alternately observed with two different beams of the receiver. When a beam is not on source it should be arranged so that it is observing blank sky. By leveraging multiple beams of a receiver there is minimal observing time lost to reference observations since one of the beams is usually on source; however, nodding observations still require the primary mirror to slew between positions. A speed improvement can be achieved by utilizing a “sub-beam nod” where the secondary mirror is moved to toggle between

the two positions. This procedure takes 0.5 s [36], which allows for faster switching and/or less overhead.

5.3.4 Frequency Switching

Another useful calibration procedure is frequency switching where the LO frequency is toggled between two nearby values. Taking the difference between two such signals rejects time-variable changes to the instrument passband from everything beyond the mixer (*i.e.* from the IF chain). *Argus* will typically use in-band frequency switching where the spectral line stays in the IF passband for both switching states. Since the signal is almost always being measured (except for the “blanked” time as the signal is switched), there is almost no cost in terms of lost integration time when frequency switching is implemented. Additionally, frequency switching can be done relatively quickly which means that variations on short time scales can be rejected. Typical switching frequencies are around 1 Hz for the GBT. It is recommended that at least four switching periods be implemented per integration time¹⁵. The minimum recommended switching time is 0.32 s [36].

There are a few practical considerations to keep in mind when implementing frequency switching with *Argus*. The change in LO frequency between switch states is a user settable parameter for all receivers on the GBT and is typically a few hundred MHz. *Argus* is unique in that it has a tracking YIG filter in the LO chain with a 3 dB bandpass of about 50 MHz. (See the LO chain schematic in Figure 2.9 for reference.) The effective bandpass after taking into account frequency multiplication in the LO chain is around 200 MHz. Frequency switching beyond this bandpass will block the LO signal and prevent impinging signals from being detected in one or both of the switch states. Another concern is that frequency switching can be adversely affected by frequency dependence in the LO chain. The *Argus* LO chain has a significant spectral slope and ripple. These features will be imprinted onto the frequency-switched difference signal. This could make frequency switching difficult for *Argus* measurements.

¹⁵Lower numbers of switching periods can be used in OTF mapping if the map is oversampled in the scan direction.

5.3.5 Pointing and Focus

The pointing and focus of the telescope are affected by thermal gradients and gravitational deformations and must be re-adjusted regularly. A pointing scan consists of multiple elevation and cross-elevation scans across a point source. Pointing offsets are made by finding the positions of maximum signal. Similarly a focus scan is made by moving the the telescope's subreflector along the axis perpendicular to the focal plane and adjusting this position to the location that provides maximum signal. The entire process adjusting peak/focus takes 5–10 minutes. It is recommended to check the performance at least once per hour, with more frequent checks being done during the day and early evening when thermal gradients have the largest effect [36].

5.3.6 Active Surface Corrections

The active surface of the telescope can be adjusted to correct for thermal and gravitational deformations via automatic out-of-focus (AutoOOF) holography. The AutoOOF procedure applies a low-order correction to the telescope surface that ultimately improves the beam shape and aperture efficiency. Maps are taken at three different focus settings that are well out of focus. The resulting maps are decomposed into Zernike polynomials, which give a non-degenerate solution for the surface adjustments that need to be made. The AutoOOF process takes about 25 minutes including a pointing and focus adjustment. It is recommended that the surface be re-adjusted every 2–4 hours for nighttime observations. It may be impractical to use AutoOOF observations during the day because of thermal instabilities. The point source aperture efficiency was improved by 30–50% during commissioning tests for the GBT's 4 mm receiver [69]. Similar improvements are expected with *Argus*.

5.4 LO Troubleshooting

The LO system (§2.5.3) was by far the source of the most technical issues as *Argus* was integrated at Stanford, despite the fact that a large fraction of the parts were commercially obtained. The LO problems are presented in detail in the following

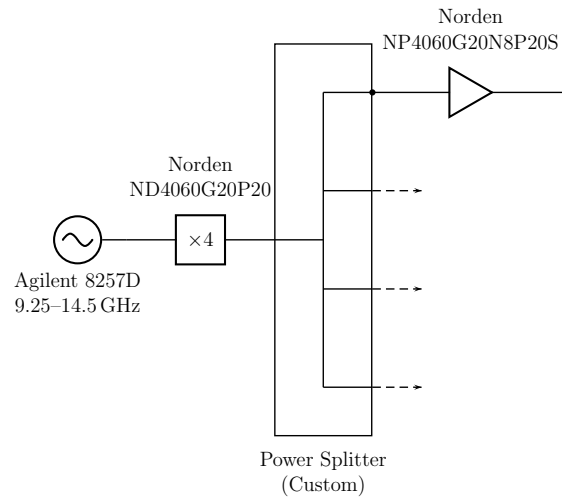


Figure 5.15: The original LO chain for *Argus*, which was used during most of the receiver integration and testing at Stanford. Spurious signals from this LO chain led to significant artifacts in the receiver performance data. The LO chain in Figure 2.9 was implemented to solve these problems.

sections. The issues include insufficient LO power pumping the mixers (§5.4.1), LO-to-RF leakage of LO harmonics (§5.4.2), and broadband noise in the LO downconverting into the IF band (§5.4.3). The initial LO chain for *Argus*, in which these problems were diagnosed, is shown in Figure 5.15. The final LO chain, in which these problems were addressed, is displayed in Figure 2.9.

5.4.1 Insufficient LO Power

Inadequate LO power levels at the receivers was an issue in both the prototyping stages and the integration of the production *Argus* receivers. The conversion loss of the mixers degrades with decreasing levels of the incident LO power and also becomes more sensitive to changes in LO power (§3.2.2). A deficit of LO power can therefore lead to two problems. Firstly, the gain of the receiver modules decreases with low LO power levels, which increases the noise contributions of all subsequent components to the system temperature as dictated by the Friis equation (Equation 2.8). Secondly, the increased sensitivity on LO power as the mixer becomes less saturated has the potential to make frequency switching the *Argus* array impractical. If the LO power

is frequency dependent, then the conversion loss of the mixer will be different in the two frequency settings, which leads to spurious spectral features in the measurement.

There were several improvements that were necessary to achieve sufficient LO power in the initial testing phases. The LO power entering the cryostat is limited by the saturation points of the commercial multiplier and power amplifiers (§2.5.3). These components were selected in part for their high saturation power relative to other components on the market. Therefore, there was little to be gained by changing any of the room temperature components in the LO chain. Instead, the improvements had to come from reducing losses inside the cryostat. The loss on the microstrip lines was higher than expected during prototyping and was reduced by systematically reducing each contribution to the noise as is discussed in detail in §4.1.3.

5.4.2 LO-to-RF Leakage

The initial noise temperature measurements of the *Argus* receivers showed noise temperatures that varied wildly across some LO frequency ranges. The noise temperature variations were highly dependent on both the LO frequency and the positioning of the hot and cold loads in the Y-factor measurements. In other words, the noise temperature results were repeatable if the loads were automatically moved with a motor but not repeatable if the loads were moved in a more imprecise manner. These variations were attributed to leakage of the second harmonic of the LO carrier (or equivalently the eighth harmonic of the synthesizer frequency) leaking into the RF feedhorn. The leakage radiates from the focal plane, upward through the window, and is finally reflected by the hot and/or cold loads into the feedhorns. The second harmonic was directly detected emanating out the window of the cryostat. Since the mixer is sub-harmonically pumped, the second harmonic of the LO frequency is in the RF passband.

It is not obvious that the second harmonic of the LO should affect the noise temperature results. The second harmonic gets downconverted into the IF at DC and should be stopped by DC block capacitors in the IF before reaching the backend instruments; any effect of the second harmonic on the measurements must therefore be

subtle. One possibility is that there were low-level “wings” that extend 0.90–2.15 GHz from the LO carrier (*e.g.* from phase noise), then this power would be downconverted into the *Argus* IF band. Unfortunately, the power level of such “wings” that would be required to cause this problem is very low and beyond the noise floor of the Stanford measurement equipment and so this hypothesis has not been verified. An unlikely alternative hypothesis is that the operating points of the MMIC components are modulated by the leakage power, causing the IF output power to change. In this scenario, one would expect the bias currents to fluctuate as a function of the coupled second harmonic power, which has not been observed. In either case, the LO-to-RF leakage appears to add power at the IF output. Since the coupling factor of the LO-to-RF leakage is highly sensitive to the absorber position, changing between hot and cold loads, which involves moving at least one of the loads, systematically changes the coupled second harmonic power and alters the measured Y-factors. Specifically, the noise powers measured with a hot and cold load presented at the RF input, P_H and P_C , are given by

$$P_H = kB(T_H + T_{Rx} + T_{LO,H}) \quad (5.49)$$

and

$$P_C = kB(T_C + T_{Rx} + T_{LO,C}) \quad (5.50)$$

where k is the Boltzmann constant, B is the bandwidth, T_{Rx} is the noise temperature of the receiver, and $T_{LO,H/C}$ is the effective temperature from the second harmonic contamination. In general, $T_{LO,H} \neq T_{LO,C}$ and either one could be larger than the other depending on the exact electromagnetic environment of the two loads. In practice this means that one would expect both positive and negative deviations in the noise temperature, which is exactly what is seen.

The most straightforward way to mitigate this problem was to block the LO-to-RF leakage path. The second harmonic of the LO carrier is generated in the both by the multiplier/power amplifier combination and at the mixer. Direct measurements of the leakage radiation¹⁶ indicated that the dominant contribution was from the mixer.

¹⁶The measurements were made using the mm-wave extenders for the network analyzer. The power was measured with an unratiod measurement on the network analyzer.

The leakage locations were measured in a similar way. The female-to-female push-on connectors¹⁷ were the dominant source of leakage, but gaps in the MMIC receiver module, the coaxial-to-microstrip transitions, and the microstrip provided subdominant contributions. Three shields were installed, which are pictured in Figure 5.16, to absorb and/or block the second harmonic LO leakage from reaching the RF feedhorns:

- A shield enclosing the multilayer IF/LO routing boards. Ideally, the aluminum shields would completely enclose the boards, forming a Faraday cage; however, in practice there are significant hole in the shield that act as ports for the IF, LO, and DC connections. The board shields are enclosed in absorber¹⁸.
- A piece of absorber¹⁹ was machined to completely enclose the area around the female-to-female push-on connectors.
- A piece of sheet metal was installed at the RF input plane of the MMIC receiver modules. The previous two shields were designed to suppress the leakage at the source. In contrast, this shield is a barrier near the destination of this unwanted signal and is a last line of defense.

The shielding successfully blocked the radiation that caused the aforementioned noise temperature measurement systematic. After shielding, the noise temperature results no longer showed the measurement-to-measurement variability nor the spectral features that were associated with this systematic; however, when measurements were taken with the shields removed, these symptoms were sometimes but not always seen. This suggests that the problem may have been an improperly seated connector. It is possible to install in the module so that there is a slight angle in the alignment of the female-to-female snap-on connector; the leakage from this connector was observed to be extremely sensitive to the angle of this connector. It's likely that improved installation techniques contributed significantly to reducing this measurement phenomenon, but the shields are nevertheless a desirable protection against this issue.

¹⁷Corning Gilbert GPPO B1B1-0001-01

¹⁸Laird GDS

¹⁹ECCOSORB MF

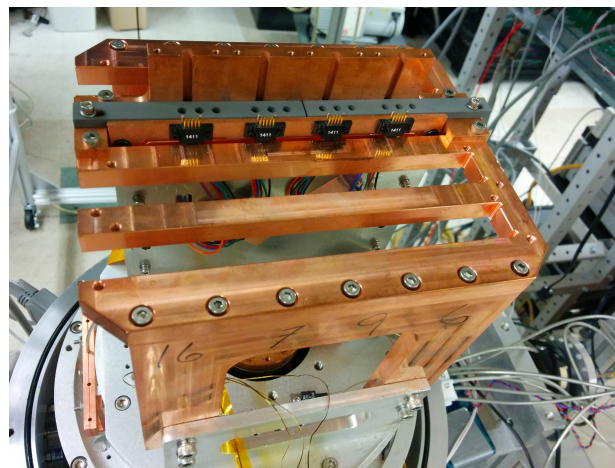
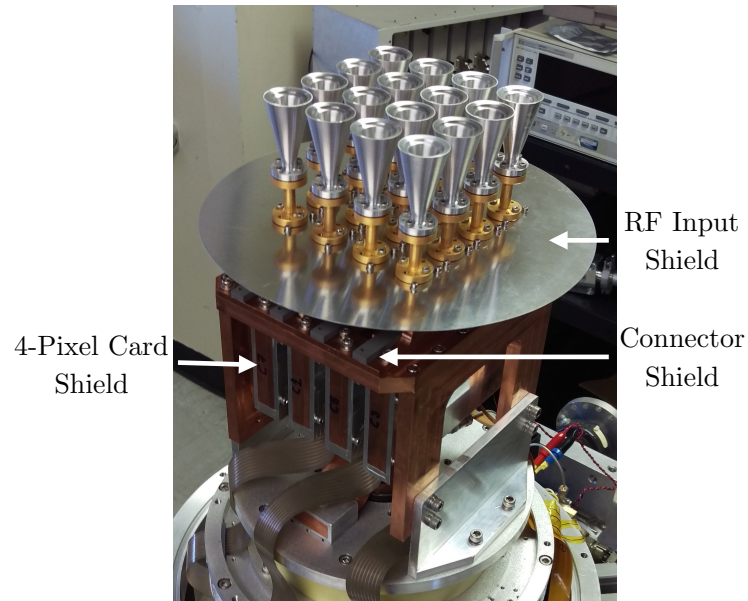


Figure 5.16: (a) A photograph of the three types of shields that were used to block LO-to-RF leakage: a metal case encloses the multilayer routing boards, a machinable piece of absorber shields the connector between the multilayer routing boards and the miniaturized receiver modules, and a metal sheet at the feedhorn antenna input plane. (b) A photograph of the connector shield before the miniaturized receiver modules were installed. Each shield is a rectangular piece of absorber with holes drilled out for the connectors to pass through.

5.4.3 Broadband LO Noise

It was found that the LO chain generated broadband noise that contaminated the IF output and increased the receiver noise temperatures tremendously before the problem was addressed. Specifically, the LO noise 0.450–1.075 GHz from the carrier was downconverted into the 0.90–2.15 GHz *Argus* IF band. It is straightforward to calculate the effects of such an LO-to-IF leakage on the measured receiver temperatures. The IF powers measured in a Y-factor measurements, P_H and P_C , are given by

$$P_{H/C} = kB G_{Rx} (T_{Rx} + T_{H/C}) + kB (G_{mix} G_{IF} T_{LO}) \quad (5.51)$$

where k is the Boltzmann constant, B is the bandwidth, T_{Rx} is the noise temperature of the receiver with a clean LO signal, T_{LO} is the effective noise temperature of the broadband LO noise, G_{Rx} is the end-to-end gain of a pixel, G_{mix} is conversion gain of the broadband LO noise into the IF band, and G_{IF} is the gain in the IF path. Rearranging Eq. 5.51 gives

$$P_{H/C} = kB G_{Rx} \left[\left(T_{Rx} + \frac{G_{mix} T_{LO}}{G_{Rx}} \right) + T_{H/C} \right] \quad (5.52)$$

which indicates that the broadband LO noise alters the effective receiver temperature as follows:

$$T'_{Rx} = T_{Rx} + \frac{G_{mix} T_{LO}}{G_{Rx}} \quad (5.53)$$

Several observations can be made from Eq. 5.53. Firstly, the excess noise contribution is additive. Therefore during Y-factor measurements, P_H and P_C receive the same (linear) offset from this effect, but P_C has a much larger fractional change. Furthermore, the additive contribution is inversely proportional to the receiver gain; frequencies with lower gain will see this effect enhanced. Many of the *Argus* pixels have reduced gain at the highest LO frequencies (roughly 113–116 GHz), which makes this problem especially troublesome since the scientifically important 12CO line is at 115.3 GHz. Finally, this noise contribution scales with both the level of LO noise, T_{LO} and its conversion efficiency, G_{mix} , into the IF.

The noise contribution from broadband LO noise has a strong frequency dependence

in the *Argus* pixels. The source of much of the frequency dependence is the standing waves on the LO path on the multilayer routing boards (Figure 4.3.2). The power of the LO carrier entering the cryostat is a relatively smooth function of frequency as it is mostly determined by the saturation power of the final stage of power amplifiers. Likewise, the LO noise sidebands presumably have only a weak frequency dependence; much of this noise is broadband noise from the various amplifier stages; however, both the LO carrier and its noise sidebands must pass through the routing inside the cryostat, which is highly frequency dependent, before it is delivered to the mixers. At frequencies where the LO carrier power delivered at the mixer is low, the receiver gain, G_{Rx} , is reduced which enhances the broadband LO noise contribution. On the other hand, at frequencies where the LO sideband noise power (T_{LO}) is high the LO noise contribution is also enhanced. There are frequencies at which *both* of these conditions are true and therefore the noise temperature undergoes a spike, which can be seen in the receiver temperature data in Figure 5.17 that was taken before this issue was addressed. The only change between this data with noise spikes and the final noise performance of the receivers that is shown in Figure 5.2 was the addition of a YIG tracking filter (shown in the schematic in Figure 2.9), that filtered out the broadband noise. In future *Argus*-like instruments, a double-balanced mixer design could also suppress this phenomenon.

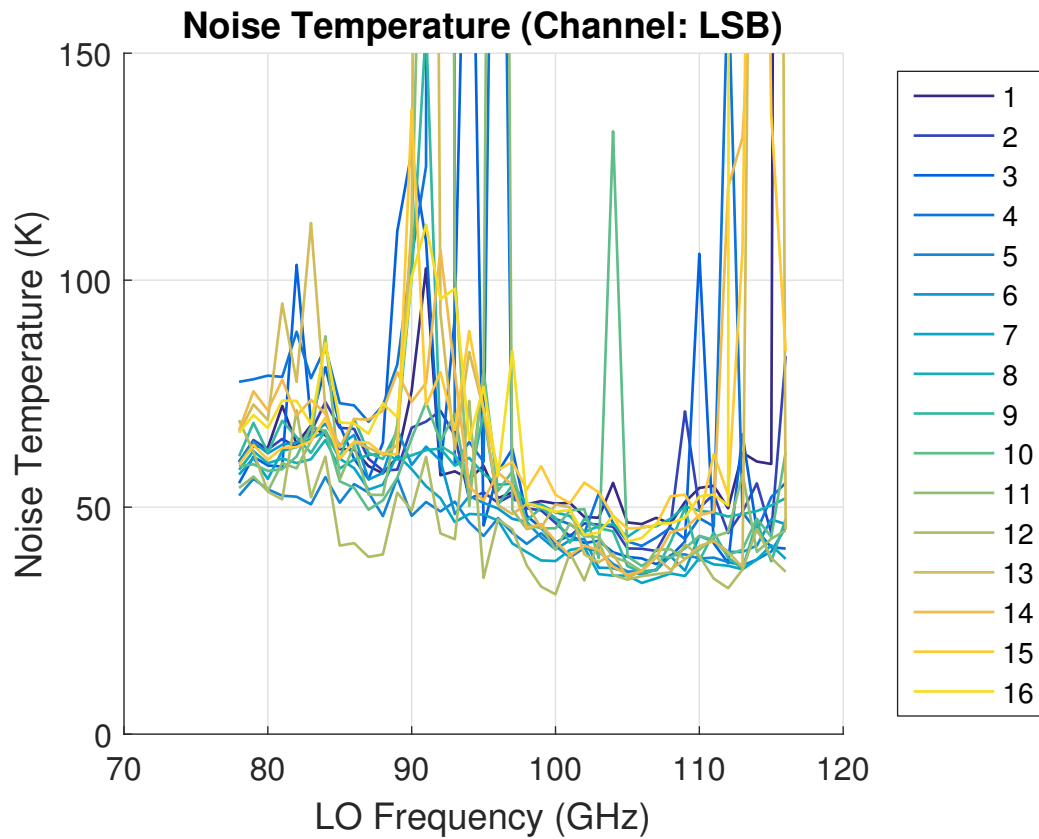


Figure 5.17: The receiver temperature for all 16 *Argus* pixels as measured in the lab with the YIG filter bypassed in the LO chain. This data is to be compared with Figure 5.2, which shows the receiver temperatures with the YIG filter in place. The spikes in the noise temperature when the filter is bypassed can be attributed to LO noise power that is downconverted into the IF path.

5.5 *Argus* Installation and First Light

Argus was installed on the GBT on March 8, 2016. The cryostat was first hoisted with a crane to the top of the GBT turret (Figure 5.18(a)). The cryostat was then dropped down one of the turret’s 24” holes (Figures 5.18(b) and 5.18(c)), while the electronics rack was attached from below in the receiver room (Figure 5.18(d)).

Argus first light was measured on March 30, 2016. Orion was chosen as a target because it is both bright and extended. The first spectrum, which is shown in Figure 5.19a, targeted the C¹⁸O and ¹³CO lines. This particular setup was one of two configurations for which *Argus* was fine-tuned. The second light spectrum measured ¹²CO at 115.271 GHz as shown in Figure 5.19b, which was the highest frequency ever observed on the GBT. Pointing and focus were not measured for the first light spectra. Instead it was simply assumed that the angular size of Orion was large enough that emission would be detected even with pointing offsets. The measurements were also uncalibrated since the *Argus* chopper vane was not yet complete when the instrument was installed. Instead the system temperature was estimated based on the expected receiver temperature and the atmospheric opacity forecasts. Finally, a raster map of Orion was taken in HCN.

The *Argus* first light measurements demonstrate that the instrument is capable of taking scientifically useful spectroscopic images. The spectral baselines in Figures 5.19a and 5.19b are qualitatively flat and stable, which is important when executing observing scans with durations of several minutes. The raster map in Figure 5.19c, which is uncalibrated, demonstrates that *Argus* is capable of making high resolution images of relatively large areas of sky in a reasonable amount of time. The next steps in the commissioning process are broadly to:

- finish implementing and testing the software interface between *Argus* and the Green Bank Telescope control software,
- to calibrate the *Argus* data,
- to verify the performance of the instrument while pointed on the sky,



(a)



(b)



(c)



(d)

Figure 5.18: Photographs from the *Argus* installation on the GBT. (a) The *Argus* cryostat being hoisted to the top level of the GBT. (b) The instrument being lowered into the receiver turret. (c) The top side of the receiver after installation. A radome protects the *Argus* window from the elements. A nozzle blows dry air across the radome to prevent condensation. (d) The bottom side of the receiver after during installation.

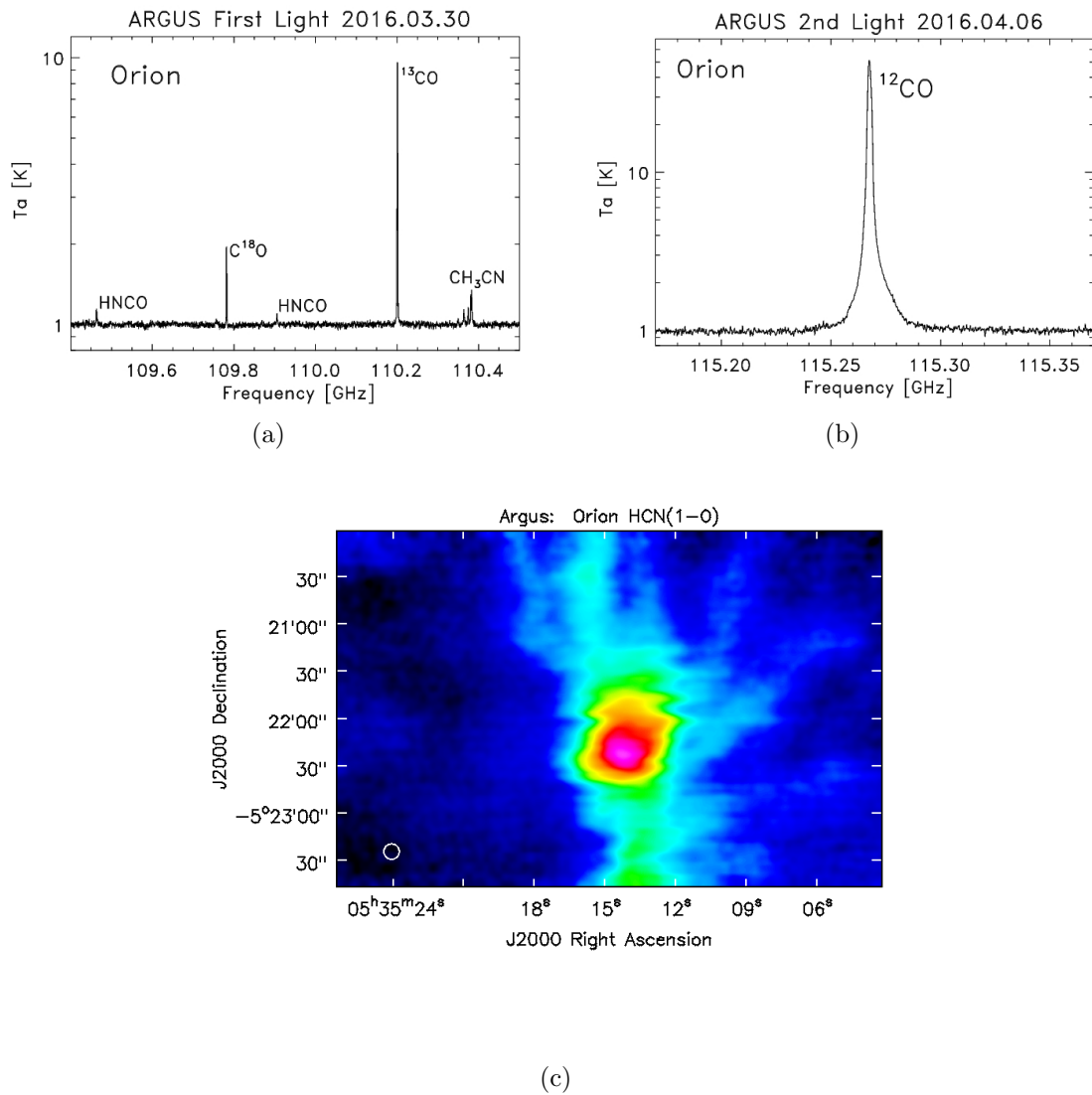


Figure 5.19: The *Argus* first and second light measurements of Orion. (a) The first light spectrum centered around 110 GHz that targeted C¹⁸O and ¹³CO. (b) The second light spectrum of ¹²CO. (c) A raster map of HCN.

- and to develop mapping schemes that efficiently map large areas of sky and are minimally affected by systematic effects.

After these commissioning tasks are complete, scientific observations will commence in the winter (16B) observing semester. These observations will be “shared-risk”, with the *Argus* instrument team helping other scientists to collect and reduce the data.

Appendix A

Y-Factor Method

In this method, the device under test (DUT) is presented with two different input noise powers and then the measured output noise powers can be used to solve for the noise temperature. The output noise power from the DUT, P_{out} , when an input noise power, P_{in} , is applied is:

$$P_{out} = G(kBT_N + P_{in}) \quad (\text{A.1})$$

where G is the gain. If the input noise power is provided by an absorber that emits approximately like a black body then we may take $P_{in} = kBT_{in}$ where T_{in} is the physical temperature of the absorber. Equation A.1 then becomes:

$$P_{out} = kBGT(T_N + T_{in}) \quad (\text{A.2})$$

The Y-factor, Y , is defined as:

$$Y = \frac{P_H}{P_C} = \frac{T_N + T_H}{T_N + T_C} \quad (\text{A.3})$$

where T_H and T_C are the physical temperatures of the hotter and colder absorbers, respectively. Finally, the noise temperature can be retrieved by solving Equation A.3:

$$T_N = \frac{T_H - YT_C}{Y - 1} \quad (\text{A.4})$$

Appendix B

Argus Optics

The *Argus* receiver is installed on the 100 m Robert C. Byrd Green Bank Telescope (GBT). The quality of the images attained with *Argus* on the GBT is largely determined by the optical design. *Argus* is designed to take high angular resolution images at fast mapping speeds so that large areas of sky can be covered. High angular resolution is achieved with the large collecting area of the GBT. The mapping speed, on the other hand, improves with the number of pixels, the receiver sensitivity, and the observing efficiency, the last of which depends on the coupling between the *Argus* receiver and the telescope. This chapter is organized as follows. A description of the GBT optics is provided in §B.1. The antenna efficiency is explored in detail in §B.2. Finally, optical simulations are presented in §B.3, which give the expected antenna efficiencies, mapping speeds, and G/T_{sys} .

B.1 The Robert C. Byrd Green Bank Telescope

The Robert C. Byrd Green Bank Telescope, or GBT, is the world's largest fully steerable radio telescope. The telescope operates over a very wide range of frequencies from 0.1–116 GHz. In the 76–116 GHz *Argus* band, observations have the potential to be significantly affected by atmospheric noise and imperfections in the telescope's surface. The atmospheric noise is combatted via a dynamic scheduling algorithm that ensures that the best atmospheric conditions are devoted to high frequency

observations [70]. In a typical year there are 2000–3000 hours that are suitable for high frequency observations. The surface of the telescope is actively controlled to correct for gravitational and thermal deformations by adjusting the position of the 2,008 mirror panels that make up the primary. Actuators are installed at the corner of each panel and are adjusted through the procedures described in §5.3.6.

The telescope utilizes an offset Gregorian design¹. There are two concave mirrors: a large primary mirror that intercepts the light and a secondary mirror that is placed beyond the focus of the primary mirror as seen in Figures B.1 and B.2. The primary mirror is a 100 m by 110 m section of a 208 m parent paraboloid and the secondary mirror is a 7.55 m by 7.95 m section of a parent ellipsoid [71]. The prime focus f/D is 0.29 and the Gregorian focus f/D is 1.9 [71]. The asymmetry of the telescope allows for the secondary mirror and the focal plane to be offset such that the primary mirror is unblocked. The unblocked primary leads to a larger effective collecting area and a cleaner beam pattern.

B.2 Antenna Efficiency

The antenna efficiency (or aperture efficiency²) of a feed and secondary mirror combination is the ratio of the effective collecting area of the system to the physical area of the secondary³. It can be decomposed into several terms:

$$\eta_{ant} = \eta_{ill}\eta_{spill}\eta_{surf} \quad (\text{B.1})$$

where η_{ill} is the illumination efficiency, η_{spill} is the spillover efficiency, and η_{surf} is the surface efficiency. The remainder of this section defines these various sub-efficiencies.

The illumination efficiency, η_{ill} , accounts for the non-uniformity of the beam pattern

¹A Gregorian design was chosen so that the telescope could optionally be used in prime focus mode where the receiver is placed at the focal point in front of the secondary mirror. The prime focus receivers operate at <2 GHz.

²The term “aperture efficiency” is used widely in the literature, however “antenna efficiency” is the IEEE standardized term [72].

³A good review of feed horn figures of merit including a section on antenna efficiency is provided in [73].



Figure B.1: A photograph of the Robert C. Byrd Green Bank Telescope. Credit: NRAO.

that illuminates the secondary. If parts of the telescope are under-illuminated then the effective area of the telescope is decreased. The illumination efficiency is relevant for point source detection where large overlap is desired between the Airy pattern and a single feedhorn. It is defined as the ratio of on-axis far field power to the total power in the aperture plane:

$$\eta_{ill} = \frac{1}{A} \frac{\left| \vec{E}(\phi = 0) \right|^2}{\int_A \left| \vec{E}_a(x, y) \right|^2 dA} \quad (\text{B.2})$$

where $\vec{E}(\phi)$ is the electric field in the far field and $\vec{E}_a(x, y)$ is the electric field in the aperture plane. It is convenient for computations of the illumination efficiency to express Equation B.2 in terms of just the electric field at the aperture field. This can be done by using the fact that the far field electric field is the Fourier transform of the electric field in the aperture field:

$$\vec{E}(\phi) = \int_A \vec{E}_a(x, y) e^{2\pi(r/\lambda) \sin \phi} dA \quad (\text{B.3})$$

Substituting Equation B.3 into Equation B.2 with $\phi = 0$ for the on-axis field yields:

$$\eta_{ill} = \frac{1}{A} \frac{\left| \int_A \vec{E}_a(x, y) dA \right|^2}{\int_A \left| \vec{E}_a(x, y) \right|^2 dA} \quad (\text{B.4})$$

The illumination efficiency can be decomposed into two components: the **taper efficiency**, η_t , which is the amplitude component, and the **phase error**, η_{ph} , which is the phase component.

$$\eta_{ill} = \eta_t \eta_{ph} \quad (\text{B.5})$$

These two components are defined in Equations (B.6) and (B.7), respectively.

$$\eta_t = \frac{1}{A} \frac{\left[\int_A \left| \vec{E}_a(x, y) \right| dA \right]^2}{\int_A \left| \vec{E}_a(x, y) \right|^2 dA} \quad (\text{B.6})$$

$$\eta_{ph} = \frac{\left| \int_A \vec{E}_a(x, y) dA \right|^2}{\left[\int_A \left| \vec{E}_a(x, y) \right| dA \right]^2} \quad (\text{B.7})$$

The degree of illumination is commonly expressed in terms of “edge taper”, which is the ratio of the power at the center of the aperture plane to that at the edge of the dish. If it is assumed that all beams are Gaussian, then the edge taper is an unambiguous way to specify the illumination.

The spillover efficiency, η_{spill} , is simply the fraction of incident power from the feed horn that is intercepted by the reflector:

$$\eta_{spill} = \frac{\int_0^{2\pi} \int_0^{\theta_0} |E(\theta, \phi)|^2 \sin(\theta) d\theta d\phi}{\int_0^{2\pi} \int_0^{\pi} |E(\theta, \phi)|^2 \sin(\theta) d\theta d\phi} \quad (\text{B.8})$$

where $E(\theta, \phi)$ is the far-field electric field and θ_0 is the angle that defines the edge of the reflector. The spillover efficiency is anti-correlated with the illumination efficiency. For example, at high edge tapers, there is very little radiation that spills over beyond the edge of the telescope mirrors, which yields high spillover efficiency, but the edges of the dishes are poorly illuminated, which gives poor illumination efficiency.

The surface efficiency, η_{surf} , quantifies the degradation in observing efficiency from scattering from imperfections on the surface of the telescope. To find the surface efficiency, one first needs the RMS of the surface errors, ϵ_{surf} which is elevation dependent [74]:

$$\epsilon_{surf} = (415.36 - 7.11El + 0.0656El^2) \mu\text{m} \quad (\text{B.9})$$

where El is the elevation in degrees. The RMS surface error of the GBT is 220 μm when the telescope is at an elevation of 45°. Ruze’s equation then gives the surface efficiency as:

$$\eta_{surf} = e^{-\left(\frac{4\pi\epsilon_{surf}f}{c}\right)^2} \quad (\text{B.10})$$

where f is the frequency being observed and c is the speed of light. The surface efficiency degrades rapidly with frequency, which is particularly significant for *Argus* since it operates at the highest frequencies possible at the GBT (76–116 GHz).

B.3 Simulated *Argus* Performance

The antenna efficiencies were simulated for for the *Argus* feedhorn antennas on the GBT using an optical design program⁴. A model of the GBT was created using the dimensions provided in [71], which is shown in Figure B.2. A realistic radiation pattern for the feedhorn antennas was input into the model by decomposing the simulated aperture fields into either Hermite-Gaussian or Laguerre-Gaussian modes as is discussed in §B.3.1. The simulated efficiencies were then computed as the frequency and the beamwidth of the feedhorn antennas were tuned, which is presented in §B.3.2. Finally, two figures of merit, the mapping speed and G/T_{sys} , were considered as a function of the feedhorn beam size and the frequency as discussed in §B.3.3. Ultimately this analysis contributed to the selection of the beam size for the production *Argus* feedhorns.

B.3.1 Mode Decomposition

Simulated *Argus* feedhorn beam patterns were imported into the optical model in order to study the expected instrument performance. The simulated beam patterns from [6] were decomposed into both Hermite-Gaussian and Laguerre-Gaussian modes as shown in Figure B.3. This decomposition was then used as input into the model. The beams are mostly Gaussian; the total power in the Gaussian mode was 93%. Corrugated feedhorns, by comparison, achieve 98% for a corrugated feed horn under balanced hybrid conditions [75].

B.3.2 Simulated Efficiencies

The efficiencies were calculated from the model using the definitions in §B.2. The results are plotted as a function of both edge taper and frequency. The antenna efficiency, which is the observing efficiency of a point source, is optimized at an edge taper of ~ 11 dB. The *Argus* edge taper, which is frequency dependent, is about 15 dB at 100 GHz. This edge taper was chosen to optimize mapping speeds, which is discussed in

⁴Zemax

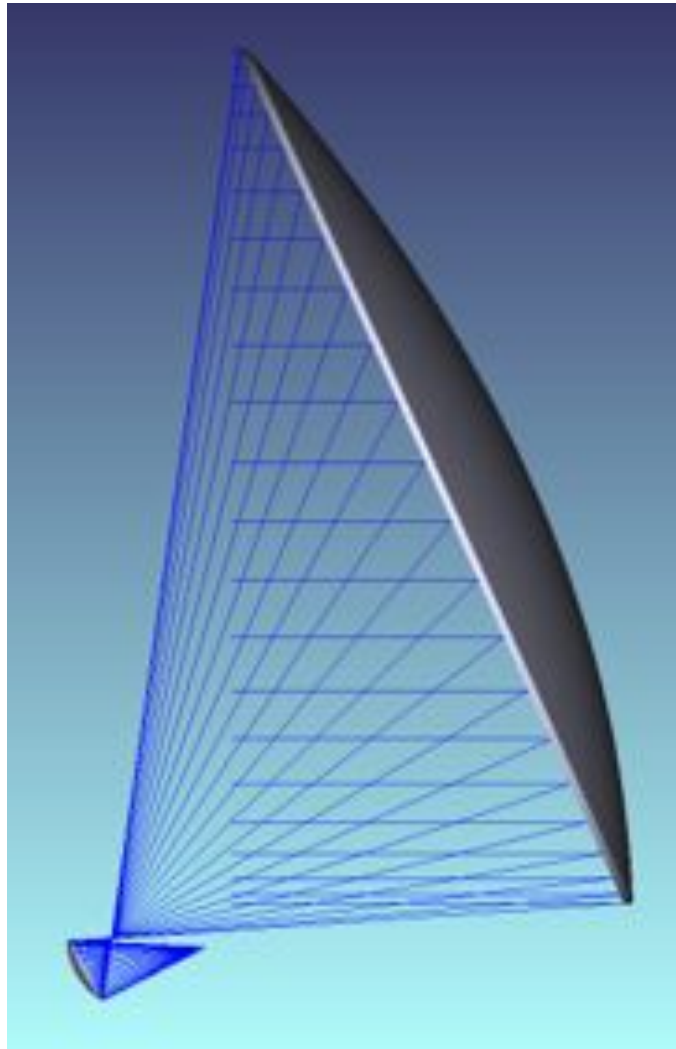


Figure B.2: A CAD model of the GBT that was used to study the observing efficiency and mapping speed of *Argus* as a function of the feedhorn beam size.

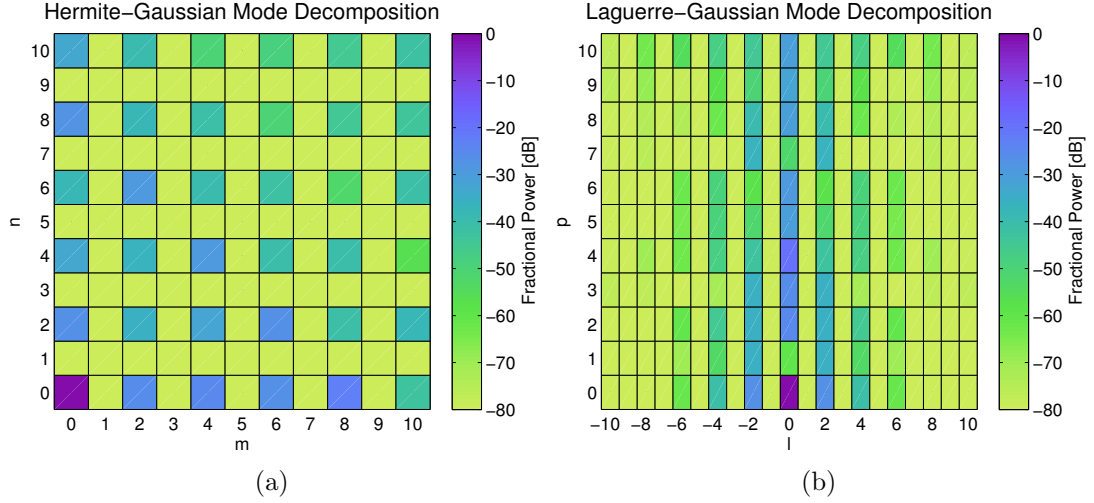


Figure B.3: The higher-order modes of the *Argus* horns that were simulated in [6]. The simulated beam patterns were imported into an optical design program to study the optical interface between *Argus* and the GBT. About 93% of the power is in the fundamental Gaussian mode.

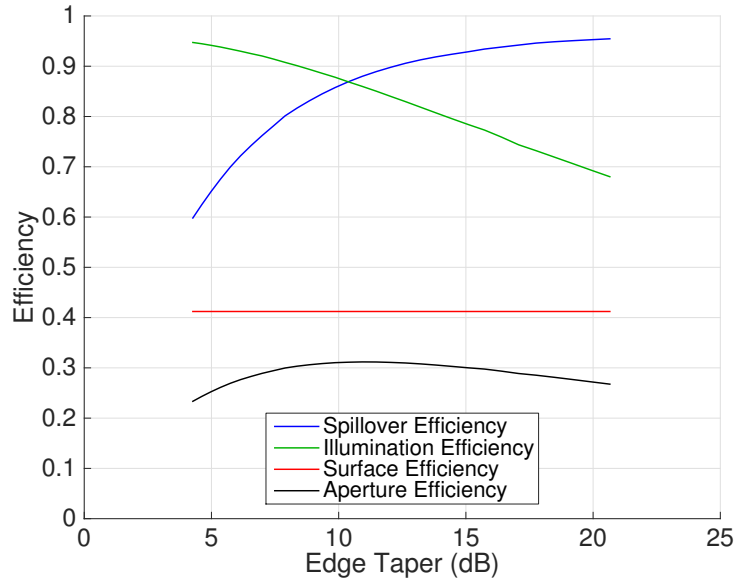
further detail in §B.3.3. The antenna efficiency degrades with frequency because of the surface efficiency and the illumination efficiency. The surface efficiency decreases with frequency as governed by Equation B.10, while the illumination efficiency decreases because of the smaller feedhorn beamwidths at higher frequencies.

B.3.3 Figures of Merit

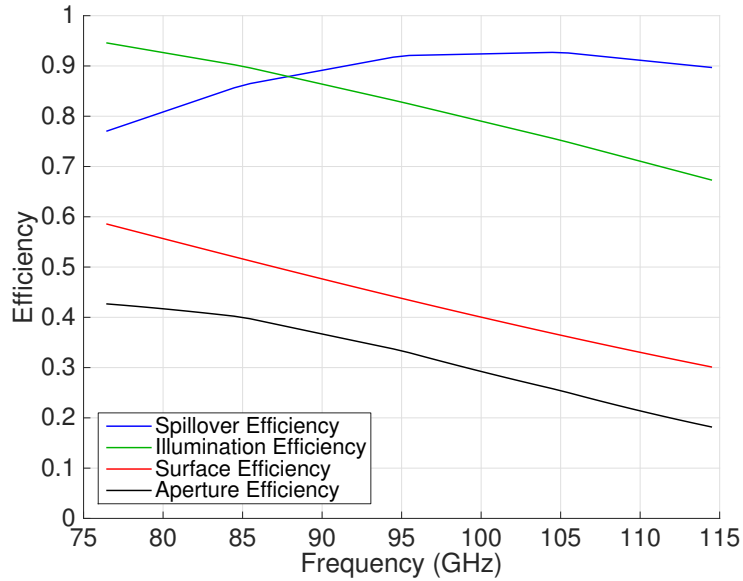
The choice of edge taper (and feedhorn beamwidth) for *Argus* was determined in part by considering a couple of figures of merit: the mapping speed and G/T_{sys} . The time required to complete a map, t_{map} , is dependent on the coupling between the receiver and telescope. Specifically,

$$t_{map} \propto \frac{T_{sys}^2}{\eta_{spill}} \quad (\text{B.11})$$

where T_{sys} is the system temperature, which has a contribution from spillover pickup (§5.1.2). The efficiencies were calculated from the model using the definitions in §B.2. The resulting mapping times are plotted as a function of both frequency and edge



(a)



(b)

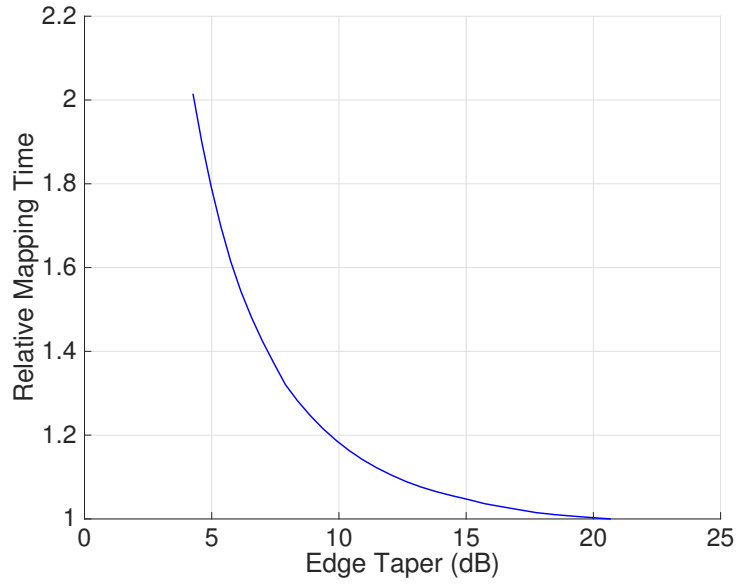
Figure B.4: (a) The coupling efficiencies to the telescope versus edge taper at a frequency of 100 GHz. The optimal antenna efficiency, which is the relevant efficiency for point source detection, is at ~ 11 dB. The *Argus* edge taper at 100 GHz is ~ 15 dB. (b) The coupling efficiencies to the telescope versus frequency. The illumination efficiency and surface efficiency degrade with increasing frequency.

taper in Figure B.5. A second commonly used figure of merit is G/T_{sys} , where G is the telescope gain which is:

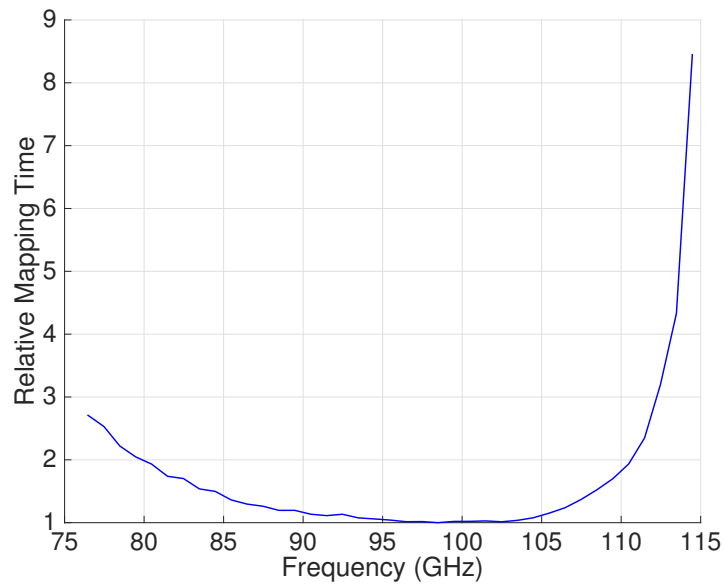
$$G = \frac{4\pi A_{eff}}{\lambda^2} \quad (\text{B.12})$$

where $A_{eff} = A\eta_{ill}$ is the effective collecting area of the dish. The calculated G/T_{sys} values are plotted as a function of edge taper and frequency in Figures B.6a and B.6b, respectively. The G/T_{sys} is best at an edge taper of ~ 18 dB.

An edge taper of ~ 15 dB at 100 GHz was chosen for *Argus*. The point source sensitivity is greatest at ~ 11 dB edge taper. On the other, the mapping time and G/T_{sys} are better at ~ 18 dB edge taper or above. The *Argus* edge taper is a compromise between these two metrics.

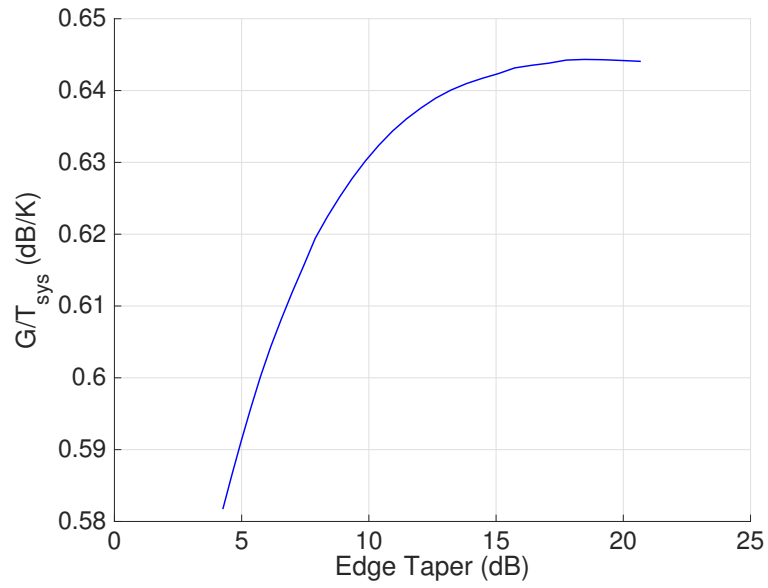


(a)

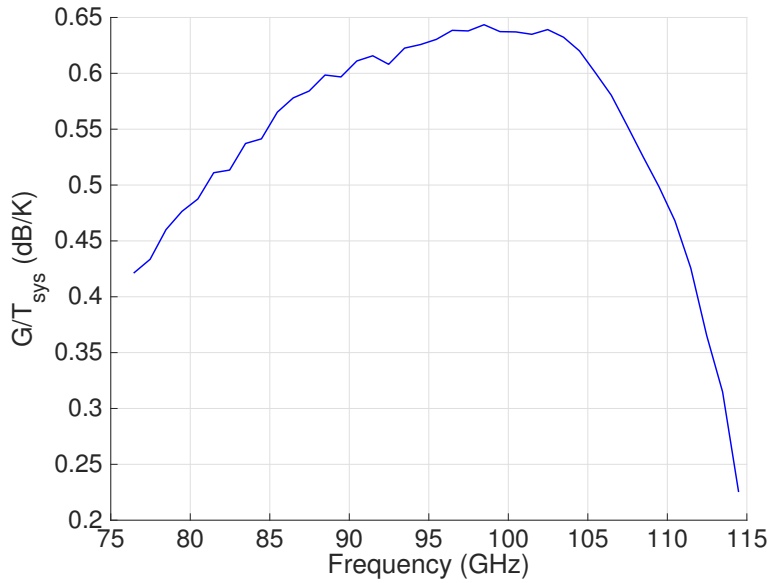


(b)

Figure B.5: (a) The relative mapping times versus edge taper at 100 GHz. The mapping times improve with increasing edge taper. (b) The relative mapping times versus frequency. The mapping time increases at the upper frequencies in the *Argus* band due to higher system temperatures.



(a)



(b)

Figure B.6: (a) G/T_{sys} versus edge taper at 100 GHz. The optimal value is at ~ 18 dB. (b) G/T_{sys} versus frequency. The performance degrades at the band edges.

Appendix C

Measurement Setups

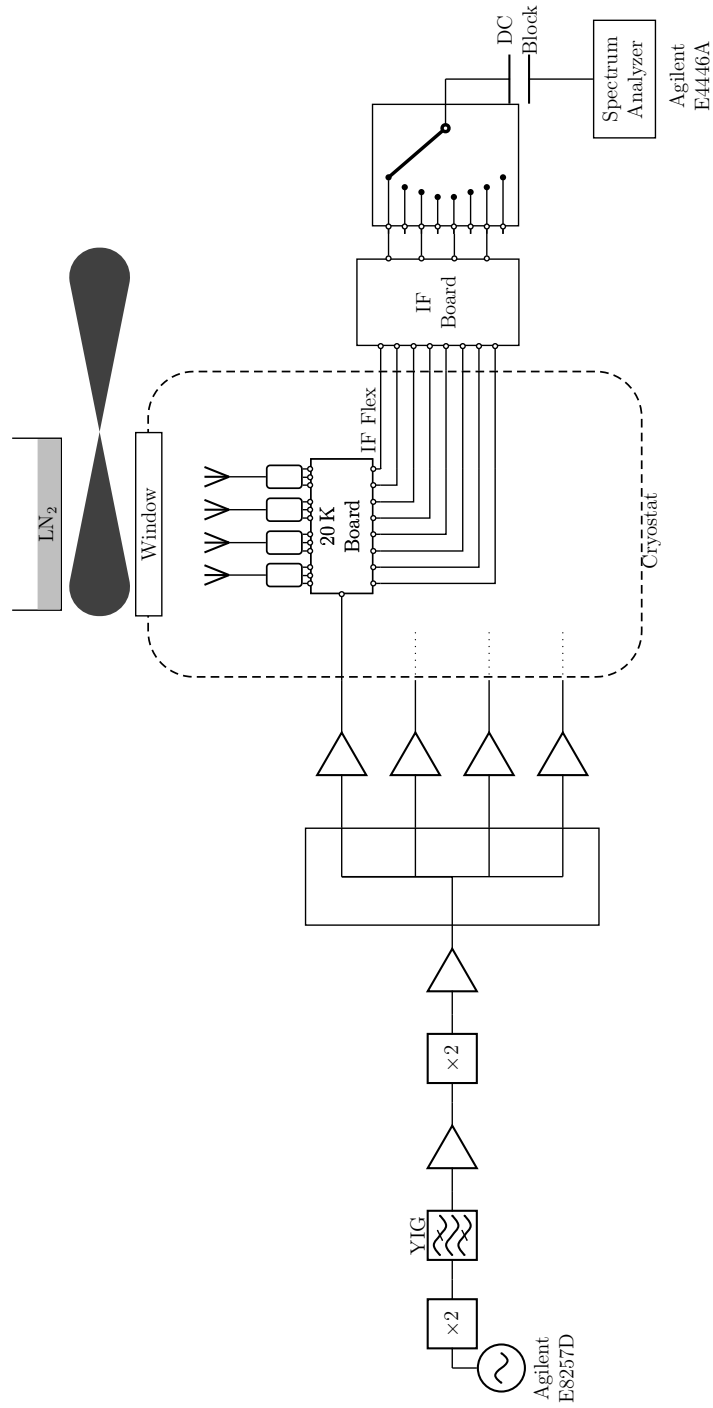


Figure C.1: A schematic of the test setup used to characterize the receiver noise temperature.

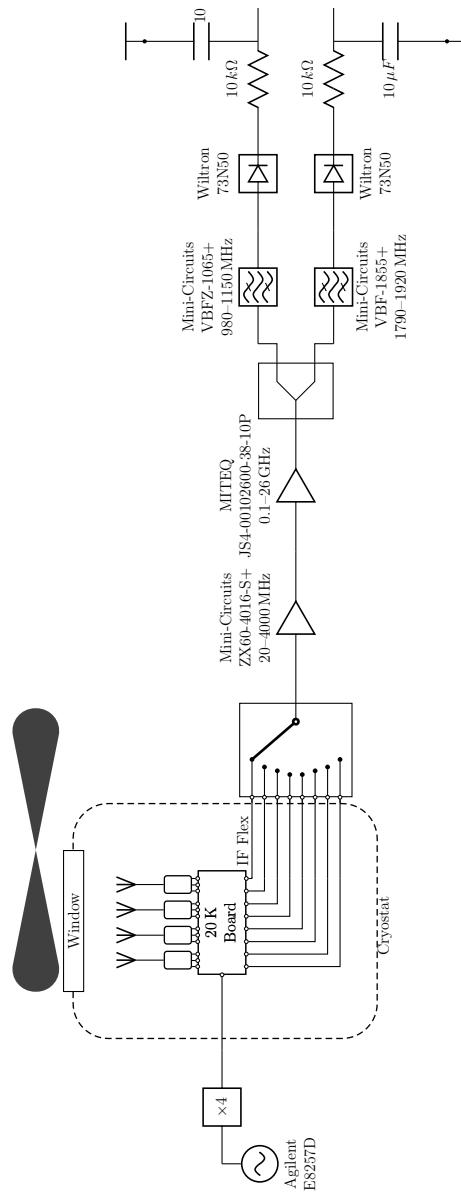


Figure C.2: A schematic of the spectroscopic Allan variance test setup.

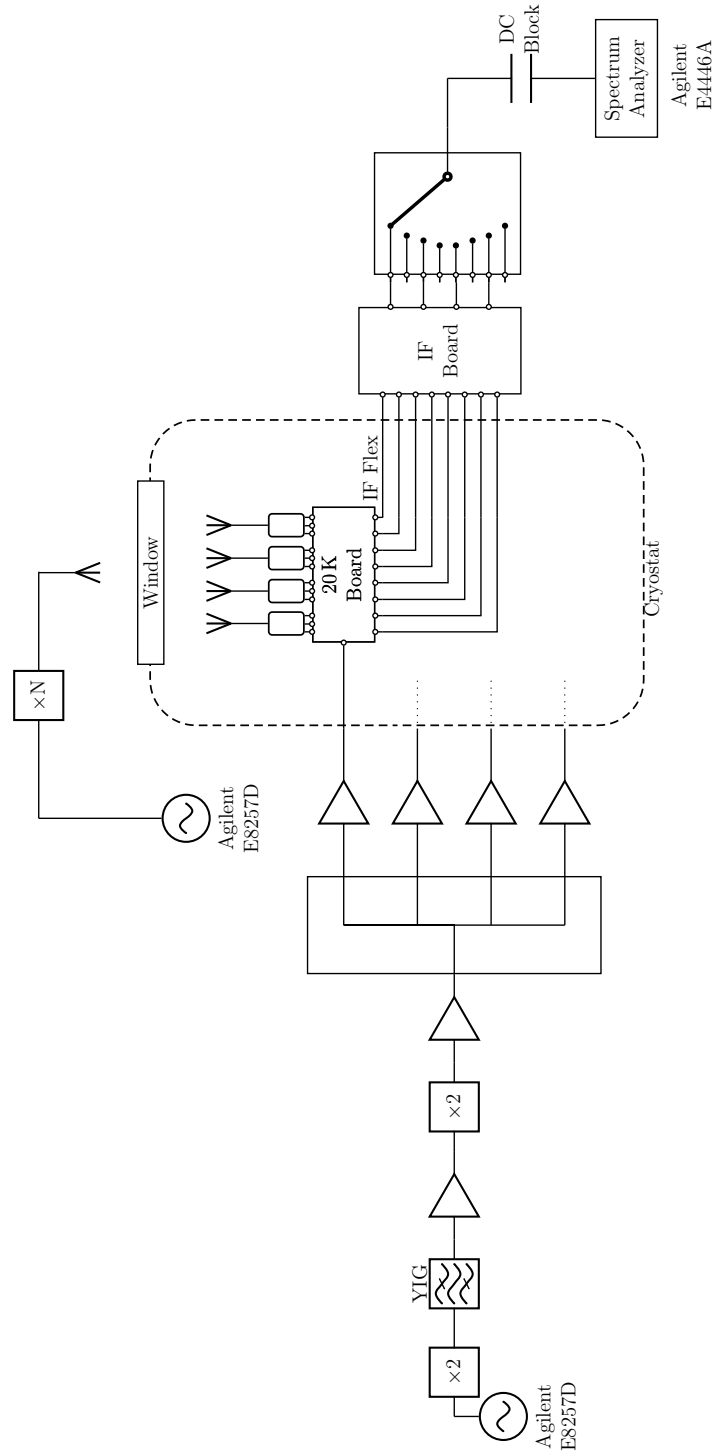


Figure C.3: A schematic of the image rejection ratio test setup.

Appendix D

Frequency Tripler

An on-board frequency tripler was prototyped but ultimately not implemented in either the final production or prototype multilayer routing boards. Performing the frequency multiplication inside the cryostat is desirable because the signal is subject to much lower loss before multiplication. It is difficult to both generate a 39–59 GHz signal with high power to pump into the cryostat and to minimize the ohmic losses inside the cryostat. Doing the frequency multiplication cryogenically in principle can solve both of these problems. There exist some active commercial frequency multipliers¹, however they dissipate a large amount of power that would degrade the cryogenic performance.

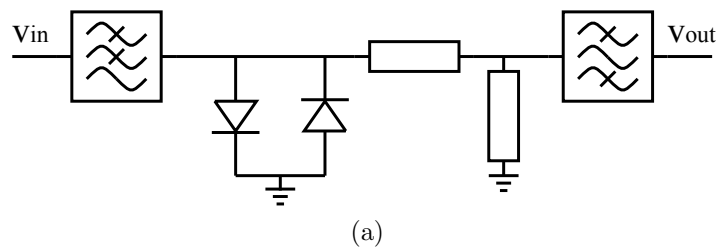
A prototype tripler is shown in Fig. D.1, which is designed around an antiparallel diode pair that functions as a sine-wave to square-wave converter. An inexpensive GaAs flip-chip dual diode² with a 3 THz cutoff frequency was used, which lends to the mass-producibility of the design. A 4-pole stepped-impedance low-pass filter was implemented on the input side, with a 3 dB frequency of 23.6 GHz. The output filter is a 4-pole coupled line design with a measured 3 dB bandpass of 38.5–48.3 GHz.

The output power of the tripler as a function of frequency and input power was measured and is shown in Figure D.2. The tripler measurements were frequency selective as opposed to a simple total power measurement. A signal generator³ provided

¹*e.g.* the MACOM XX1000-QT

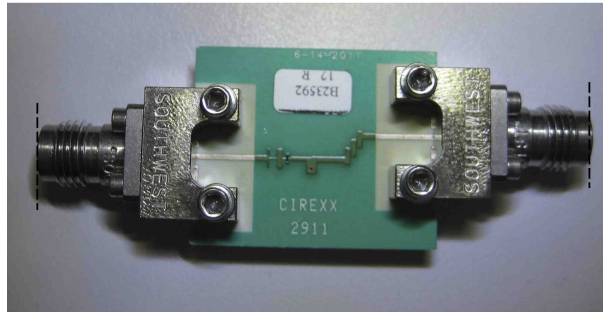
²United Monolithic Semiconductors DBES105a

³Agilent E8257D PSG Analog Signal Generator



(a)

----- Measurement Reference Plane

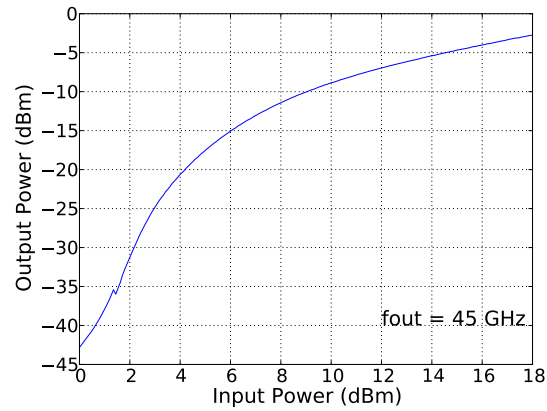


(b)

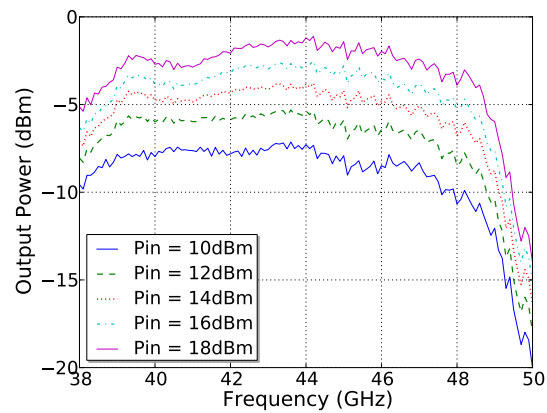
Figure D.1: (a) A schematic of the prototype frequency tripler, which utilizes a flip-chip dual diode. The input filter is a stepped-impedance design. A coupled-line filter is included as a part of the output match. (b) A photograph of a prototype test board for the diode tripler.

the input signal and the output was measured using an unratiod receiver measurement with a network analyzer ⁴. A 2.4 mm coaxial cable was connected between the signal generator and the frequency tripler, while the output was connected directly to the 2.4 mm port of the network analyzer. A source power calibration was applied at the DUT side of the 2.4 mm cable, which was chosen as the input reference plane for these measurements. The output reference plane is at the output 2.4 mm connector. A 2-port SOLT calibration was performed on the network analyzer ports as a source/receiver calibration. The output power at 45 GHz is about 0.5 mW for a 63 mW input, which is the anticipated operating condition for implementation into a focal plane array. Higher output powers could be achieved by combining additional diodes in series with the existing diodes.

⁴Agilent E8364B PNA Series Network Analyzer



(a)



(b)

Figure D.2: (a) Output power versus input power with the output frequency at 45 GHz. (b) Output power versus output frequency where the input power is varied between 10–18 dBm in increments of 2 dBm.

Bibliography

- [1] F. L. Schöier, F. F. S. van der Tak, E. F. van Dishoeck, and J. H. Black. An atomic and molecular database for analysis of submillimetre line observations. *Astronomy & Astrophysics*, 432(1):369–379, March 2005.
- [2] M. W. Pospieszalski. Modeling of noise parameters of MESFETs and MODFETs and their frequency and temperature dependence. *IEEE Transactions on Microwave Theory and Techniques*, 37(9):1340–1350, September 1989.
- [3] R. Gawande, R. Reeves, L. Samoska, K. Cleary, A. C. Readhead, T. Gaier, P. Kangaslahti, M. Varonen, S. Church, K. Devaraj, M. Sieth, and M. Morgan. W-band IQ sub-harmonic mixers with low LO power for cryogenic operation in large arrays. In *European Microwave Integrated Circuit Conference (EuMIC), 2014 9th*, pages 301–304, October 2014.
- [4] R. Gawande, R. Reeves, K. Cleary, A. C. Readhead, T. Gaier, P. Kangaslahti, L. Samoska, S. Church, M. Sieth, P. Voll, A. Harris, R. Lai, and S. Sarkozy. W-band heterodyne receiver module with 27 K noise temperature. In *Microwave Symposium Digest (MTT), 2012 IEEE MTT-S International*, pages 1–3, June 2012.
- [5] A. I. Harris, M. Sieth, J. M. Lau, S. E. Church, L. A. Samoska, and K. Cleary. Note: Cryogenic microstripline-on-kapton microwave interconnects. *Review of Scientific Instruments*, 83(8), 2012.

- [6] Patricia Voll, Sami Tantawi, and Mohammed El-Beltagy. A Smooth-Walled Feed-horn Antenna Design for Astrophysical Instrumentation in Space. In *Proceedings of the 62nd International Astronautical Congress*, pages 1–7, 2011.
- [7] Gopal Narayanan, Mark H. Heyer, Christopher Brunt, Paul F. Goldsmith, Ronald Snell, and Di Li. The Five College Radio Astronomy Observatory CO Mapping Survey of the Taurus Molecular Cloud. *The Astrophysical Journal Supplement Series*, 177(1):341, 2008.
- [8] Thomas Wilson, Kristen Rohlfs, and Susanne Huettemeister. *Tools of Radio Astronomy*. Astronomy and Astrophysics Library. Springer Berlin Heidelberg, Berlin, Heidelberg, 2009.
- [9] Lyman Spitzer. *Physical Processes in the Interstellar Medium*. Wiley-VCH Verlag GmbH, Weinheim, Germany, May 1998.
- [10] Yancy L. Shirley. The Critical Density and the Effective Excitation Density of Commonly Observed Molecular Dense Gas Tracers. *Publications of the Astronomical Society of the Pacific*, 127(949):299, 2015.
- [11] Yu Gao and Philip M. Solomon. The Star Formation Rate and Dense Molecular Gas in Galaxies. *The Astrophysical Journal*, 606(1):271, 2004.
- [12] M. Schmidt. The Rate of Star Formation. *Astrophysical Journal*, 129:243, March 1959.
- [13] Jr. Robert C. Kennicutt. The Global Schmidt Law in Star-forming Galaxies. *The Astrophysical Journal*, 498(2):541, 1998.
- [14] Amanda Heiderman, Neal J. Evans II, Lori E. Allen, Tracy Huard, and Mark Heyer. The Star Formation Rate and Gas Surface Density Relation in the Milky Way: Implications for Extragalactic Studies. *The Astrophysical Journal*, 723(2):1019, 2010.
- [15] Sachiko Onodera, Nario Kuno, Tomoka Tosaki, Kotaro Kohno, Kouichiro Nakanishi, Tsuyoshi Sawada, Kazuyuki Muraoka, Shinya Komugi, Rie Miura, Hiroyuki

- Kaneko, Akihiko Hirota, and Ryohei Kawabe. Breakdown of Kennicutt-Schmidt Law at Giant Molecular Cloud Scales in M33. *The Astrophysical Journal Letters*, 722(2):L127, 2010.
- [16] D. B. Sanders, B. T. Soifer, J. H. Elias, B. F. Madore, K. Matthews, G. Neugebauer, and N. Z. Scoville. Ultraluminous infrared galaxies and the origin of quasars. *Astrophysical Journal*, 325:74–91, February 1988.
- [17] Jingwen Wu, Neal J. Evans II, Yancy L. Shirley, and Claudia Knez. The Properties of Massive, Dense Clumps: Mapping Surveys of HCN and CS. *The Astrophysical Journal Supplement Series*, 188(2):313, 2010.
- [18] J. Wu, N. J. Evans, II, Y. Gao, P. M. Solomon, Y. L. Shirley, and P. A. Vanden Bout. Connecting Dense Gas Tracers of Star Formation in our Galaxy to High-z Star Formation. *Astrophysical Journal*, 635:L173–L176, December 2005.
- [19] Amanda A. Kepley, Adam K. Leroy, David Frayer, Antonio Usero, Josh Marvil, and Fabian Walter. The Green Bank Telescope Maps the Dense, Star-forming Gas in the Nearby Starburst Galaxy M82. *The Astrophysical Journal Letters*, 780(1):L13, 2014.
- [20] Frank Bigiel, Adam K. Leroy, Maria J. Jiménez-Donaire, Jérôme Pety, Antonio Usero, Diane Cormier, Alberto Bolatto, Santiago Garcia-Burillo, Dario Colombo, Manuel González-García, Annie Hughes, Amanda A. Kepley, Carsten Kramer, Karin Sandstrom, Eva Schinnerer, Andreas Schruba, Karl Schuster, Neven Tomić, and Laura Zschaechner. The EMPIRE Survey: Systematic Variations in the Dense Gas Fraction and Star Formation Efficiency from Full-disk Mapping of M51. *The Astrophysical Journal Letters*, 822(2):L26, 2016.
- [21] André, Ph., Men’shchikov, A., Bontemps, S., Könyves, V., Motte, F., Schneider, N., Didelon, P., Minier, V., Saraceno, P., Ward-Thompson, D., Di Francesco, J., White, G., Molinari, S., Testi, L., Abergel, A., Griffin, M., Henning, Th., Royer, P., Merín, B., Vavrek, R., Attard, M., Arzoumanian, D., Wilson, C. D., Ade, P., Aussel, H., Baluteau, J.-P., Benedettini, M., Bernard, J.-Ph., Blommaert, J.

- A. D. L., Cambr esy, L., Cox, P., Di Giorgio, A., Hargrave, P., Hennemann, M., Huang, M., Kirk, J., Krause, O., Launhardt, R., Leeks, S., Le Penneec, J., Li, J. Z., Martin, P. G., Maury, A., Olofsson, G., Omont, A., Peretto, N., Pezzuto, S., Prusti, T., Roussel, H., Russeil, D., Sauvage, M., Sibthorpe, B., Sicilia-Aguilar, A., Spinoglio, L., Waelkens, C., Woodcraft, A., and Zavagno, A. From filamentary clouds to prestellar cores to the stellar IMF: Initial highlights from the Herschel Gould Belt Survey. *Astronomy & Astrophysics*, 518:L102, July 2010.
- [22] Molinari, S., Swinyard, B., Bally, J., Barlow, M., Bernard, J.-P., Martin, P., Moore, T., Noriega-Crespo, A., Plume, R., Testi, L., Zavagno, A., Abergel, A., Ali, B., Anderson, L., Andr e, P., Baluteau, J.-P., Battersby, C., Beltr an, M. T., Benedettini, M., Billot, N., Blommaert, J., Bontemps, S., Boulanger, F., Brand, J., Brunt, C., Burton, M., Calzoletti, L., Carey, S., Caselli, P., Cesaroni, R., Cernicharo, J., Chakrabarti, S., Chrysostomou, A., Cohen, M., Compi egne, M., de Bernardis, P., de Gasperis, G., di Giorgio, A. M., Elia, D., Faustini, F., Flagey, N., Fukui, Y., Fuller, G. A., Ganga, K., Garcia-Lario, P., Glenn, J., Goldsmith, P. F., Griffin, M., Hoare, M., Huang, M., Ikhenaode, D., Joblin, C., Joncas, G., Juvela, M., Kirk, J. M., Lagache, G., Li, J. Z., Lim, T. L., Lord, S. D., Marengo, M., Marshall, D. J., Masi, S., Massi, F., Matsuura, M., Minier, V., Miville-Desch enes, M.-A., Montier, L. A., Morgan, L., Motte, F., Mottram, J. C., M uller, T. G., Natoli, P., Neves, J., Olmi, L., Paladini, R., Paradis, D., Parsons, H., Peretto, N., Pestalozzi, M., Pezzuto, S., Piacentini, F., Piazzo, L., Polychroni, D., Pomar es, M., Popescu, C. C., Reach, W. T., Ristorcelli, I., Robitaille, J.-F., Robitaille, T., Rod on, J. A., Roy, A., Royer, P., Russeil, D., Saraceno, P., Sauvage, M., Schilke, P., Schisano, E., Schneider, N., Schuller, F., Schulz, B., Sibthorpe, B., Smith, H. A., Smith, M. D., Spinoglio, L., Stamatellos, D., Strafella, F., Stringfellow, G. S., Sturm, E., Taylor, R., Thompson, M. A., Traficante, A., Tuffs, R. J., Umana, G., Valenziano, L., Vavrek, R., Veneziani, M., Viti, S., Waelkens, C., Ward-Thompson, D., White, G., Wilcock, L. A., Wyrowski, F., Yorke, H. W., and Zhang, Q. Clouds, filaments, and protostars: The Herschel Hi-GAL Milky Way. *Astronomy & Astrophysics*, 518:L100, July 2010.

- [23] Arzoumanian, D., André, Ph., Didelon, P., Könyves, V., Schneider, N., Menskchikov, A., Sousbie, T., Zavagno, A., Bontemps, S., Di Francesco, J., Griffin, M., Hennemann, M., Hill, T., Kirk, J., Martin, P., Minier, V., Molinari, S., Motte, F., Peretto, N., Pezzuto, S., Spinoglio, L., Ward-Thompson, D., White, G., and Wilson, C. D. Characterizing interstellar filaments with Herschel in IC 5146. *Astronomy & Astrophysics*, 529:L6, May 2011.
- [24] Paul F. Goldsmith, Mark Heyer, Gopal Narayanan, Ronald Snell, Di Li, and Chris Brunt. Large-Scale Structure of the Molecular Gas in Taurus Revealed by High Linear Dynamic Range Spectral Line Mapping. *The Astrophysical Journal*, 680(1):428, 2008.
- [25] Nathan J. Goldbaum, Mark R. Krumholz, Christopher D. Matzner, and Christopher F. McKee. The Global Evolution of Giant Molecular Clouds. II. The Role of Accretion. *The Astrophysical Journal*, 738(1):101, 2011.
- [26] D. Balsara, D. Ward-Thompson, and R.M. Crutcher. A turbulent MHD model for molecular clouds and a new method of accretion on to star-forming cores. *Monthly Notices of the Royal Astronomical Society*, 327(3):715–720, 2001.
- [27] Andy Pon, Jesús A. Toalá, Doug Johnstone, Enrique Vázquez-Semadeni, Fabian Heitsch, and Gilberto C. Gómez. Aspect Ratio Dependence of the Free-fall Time for Non-spherical Symmetries. *The Astrophysical Journal*, 756(2):145, 2012.
- [28] W. M. Irvine, F. P. Schloerb, J. Crovisier, B. Fegley, Jr., and M. J. Mumma. Comets: a Link Between Interstellar and Nebular Chemistry. *Protostars and Planets IV*, page 1159, May 2000.
- [29] J. M. Hollis, P. R. Jewell, F. J. Lovas, A. Remijan, and H. Møllendal. Green Bank Telescope Detection of New Interstellar Aldehydes: Propenal and Propanal. *Astrophysical Journal*, 610:L21–L24, July 2004.
- [30] J. M. Hollis, P. R. Jewell, F. J. Lovas, and A. Remijan. Green Bank Telescope Observations of Interstellar Glycolaldehyde: Low-Temperature Sugar. *The Astrophysical Journal Letters*, 613(1):L45, 2004.

- [31] J. M. Hollis, Anthony J. Remijan, P. R. Jewell, and F. J. Lovas. Cyclopropenone (c-H₂C₃O): A New Interstellar Ring Molecule. *The Astrophysical Journal*, 642(2):933, 2006.
- [32] J. M. Hollis, F. J. Lovas, Anthony J. Remijan, P. R. Jewell, V. V. Ilyushin, and I. Kleiner. Detection of Acetamide (CH₃CONH₂): The Largest Interstellar Molecule with a Peptide Bond. *The Astrophysical Journal Letters*, 643(1):L25, 2006.
- [33] Matthew W Powner, Béatrice Gerland, and John D Sutherland. Synthesis of activated pyrimidine ribonucleotides in prebiotically plausible conditions. *Nature*, 459(7244):239–242, May 2009.
- [34] A. Wootten. Deuterated molecules in interstellar clouds. In *Astrochemistry*, volume 120 of *IAU Symposium*, pages 311–318, 1987.
- [35] D Anish Roshi, Marty Bloss, Patrick Brandt, Srikanth Bussa, Hong Chen, Paul Demorest, Gregory Desvignes, Terry Filiba, Richard J Fisher, John Ford, David Frayer, Robert Garwood, S. Gowda, Glenn Jones, Billy Mallard, Joseph Masters, R. McCullough, Guifre Molera, K. O’Neil, Jason Ray, Simon Scott, Amy Shelton, Andrew Siemion, Mark Wagner, G. Watts, Dan Werthimer, and Mark Whitehead. Advanced multi-beam spectrometer for the Green Bank Telescope. In *2011 XXXth URSI General Assembly and Scientific Symposium*, pages 1–4. IEEE, August 2011.
- [36] Dana Balsler, Jim Braatz, David Frayer, Frank Ghigo, Amanda Kepley, Adam Kobelski, Karen O’Neil, Glen Langston, Ron Maddalena, Brian Mason, Toney Minter, Dan Perera, Richard Prestage, and Scott Ransom. *Observing With The Green Bank Telescope*, January 2015.
- [37] N Erickson and G Narayanan. MMIC Receiver Systems Developed at the University of Massachusetts, Amherst. In *MMIC Array Receivers and Spectrographs Workshop*, Pasadena, CA, 2008.

- [38] N. R. Erickson, P. F. Goldsmith, G. Novak, R. M. Grosslein, P. J. Viscuso, R. B. Erickson, and C. R. Predmore. A 15 element focal plane array for 100 GHz. *IEEE Transactions on Microwave Theory Techniques*, 40:1–11, January 1992.
- [39] M. Camiade, C. Dourlens, V. Serru, P. Savary, and J. C. Blanc. Highly integrated and compact W-band front-end for radiometry application. In *Gallium Arsenide Integrated Circuit (GaAs IC) Symposium, 1995. Technical Digest 1995., 17th Annual IEEE*, pages 230–237, October 1995.
- [40] W. H. Haydl. Resonance phenomena and power loss in conductor-backed coplanar structures. *IEEE Microwave and Guided Wave Letters*, 10(12):514–516, December 2000.
- [41] A. Tessmann, M. Kuri, M. Riessle, H. Massler, M. Zink, W. Reinert, W. Bronner, and A. Leuther. A Compact W-Band Dual-Channel Receiver Module. In *2006 IEEE MTT-S International Microwave Symposium Digest*, pages 85–88, June 2006.
- [42] J. Schellenberg, R. Chedester, and J. McCoy. Multi-Channel Receiver for an E-band FMCW Imaging Radar. In *2007 IEEE/MTT-S International Microwave Symposium*, pages 1359–1362, June 2007.
- [43] Matthew Sieth, Judy M. Lau, Patricia Voll, Sarah Church, Pekka Kangaslahti, Lorene Samoska, Mary Soria, Todd Gaier, Dan Van Winkle, Jeffrey Neilson, Sami Tantawi, Kieran Cleary, and Anthony C. S. Readhead. Development of MMIC receivers for cosmic microwave background interferometry. In *Proc. SPIE*, volume 7741, pages 77412I–77412I–12, 2010.
- [44] Pekka P. Kangaslahti, Todd C. Gaier, Joelle T. Cooperrider, Lorene A. Samoska, Mary M. Soria, Ian J. O’Dwyer, Sander Weinreb, Brian Custodero, Heather Owen, Keith Grainge, Judy M. Lau, Sarah E. Church, Richard Lai, and Xiaobing Mei. Compact, Miniature MMIC Receiver Modules for an MMIC Array Spectrograph. *NASA Tech Briefs*, pages 14–15, December 2009.

- [45] Matthew Sieth, Sarah Church, Judy M. Lau, Patricia Voll, Todd Gaier, Pekka Kangaslahti, Lorene Samoska, Mary Soria, Kieran Cleary, Rohit Gawande, Anthony C.S. Readhead, Rodrigo Reeves, Andrew Harris, Jeffrey Neilson, Sami Tantawi, and Dan Van Winkle. Technology developments for a large-format heterodyne MMIC array at W-band. *International Journal of Microwave and Wireless Technologies*, 4(3):299–307, April 2012.
- [46] R. Gawande, R. Reeves, K. Cleary, J. Kooi, A. C. Readhead, T. Gaier, P. Kangaslahti, L. Samoska, M. Varonen, S. Church, K. Devaraj, M. Sieth, P. Voll, A. Harris, R. Lai, and S. Sarkozy. A W-band heterodyne receiver module prototype for focal plane arrays. In *2014 IEEE MTT-S International Microwave Symposium (IMS2014)*, pages 1–4, June 2014.
- [47] Juan Luis Cano de Diego. *Cryogenic Technology in the Microwave Engineering: Application to MIC and MMIC Very Low Noise Amplifier Design*. PhD thesis, University of Cantabria, June 2010.
- [48] E. W. Bryerton, Xiaobing Mei, Y. M. Kim, W. Deal, W. Yoshida, M. Lange, J. Uyeda, M. Morgan, and R. Lai. A W-band low-noise amplifier with 22K noise temperature. In *Microwave Symposium Digest, 2009. MTT '09. IEEE MTT-S International*, pages 681–684, June 2009.
- [49] L. A. Samoska. An Overview of Solid-State Integrated Circuit Amplifiers in the Submillimeter-Wave and THz Regime. *IEEE Transactions on Terahertz Science and Technology*, 1(1):9–24, September 2011.
- [50] Lorene A. Samoska, Sarah Church, Kieran Cleary, Andy Fung, Todd C. Gaier, Pekka Kangaslahti, Richard Lai, Judy M. Lau, Gerry Mei, Rodrigo Reeves, Matthew M. Sieth, and Patricia Voll. Cryogenic MMIC Low Noise Amplifiers for W-Band and Beyond. In *International Symposium on Space Terahertz Technology*, Tucson, AZ, 2011.
- [51] L. Samoska, M. Varonen, R. Reeves, K. Cleary, R. Gawande, P. Kangaslahti, T. Gaier, R. Lai, and S. Sarkozy. W-Band cryogenic InP MMIC LNAs with noise

- below 30K. In *2012 IEEE/MTT-S International Microwave Symposium Digest*, pages 1–3. IEEE, June 2012.
- [52] M. Varonen, R. Reeves, P. Kangaslahti, L. Samoska, A. Akgiray, K. Cleary, R. Gawande, A. Fung, T. Gaier, S. Weinreb, A. C. S. Readhead, C. Lawrence, S. Sarkozy, and R. Lai. A 75–116-GHz LNA with 23-K noise temperature at 108 GHz. In *Microwave Symposium Digest (IMS), 2013 IEEE MTT-S International*, pages 1–3, June 2013.
- [53] M. W. Pospieszalski. Extremely low-noise amplification with cryogenic FETs and HFETs: 1970-2004. *IEEE Microwave Magazine*, 6(3):62–75, September 2005.
- [54] Richard Lai. Two Approaches to Improvement of InGaAs / InAlAs / InP HEMTs. *NASA Tech Brief from JPL New Technology Report NPO-20341*, 25(2):1–3, 2000.
- [55] Yoke-Choy Leong and S. Weinreb. Full band waveguide-to-microstrip probe transitions. In *Microwave Symposium Digest, 1999 IEEE MTT-S International*, volume 4, pages 1435–1438, June 1999.
- [56] S. Weinreb, R. Lai, N. Erickson, T. Gaier, and J. Wielgus. W-band InP wideband MMIC LNA with 30 K noise temperature. In *Microwave Symposium Digest, 1999 IEEE MTT-S International*, volume 1, pages 101–104, June 1999.
- [57] Damon Russell, Kieran Cleary, and Rodrigo Reeves. Cryogenic probe station for on-wafer characterization of electrical devices. *Review of Scientific Instruments*, 83(4), 2012.
- [58] E. R. Pillai. Coax via-A technique to reduce crosstalk and enhance impedance match at vias in high-frequency multilayer packages verified by FDTD and MoM modeling. *IEEE Transactions on Microwave Theory and Techniques*, 45(10):1981–1985, October 1997.
- [59] V. Ossenkopf. The stability of spectroscopic instruments: a unified Allan variance computation scheme. *Astronomy & Astrophysics*, 479(3):915–926, March 2008.

- [60] R. Schieder, G. Rau, and B. Vowinkel. Characterization and Measurement of System Stability. In *Proc. SPIE*, volume 0598, pages 189–192, 1986.
- [61] Jacob Willem Kooi. *Advanced Receivers for Submillimeter and Far Infrared Astronomy*. PhD thesis, University of Groningen, 2008.
- [62] D. W. Allan. Statistics of atomic frequency standards. *Proceedings of the IEEE*, 54(2):221–230, February 1966.
- [63] Mangum, J. G., on, D. T. Emer, and en, E. W. Grei. The On The Fly imaging technique. *Astronomy & Astrophysics*, 474(2):679–687, 2007.
- [64] Schieder, R. and Kramer, C. Optimization of heterodyne observations using Allan variance measurements. *Astronomy & Astrophysics*, 373(2):746–756, July 2001.
- [65] Attila Kovács. Scanning strategies for imaging arrays. In *Proc. SPIE*, volume 7020, pages 702007–702007–14, 2008.
- [66] T. Minter. *The proposer’s guide for the Green Bank Telescope*, 2008.
- [67] A. A. Penzias and C. A. Burrus. Millimeter-Wavelength Radio-Astronomy Techniques. *Annual Review of Astronomy and Astrophysics*, 11(1):51–72, 1973.
- [68] B. L. Ulich and R. W. Haas. Absolute calibration of millimeter-wavelength spectral lines. *Astrophysical Journals*, 30:247–258, March 1976.
- [69] D. T. Frayer, Ronald J. Maddalena, M. Meijer, L. Hough, S. White, R. Norrod, G. Watts, M. Stennes, R. Simon, D. Woody, S. Srikanth, M. Pospieszalski, E. Bryerton, M. Whitehead, P. Ford, M. Mello, and M. Bloss. The GBT 67-93.6 GHz Spectral Line Survey of Orion-KL. *The Astronomical Journal*, 149(5):162, 2015.
- [70] M. T. McCarty, D. S. Balse, J. Braatz, M. H. Clark, J. Condon, R. E. Creager, R. J. Maddalena, P. Marganian, K. O’Neil, E. Sessoms, and A. L. Shelton. The GBT Dynamic Scheduling System. In *Astronomical Data Analysis Software and Systems XXI*, volume 461 of *Astronomical Society of the Pacific Conference Series*, page 193, September 2012.

- [71] R Norrod and S Srikanth. A summary of the GBT optics design. *NRAO GBT Memo Series*, 155, March 1996.
- [72] IEEE Standard Definitions of Terms for Antennas. *IEEE Std 145-1993*, pages 1–32, July 1993.
- [73] A.D. Olver and Institution of Electrical Engineers. *Microwave Horns and Feeds*. Electromagnetics and Radar Series. IEE, 1994.
- [74] Dan Perera. *The GBT Sensitivity Calculator User's Guide*, 2013.
- [75] R. J. Wylde. Millimetre-wave Gaussian beam-mode optics and corrugated feed horns. *Microwaves, Optics and Antennas, IEE Proceedings H*, 131(4):258–262, August 1984.